INSPYRE
Investigations Supporting MOX Fuel Licensing in ESNII Prototype Reactors

EERA JPNM
JOINT PROGRAMME ON NUCLEAR MATERIALS

D6.4 – Synthesis of the inert gas behaviour models developed in INSPYRE

D. Pizzocri, T. Barani, L. Cognini, L. Luzzi, A. Magni (POLIMI),
A. Schubert, P. Van Uffelen, T. Wiss (JRC)

Version 1 – 30/08/2020

The INSPYRE project has received funding from the EURATOM research and training programme 2014-2018 under Grant Agreement No 754329.

Document type	Deliverable
Document number	D6.4 version 1
Document title	Synthesis of the inert gas behaviour models developed in INSPYRE
Authors	D. Pizzocri, T. Barani, L. Cognini, L. Luzzi, A. Magni (POLIMI), A. Schubert, P. Van Uffelen, T. Wiss (JRC)
Release date	30/08/2020
Contributing partners	POLIMI, JRC-Karlsruhe
Dissemination level	Public

Version	Short description	Main author	WP leader	Coordinator
1	First release	D. Pizzocri (POLIMI) 27/08/2020	A. Del Nevo (ENEA) 27/08/2020	M. Bertolus (CEA) 30/08/2020

SUMMARY

The goal of this deliverable is to present a synthesis of the model developments achieved during the INSPYRE Project with respect to the description of inert gas (i.e., helium and fission gases) behaviour in MOX fuel. The models presented are designed for use in fuel performance codes and are particularly suited for the simulation of fuel experiencing fast reactor conditions (higher temperatures and burn-up compared to light water reactor conditions). They allow for fast and robust numerical solution. The principles of the models presented herein are described in Deliverable D6.1, whereas the details about the inclusion in fuel performance codes will the subject of D7.2.

Despite their targeted application, all the developed models are physics-based, allowing for the use of lower-length scale information either by introducing/disregarding specific mechanisms or by defining specific model parameters. The characteristic length scale at which inert gas behaviour is described by the models herein presented is the scale of the fuel grain. This is in line with the approach followed in state-of-the-art models used in fuel performance codes.

The conclusion of this deliverable includes a possible roadmap for future developments to be targeted in INSPYRE and after the end of the project.

CONTENT

GLOSSARY

CRAM	Chebychev Rational Approximation Method
FR	Fast Reactor
G	Galerkin projection
Gen-IV	Generation IV
HBS	High Burn-up Structure
HM	Heavy Metal
INSPYRE	Investigations Supporting MOX Fuel Licensing for ESNII Prototype Reactors
JPNM	Joint Programme on Nuclear Materials
KEMS	Knudsen-cell Effusion Mass Spectrometry
KJMA	Kolmogorov-Johnson-Mehl-Avrami
LBE-FR	Lead-Bismuth Eutectic – Fast Reactor
LELI	SERPENT numerical option
LFR	Lead-cooled Fast Reactor
MOX	Mixed Oxide Fuel
NR	Non-restructured
ODE	Ordinary Differential Equation
POD	Proper Orthogonal Decomposition
PDE	Partial Differential Equation
ROM	Reduced Order Model
SFR	Sodium-cooled Fast Reactor
V&V	Verification and Validation
WP	Work Package

1 INTRODUCTION

The current description of inert gas behaviour in fuel performance codes presents significant limitations when it comes to mixed oxide (MOX) fuels in fast reactor (FR) conditions [1–4]. These limitations are due to three main reasons:

- A limited amount of experimental data concerning inert gas behaviour is available.
- Expected high values of release suggested that detailed description of inert gas behaviour was not required.
- Several inter-related phenomena connected to inert gas behaviour (e.g., pore migration towards the centre of the pellet, formation of columnar grains, redistribution of uranium and plutonium [5–7]) are currently decoupled from gas behaviour in fuel performance codes (if treated at all).

As identified in the objectives of INSPYRE and discussed in the previous deliverable D6.1 [8], the proper modelling of inert gas behaviour in fast reactor (FR) MOX is fundamental in fuel performance codes. In fact, even from a purely engineering point of view, there are indications that expected fission gas release are well below 100% in several designs of Gen-IV FRs (e.g., MYRRHA, ALFRED) [9–12]. Moreover, the relative scarcity of experimental data/information calls for the development of physics-based models instead of correlation-based models. These models can be informed from lower-length scale knowledge (either simulations or experiments) whereas the development of correlations relies on (expensive) integral irradiation experiments. Lastly, physics-based models allow for effective multi-scale bridging, gaining better understanding about the detailed mechanisms involved and transferring knowledge acquired from separate-effect experiments and lower-length scale calculations to the engineering-scale of fuel performance codes (as demonstrated for UO_2 in LWRs, e.g., [13,14]). This implies a more efficient and effective use of coordinated research efforts, potentially speeding up the development and licensing of FR MOX.

The present deliverable is a synthesis of publications prepared in the INSPYRE Project, for which explicit reference is provided in each section. Four specific aspects are addressed: (1) intra-granular helium behaviour and helium production, (2) diffusion of inert gas in columnar grains, (3) grain-boundary venting tailored to high temperature conditions, and (4) a model describing the formation of HBS and its characteristic depletion of intra-granular gas.

The principles of the models presented herein are described in Deliverable D6.1, whereas the details about the inclusion in fuel performance codes will the subject of D7.2. All the described models are implemented in SCIANTIX [15], a mesoscale code treating inert gas behaviour and designed to be included directly in fuel performance codes

The conclusion of this deliverable includes a possible roadmap for future developments to be targeted within and after the framework of INSPYRE.

HELIUM BEHAVIOUR

Helium behaviour is potentially critical in MOX fuels irradiated in fast reactor conditions because of the higher production of actinides presenting α-decays compared to light water reactors (LWRs) fuels. This section covers the details concerning a physics-based model describing intra-granular helium behaviour (Section 2.1) and details of a depletion model tracking the concentration of actinides (Section 2.2).

1.1 Intra-granular helium behaviour

We present in this section the mechanistic model developed to describe intra-granular helium behaviour in oxide fuel. The proposed model is suitable for application in fuel performance codes, and is hence implemented in the fission gas behaviour module SCIANTIX [15] and compared with the current model adopted in the TRANSURANUS performance code [16–18].

The content of this section is published in *L. Cognini, A. Cechet, T. Barani, D. Pizzocri, P. Van Uffelen, L. Luzzi, "Towards a meso-scale mechanistic description of intra-granular helium behaviour in oxide fuel for application in fuel performance codes", Nuclear Engineering and Technology, 2020* [19].

1.1.1 Model description

The proposed model aims at a physics-based description of the helium release and retention mechanisms by extending state-of-the-art models developed for the description of intra-granular fission gas behaviour (such as [14,20,21]) by including the treatment of helium solubility. Although it is not usually considered for xenon and krypton (as discussed and ruled out, e.g., by Lösönen [22]), solubility of fission gases was included in rate theory models by Veshchunov [23] due to its potential contribute at high temperatures. In this work, we propose a description of helium solubility in oxide fuel in line with [22,23]. It was shown that helium solubility in oxide nuclear fuel is linearly proportional to the infusion pressure at a fixed temperature [24] and hence that the system He-UO_2 obeys Henry's law:

$$C_S = k_H p \tag{1}$$

Where, k_H (at m^{-3} MPa^{-1}) is Henry's constant for the He-UO_2 system, C_S (at m^{-3}) is the solubility achieved at a pressure p (MPa).

The inclusion in the model of the mobility of intra-granular helium bubbles was proposed by Talip *et al.* [25], based on the observation of helium release rates from doped fuel samples. This model extension follows the generalization of Speight's rate theory model [20] proposed by Van Uffelen *et al.* [26]. In this work, however, we do not include this bubble-diffusivity term since the only bubble diffusion coefficient available is that derived in [25] by fitting the experimental results of helium release rate during annealing of doped fuel samples. This dataset is herein selected as validation base for the proposed model and therefore we apply parameters derived independently in the frame of INSPYRE [8].

Summarizing, the proposed model includes single-atom diffusion (in an equivalent sphere [27]), trapping of single atoms at intra-granular bubbles and irradiation induced re-solution of gas atoms from intra-granular bubbles, helium solubility, and helium production rate as follows:

$$\frac{\partial c}{\partial t} = S + D\frac{1}{r^2}\frac{\partial}{\partial r}r^2\frac{\partial}{\partial r^2}c - \beta\left(c - C_{S,\mathrm{ig}}\right) + \alpha m$$
$$\frac{\partial m}{\partial t} = \beta\left(c - C_{S,\mathrm{ig}}\right) - \alpha m \qquad (2)$$

in which r (m) is the radial coordinate along the fuel grain (assumed as spherical) and t (s) is time, c and m (at m^{-3}) are the concentration of helium single-atoms and helium in intra-granular bubbles, respectively, S (at m^{-3} s^{-1}) is the helium production rate (this term includes ternary fissions, (n,α)-reactions on oxygen, and α-decays.), β (s^{-1}) is the trapping rate and α (s^{-1}) is the irradiation-induced re-solution rate, D (m^2 s^{-1}) is the single-atom diffusion coefficient, and $C_{S,\mathrm{ig}}$ (at m^{-3}) is the intra-granular helium solubility. Using Eq. 1, these solubilities are related to the helium pressure in those bubbles, i.e.

$$C_{S,\mathrm{ig}} = k_H p_{\mathrm{ig}} \qquad (3)$$

The boundary conditions assumed for the single-atom diffusion problem are

$$c(r = a, t) = C_{S,\mathrm{gb}} = k_H p_{\mathrm{gb}}$$
$$\frac{\partial}{\partial r}c(r = 0, t) = 0 \qquad (4)$$

Where, a (m) is the radius of the spherical fuel grain and $C_{S,\mathrm{gb}}$ (at m^{-3}) is the inter-granular helium solubility.

Besides the definition of each model parameter appearing in Eq. 2, which is detailed in the following, it is worth noting that the introduction of the solubility calls for the necessity of evaluating the helium pressure within intra- (p_{ig}) and inter-granular bubbles (p_{gb}), as expressed in Eq. 3. This is not trivial since:

- Intra-granular and inter-granular bubbles could have very different size and helium densities, and thus in order to calculate their pressure a wide ranged equation of state is required, or a combination of different equations of state tailored to each bubble population [28].
- The knowledge of solubility of helium at grain boundaries is limited, since the experimental knowledge about solubility in UO_2 derives from infusion in single crystals and powders, with the lack of data available for polycrystalline samples [29]. The estimation of the gas content in inter-granular bubbles is therefore strongly dependent on model assumptions.

In view of these intrinsic limitations in the general application of the model formalized in Eq. 2, we focus on the simplified version of the model applicable to the simulation of fast annealing experiments performed in vacuum conditions [25]. Despite the loss of generality, this approach allows us to assess the performance of the model with a subset of parameters and to compare its results with the experimental measurements of release rates during annealing in KEMS of doped UO_2 performed by Talip *et al.* [25].

In annealing conditions, the irradiation induced re-solution rate is null, $\alpha = 0$, whereas the condition of fast transients allows neglecting the helium production rate, $S \approx 0$, with the average intra-granular concentrations of helium initialized to $c(t) = c_0$ and $m(t) = m_0$. Moreover, the experiments being performed in vacuum (i.e., in the KEMS), the pressure at grain boundaries is assumed to be zero, $p_{\mathrm{gb}} \approx 0$, implying by Eq. 3 that $C_{S,\mathrm{gb}} = 0$. Under these assumptions and using Henry's law (Eq. 3), Eq. 2 becomes

$$\frac{\partial c}{\partial t} = D\frac{1}{r^2}\frac{\partial}{\partial r}r^2\frac{\partial}{\partial r^2}c + \beta\left(c - k_H p_{\mathrm{ig}}\right) = D\frac{1}{r^2}\frac{\partial}{\partial r}r^2\frac{\partial}{\partial r^2}c - \beta c + \beta k_H p_{\mathrm{ig}}$$
$$\frac{\partial m}{\partial t} = \beta\left(c - k_H p_{\mathrm{ig}}\right) = \beta c - \beta k_H p_{\mathrm{ig}} \quad (5)$$

in which the term $\beta k_H p_{\mathrm{ig}}$ plays the role of a thermal resolution.

By using the classic trapping rate by Ham [30]

$$\beta = 4\pi D R_{\mathrm{ig}} N_{\mathrm{ig}} \quad (6)$$

where R_{ig} (m) is the radius of intra-granular bubbles and N_{ig} (at m^{-3}) is the intra-granular bubble density, and using the equation of state derived by Van Brutzel *et al.* [28] for the intra-granular bubble pressure p_{ig} (Pa) (for the sake of completeness, the equation of state is: $p_{\mathrm{ig}} = kTZ/V_{\mathrm{at}}$, $Z = (1+y+y^2-y^3)/(1-y)^3$, $y = \pi d^3/6V_{\mathrm{at}}$, with V_{at} (m^3) = 7.8 10^{-30}, and d being the hard-sphere diameter given by d (m) = 2.973 10^{-10} [0.8414 - 0.05 log(T (K)/10.985)])

$$p_{\mathrm{ig}} = \frac{kT}{V_{\mathrm{at}}}Z \quad (7)$$

Where, k (J K^{-1}) is the Boltzmann's constant, T (K) the temperature, Z the compressibility factor, and V_{at} the atomic specific volume, i.e., $V_{\mathrm{at}} = V_{\mathrm{ig}}/n_{\mathrm{He}}$, with V_{ig} (m^3) being the intra-granular bubble volume and n_{He} (at) being the number of atoms per bubble. We can write:

$$\beta k_H p_{\mathrm{ig}} = 4\pi D R_{\mathrm{ig}} N_{\mathrm{ig}} k_H \frac{kTZn_{\mathrm{He}}}{V_{\mathrm{ig}}} = \left(4\pi D R_{\mathrm{ig}} k_H \frac{kTZ}{V_{\mathrm{ig}}}\right)\left(n_{\mathrm{He}} N_{\mathrm{ig}}\right) := \gamma m \quad (8)$$

Where γ (s^{-1}) is interpreted as a thermal re-solution rate (this definition of the thermal re-solution is dependent on the choice of the equation of state for intra-granular helium bubbles. Different equation of states will imply different formulas for γ [22]). With this notation, Eq. 5 can be written as:

$$\frac{\partial c}{\partial t} = D\frac{1}{r^2}\frac{\partial}{\partial r}r^2\frac{\partial}{\partial r^2}c - \beta c + \gamma m$$
$$\frac{\partial m}{\partial t} = \beta c - \gamma m \quad (9)$$

which is formally the homogeneous form (i.e., with no source term) of the system studied by Speight [20].

As for the model parameters to be used in Eq. 9, we adopt Ham's trapping rate β [30] (Eq. 6), the thermal re-solution rate γ defined by Eq. 8, and the diffusion coefficient D by Luzzi *et al.* [31], recommended for infused samples (the samples were estimated to have 0.04 dpa at the time it was examined, far from typical values reached in irradiated fuel), i.e.

$$D\ (\mathrm{m^2\ s^{-1}}) = 2.0\ 10^{-10}\exp(-2.12\ (\mathrm{eV})/kT) \quad (10)$$

Henry's constant is selected after the review of Cognini *et al.* [29]. We use the relation reported for single crystals, since Eq. 9 describes the solubility of helium *within* a fuel grain

$$k_H\ (\mathrm{at\ m^{-3}MPa^{-1}}) = 4.1\ 10^{24}\exp(-0.65\ (\mathrm{eV})/kT) \quad (11)$$

For the sake of comparison, we report the model for helium behaviour currently implemented in TRANSURANUS [18]. This model includes the treatment of intra-granular helium diffusion with an effective diffusivity D_{eff} acting on the total helium concentration, in line with [20,27]. The diffusion coefficient is based on the best-estimate correlation derived by Federici *et al.* [17]. The governing equation is

$$\frac{\partial(c+m)}{\partial t} = D_{\text{eff}} \frac{1}{r^2} \frac{\partial}{\partial r} r^2 \frac{\partial}{\partial r^2} (c+m) + S \tag{12}$$

with the source rate being calculated from the TUBRNP depletion module [18,32]. As for the inter-granular helium behaviour, the model assumes that above 800°C all the gas reaching the grain boundaries is released, whereas at lower temperatures the helium is trapped at the grain boundaries up to a certain saturation. In TRANSURANUS, a model describing the absorption of helium from the rod free volume is also present. This model is out of the scope of this work and is therefore not discussed.

It should be added that the effective diffusivity by Federici *et al.* [17] is the *only* parameter considered in the model of TRANSURANUS since the grain-boundary release temperature threshold and the grain-boundary retention [18] are turned off to represent the vacuum conditions in which the annealing is performed. The effective diffusion coefficient D_{eff} proposed by Federici *et al.* represents (in the model of TRANSURANUS) a combination of the single-atom diffusivity D, the trapping rate β, and the thermal and irradiation-induced re-solution rate α and γ, i.e., $D_{\text{eff}} = (\alpha + \gamma)/(\beta + \alpha + \gamma)\, D$, whereas the new mechanistic model proposed describes each of these parameters separately. Up to a certain degree, it is expected that adding physics-based parameters with considerable uncertainty [28,29,31,33] results in a limited predictive capability of the model itself. Nevertheless, the combination of the physics-based parameters should attempt to reproduce the effective diffusion coefficient by Federici *et al.*, in view of its (*i*) capability in reproducing experimental data (Fig. 2), and it (*ii*) being the best-estimate fit of several experimental diffusivity measurements [17]. This represents a development target for future work on mechanistic models.

Both the new model (Eq. 2) and the current TRANSURANUS one (Eq. 12) were implemented in SCIANTIX [15,34,35].

1.1.2 Comparison with experimental data

The goal of the separate-effect experiments performed by Talip *et al.* [25] was to investigate the helium release from UO_2 samples doped with 0.1 wt.% of additive (PuO_2) containing 66.7 wt.% of $^{238}PuO_2$, and aged 15 years. Helium desorption experiments were performed on the samples in a Knudsen Effusion Mass Spectrometry (KEMS) system connected to a Quantitative GAs MEasurement Set-up (Q-GAMES). In this technique, the helium released from the samples during the annealing is collected, purified and quantitatively measured by comparison with a known spike of gas [36].

Five annealing experiments were carried out with the temperature sequences shown in Fig. 1. These sequences are characterized by a heat up step (around 30 minutes with 10-30 K min^{-1}), followed by a holding at the annealing temperature (for 1 to 3 hours). In three out of the five annealing sequences, the temperature is decreased after the plateau, while in the two others there is a second heat up phase up to 2200 and 2300 K. For each temperature sequence, two figures of merit were analysed: the helium fractional release and the helium release rate. The helium fractional release is measured up to the end of the annealing plateau, while the helium release rate is measured continuously to the end of the annealing history (i.e., for two cases, up to 2200 and 2300 K).

The experimental measurements are supported by TEM images [25] allowing the authors to estimate the population of helium bubbles in the sample before annealing. In line with Talip *et al.* [25], we assume an initial concentration of helium single-gas atoms c_0 = 1.6 10^{24} at m^{-3} and a helium concentration trapped in intra-granular bubbles of m_0 = 8.3 10^{22} at m^{-3}. Based on the measurement of bubble size in the order of 1-2 nm, it is assumed a bubble density of 400 atoms per bubbles, resulting in a number density of N_{ig} = 2.08 bubbles m^{-3} intra-granular bubbles. These values are used for the initialization of the helium behaviour model in SCIANTIX. The selection of the other model parameters (helium diffusivity and solubility) is described in the previous section. Besides these parameters, we briefly recall that since the annealing is performed in vacuum conditions, we assume zero retention of helium at the grain boundaries. Moreover, we neglect the source term because of the short duration of the annealing histories.

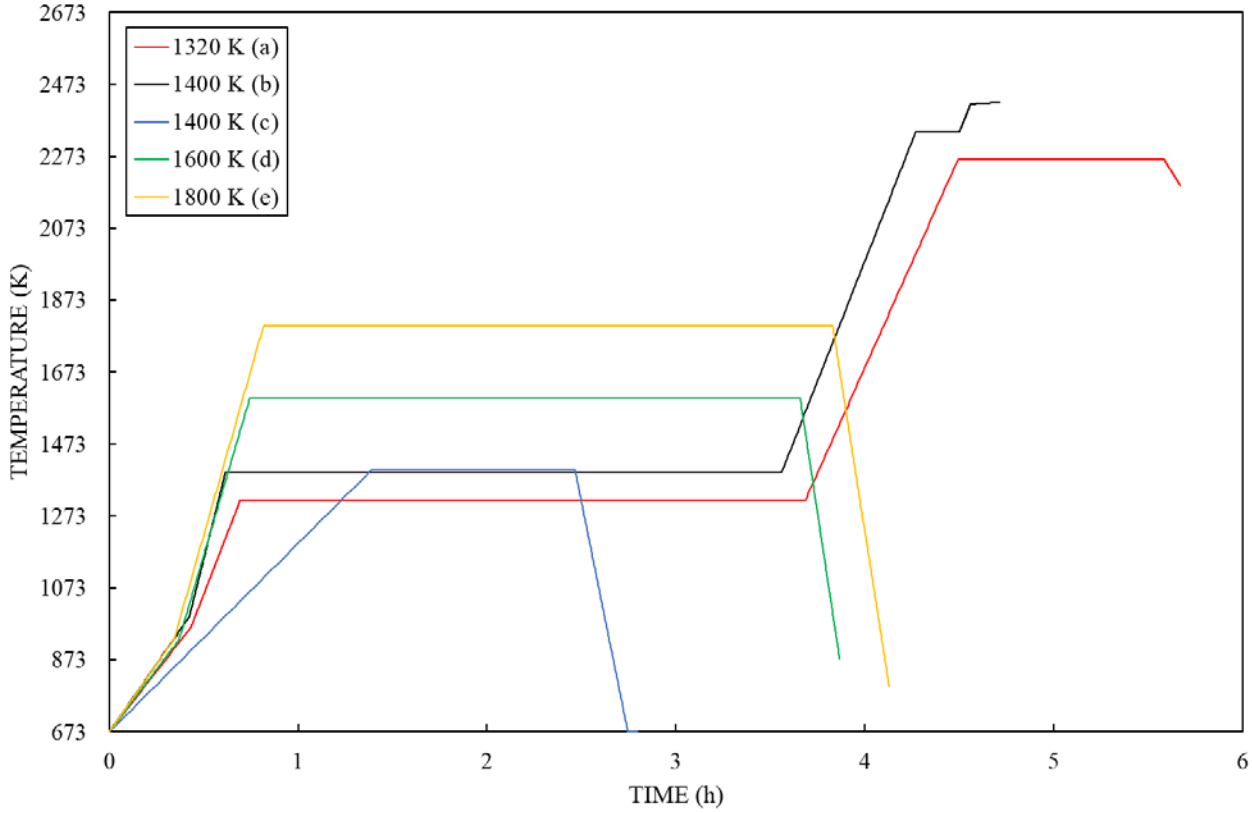

Figure 1: Temperature histories of the annealing experiments considered [25].

Since the grain size, a (m), and its evolution affect helium behaviour (e.g., via the diffusion rate D/a^2 (s^{-1}) and the grain-boundary sweeping) Talip *et al.* [25] measured the grain size before and after the annealing experiments, reporting a general trend of strong grain growth. In order to attempt to account for this effect, the grain growth and the consequent grain boundary sweeping were included in SCIANTIX: we use the Van Uffelen *et al.* grain growth model [37] and the model present in TRANSURANUS for the swept volume fraction [38].

Figures 2 and 3 collect the results of the SCIANTIX simulations using both the new helium behaviour model and the model already available in TRANSURANUS. The simulation results are compared with the experimental release in terms of helium fractional release (Fig. 2) and of helium release rate (Fig. 3).

It can be seen in Fig. 2 that both the current TRANSURANUS model and the newly proposed model exhibit a satisfactory agreement with the experimental results [39]. The mean square errors calculated between the simulation results and the experimental data are reported in Table 1, and quantitatively

confirm this observation. Despite adopting an effective treatment of helium diffusivity, the TRANSURANUS model catches both the kinetics and the integral values of the helium release remarkably well for all annealing temperatures considered.

Figure 3 reports the comparison of the simulation results with the experimental data in terms of helium release as function of temperature. For the annealing sequences with the first plateau at 1320 K (Fig. 3a) and 1400 K (Fig. 3b) two distinct peaks can be observed. Beside the relatively poor quantitative agreement, both the new proposed model and the TRANSURANUS model correctly predict the onset of both release-rate peaks in this annealing transient. This is particularly important since this two-peaked release-rate evolution has been ascribed to the mobility of helium intra-granular bubbles [25], which is not considered in the herein presented models. It could be said that since the description by Federici *et al.* is *effective*, it includes already also the mobility of intra-granular bubbles. The coefficient proposed by Federici *et al.* is Arrhenius-like, i.e., $D_{\text{eff}} = D_0 \exp(-E/kT)$ with E being the activation energy, $1/kT$ the Boltzmann's factor and D_0 a pre-exponential, while it is expected that the motion of intra-granular bubbles should have a specific activation energy, different from that of single atoms. In the present description, for these two cases, the second peak is caused by the rise in temperature of the annealing transient (Fig. 1) and the consequent increase in the diffusion rate of helium towards the grain boundaries, together with a strong grain growth and the associated grain boundary sweeping. It is worth noting that grain boundary sweeping plays a major role in the formation of the second peak and therefore it is crucial to include this effect not to underestimate this peak (Fig. 4).

Figure 3e shows the highest temperature plateau analysed, i.e., the annealing sequence with the first plateau at 1800 K (Fig. 1, yellow curve). This case shows two release-rate peaks, with an almost 100% helium fractional release (Fig. 2e). Both the peaks are observed during the heat up phase of the annealing. This behaviour suggests the activation of a second release mechanism with an activation energy higher than that of either the diffusivity of single atoms by Luzzi *et al.* [31] or the effective diffusivity by Federici *et al.* [17], since the temperature of 1800 K is not sufficient for a significant grain growth. The new proposed mechanistic model is unable to catch this second peak at higher temperature, despite the additional parameters compared to the current TRANSURANUS model. With suited parameters, the model itself could explain a two-peak release behaviour. A possible mechanism could be in a first stage the diffusion of single atoms activates, leading to trapping of gas at intra-granular bubbles and to diffusion towards the grain boundaries – i.e., causing the first release peak; then at higher temperature, the thermal resolution becomes dominant compared to trapping and hence helium is resolved in the matrix and becomes available for diffusion leading to the second peak. This hypothetical evolution of intra-granular helium is not predicted by the model since thermal resolution is dominant at lower temperatures compared to trapping. Consequently, the helium is resolved from intra-granular bubbles and then (at higher temperature) diffuses towards the grain boundaries, resulting in a single release peak.

It appears that the most critical parameter is the thermal resolution. This can be deduced from the fact that the activation of the diffusivity proposed by Luzzi *et al.* [31] is similar to that proposed by Federici *et al.* [17], and consequently both the models considered are able to predict correctly the onset of the first peak. The thermal resolution term on the contrary contains both the equation of state of intra-granular bubbles (which is not trivial to address [28]) and Henry's constant, on which a very limited and spread experimental dataset is available [29].

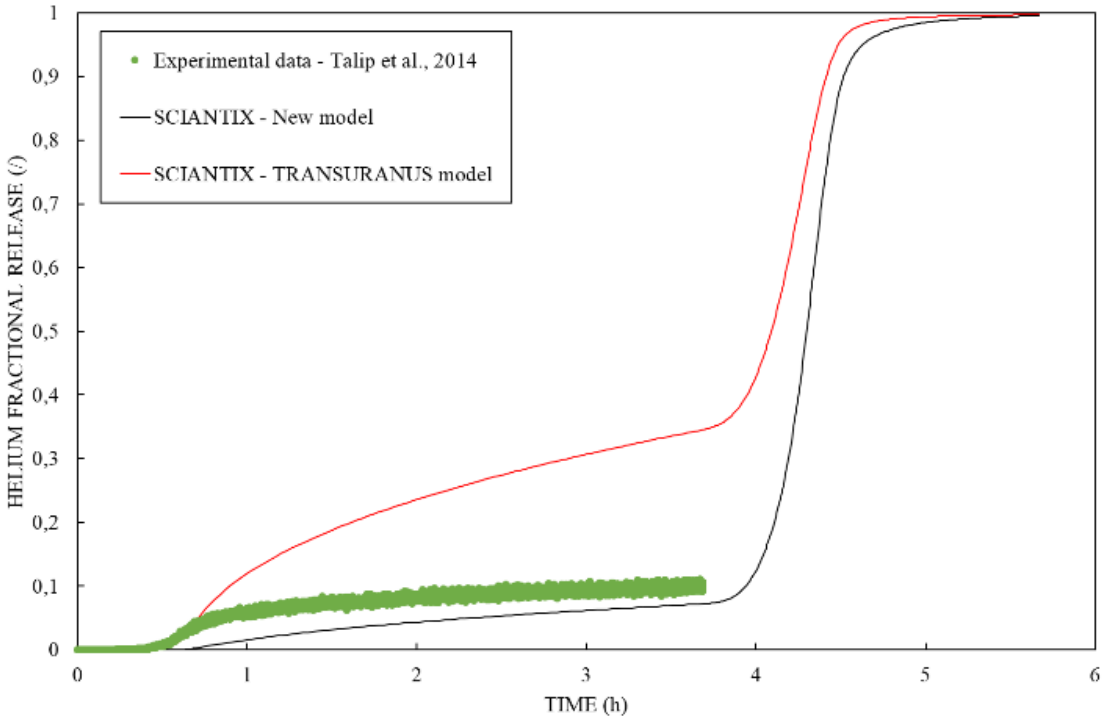
Experimental data - Talip et al., 2014
SCIANTIX - New model
SCIANTIX - TRANSURANUS model
HELIUM FRACTIONAL RELEASE (/)
TIME (h)
0
0,1
0,2
0,3
0,4
0,5
0,6
0,7
0,8
0,9
1
0
1
2
3
4
5
6

(a)

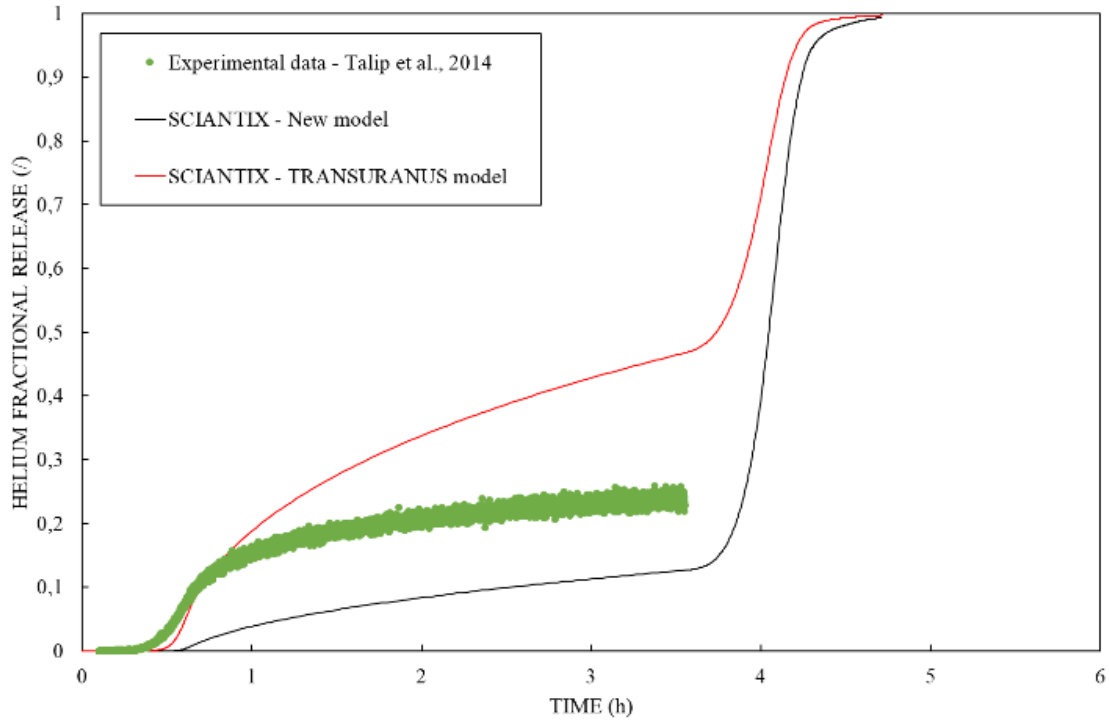
Experimental data - Talip et al., 2014
SCIANTIX - New model
SCIANTIX - TRANSURANUS model
HELIUM FRACTIONAL RELEASE (/)
TIME (h)
0
0,1
0,2
0,3
0,4
0,5
0,6
0,7
0,8
0,9
1
0
1
2
3
4
5
6

(b)

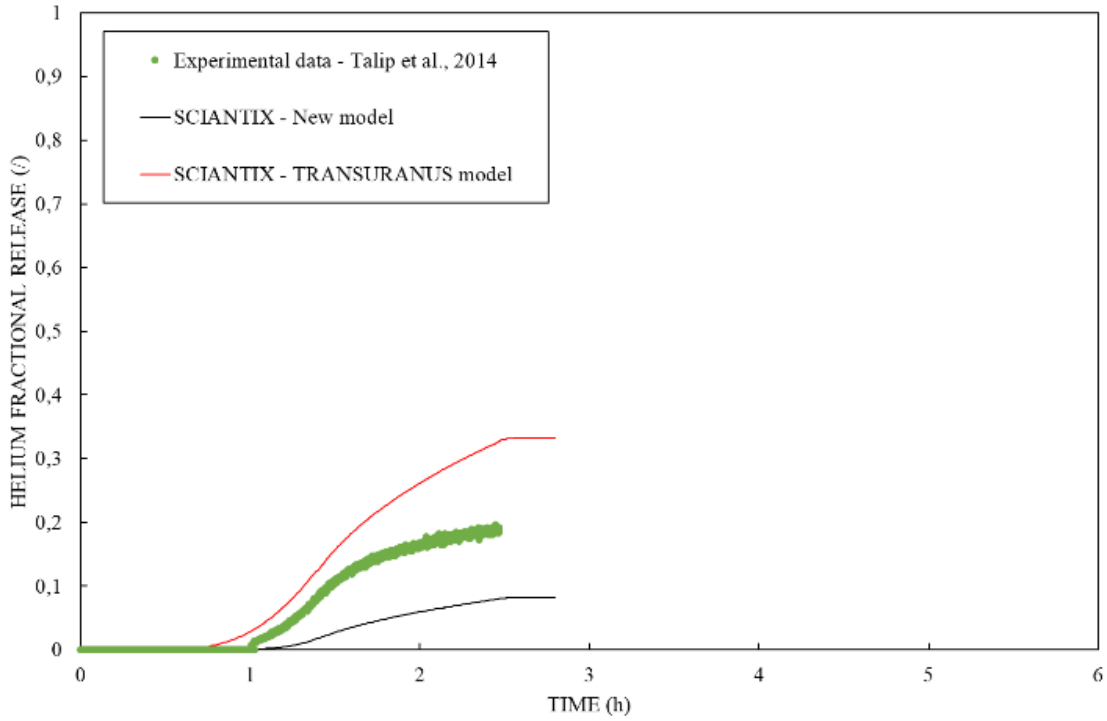
Experimental data - Talip et al., 2014
SCIANTIX - New model
SCIANTIX - TRANSURANUS model
HELIUM FRACTIONAL RELEASE (-)
TIME (h)
0
0,1
0,2
0,3
0,4
0,5
0,6
0,7
0,8
0,9
1
0
1
2
3
4
5
6

(c)

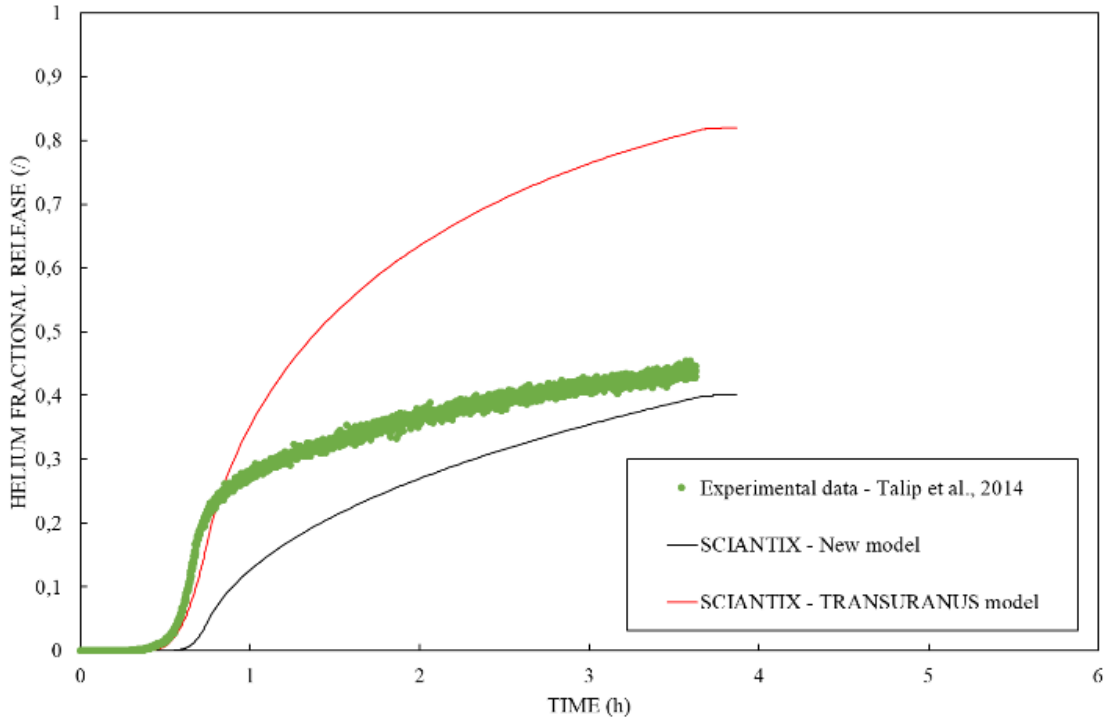
Experimental data - Talip et al., 2014
SCIANTIX - New model
SCIANTIX - TRANSURANUS model
HELIUM FRACTIONAL RELEASE (-)
TIME (h)
0
0,1
0,2
0,3
0,4
0,5
0,6
0,7
0,8
0,9
1
0
1
2
3
4
5
6

(d)

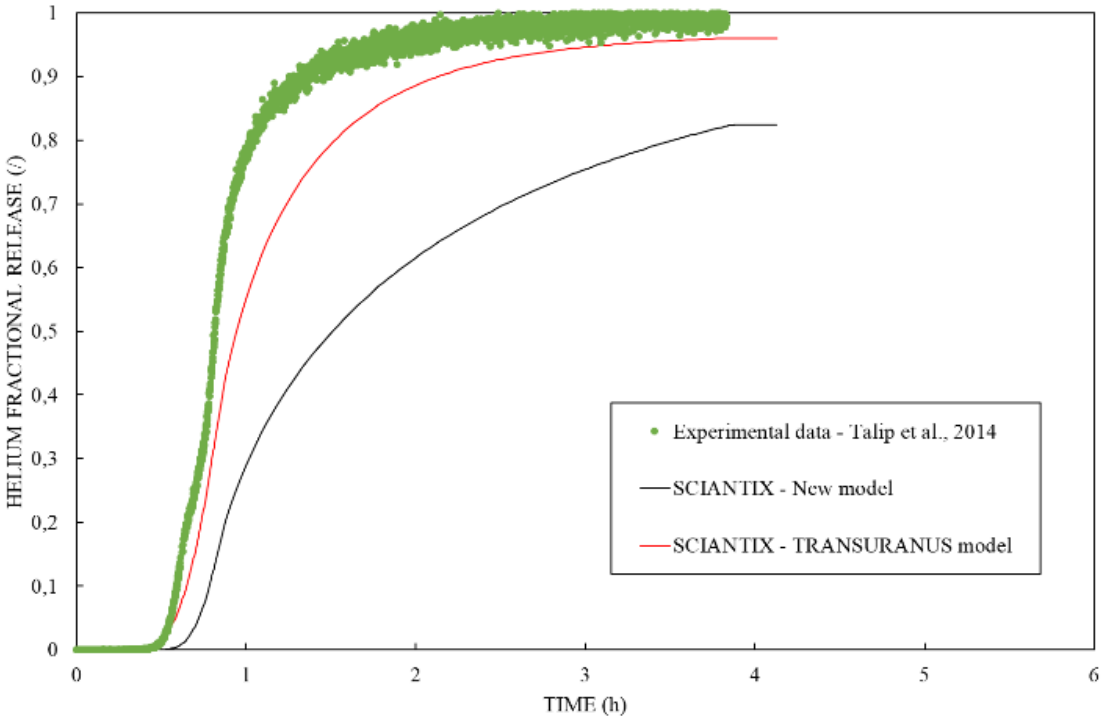

(e)

Figure 2: Comparison of SCIANTIX results (new helium model and current TRANSURANUS model) with experimental helium fractional release from [25]. Each subfigure corresponds to an annealing sequence referred to by the temperature of its first plateau (a) 1320 K, (b) 1400 K, (c) 1400 K, (d) 1600 K, and (e) 1800 K , respectively (see Fig. 1).

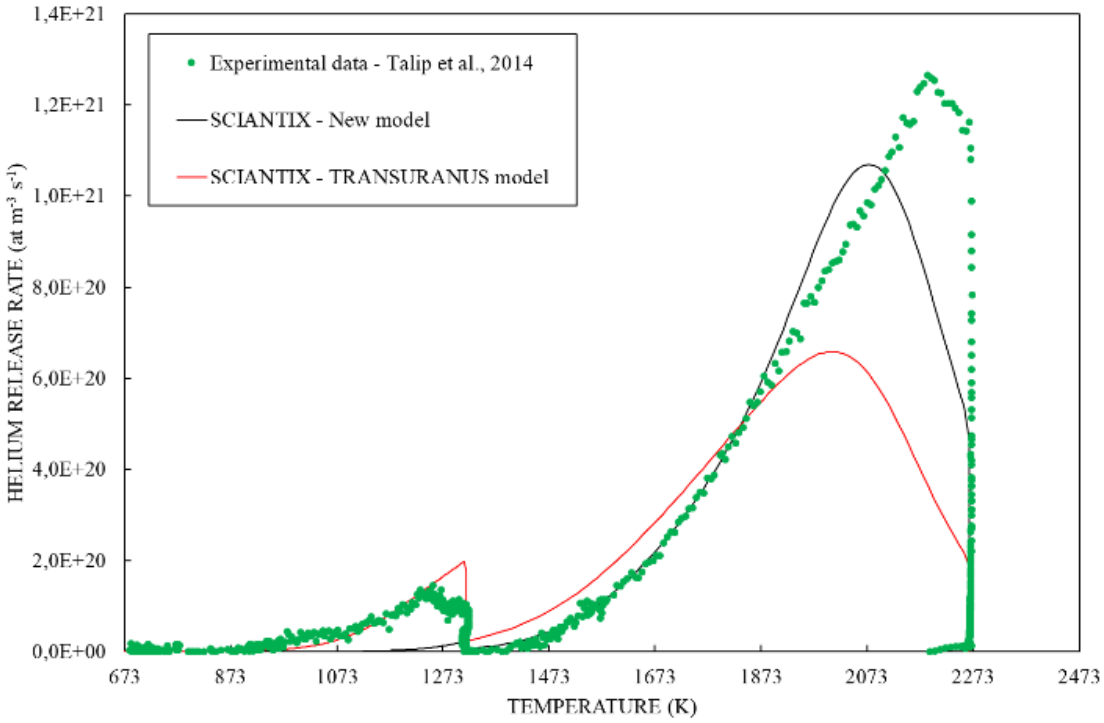

(a)

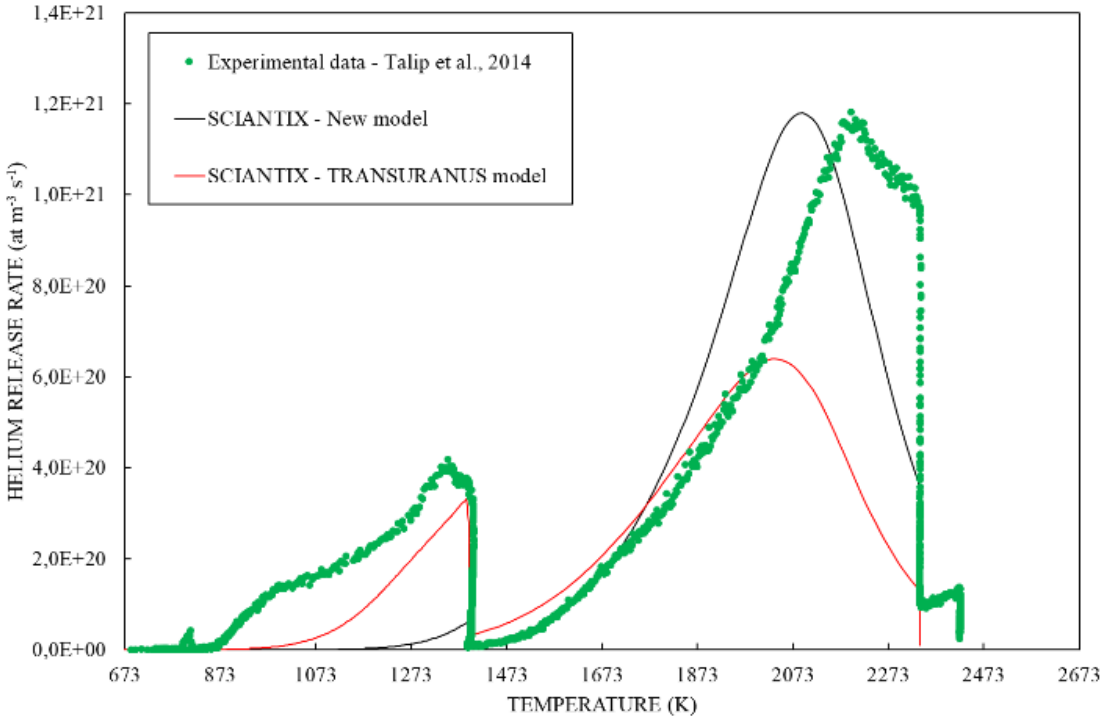
Experimental data - Talip et al., 2014
SCIANTIX - New model
SCIANTIX - TRANSURANUS model
HELIUM RELEASE RATE (at m-3 s-1)
1,4E+21
1,2E+21
1,0E+21
8,0E+20
6,0E+20
4,0E+20
2,0E+20
0,0E+00
673
873
1073
1273
1473
1673
1873
2073
2273
2473
2673
TEMPERATURE (K)

(b)

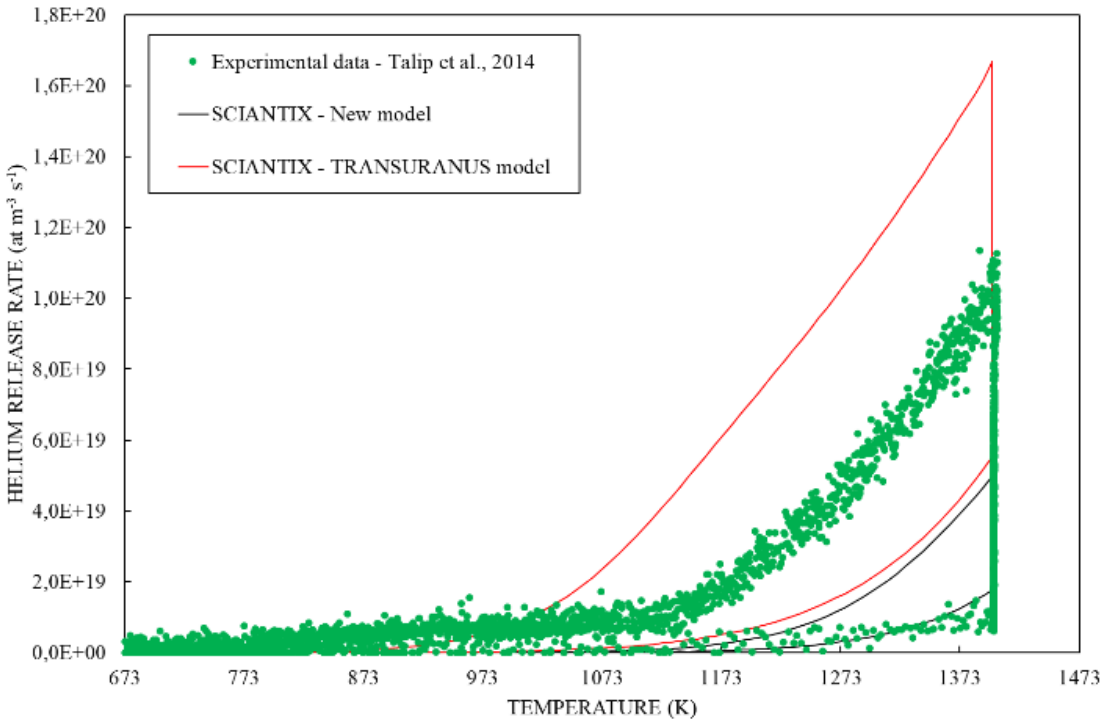
Experimental data - Talip et al., 2014
SCIANTIX - New model
SCIANTIX - TRANSURANUS model
HELIUM RELEASE RATE (at m-3 s-1)
1,8E+20
1,6E+20
1,4E+20
1,2E+20
1,0E+20
8,0E+19
6,0E+19
4,0E+19
2,0E+19
0,0E+00
673
773
873
973
1073
1173
1273
1373
1473
TEMPERATURE (K)

(c)

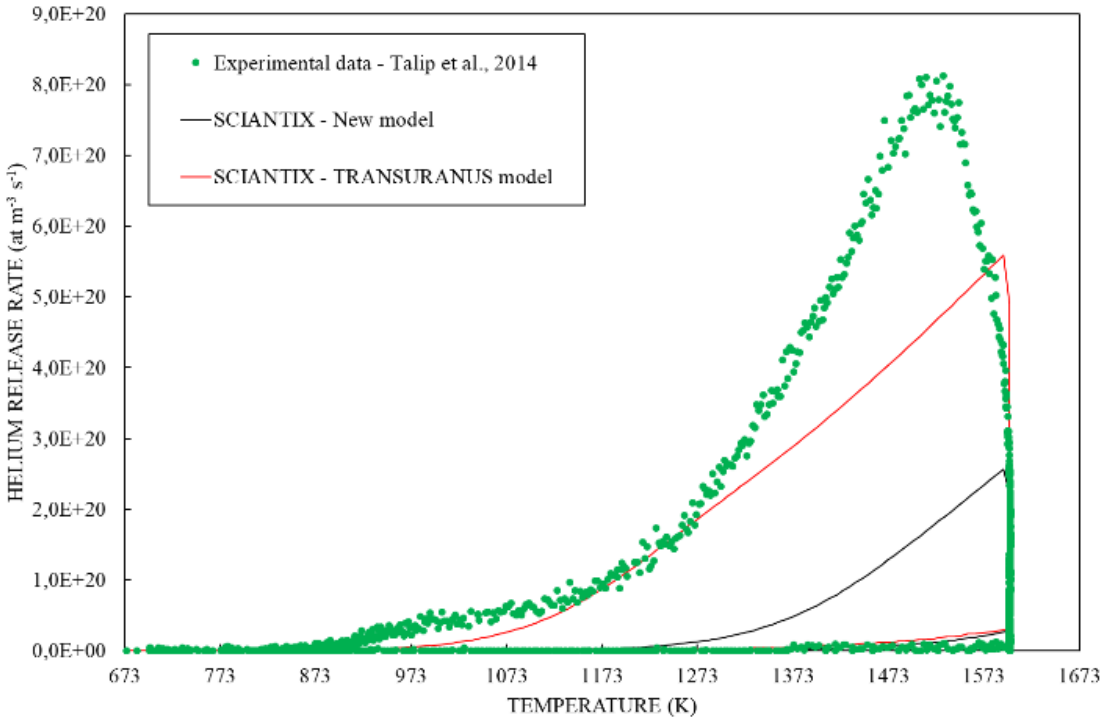

(d)

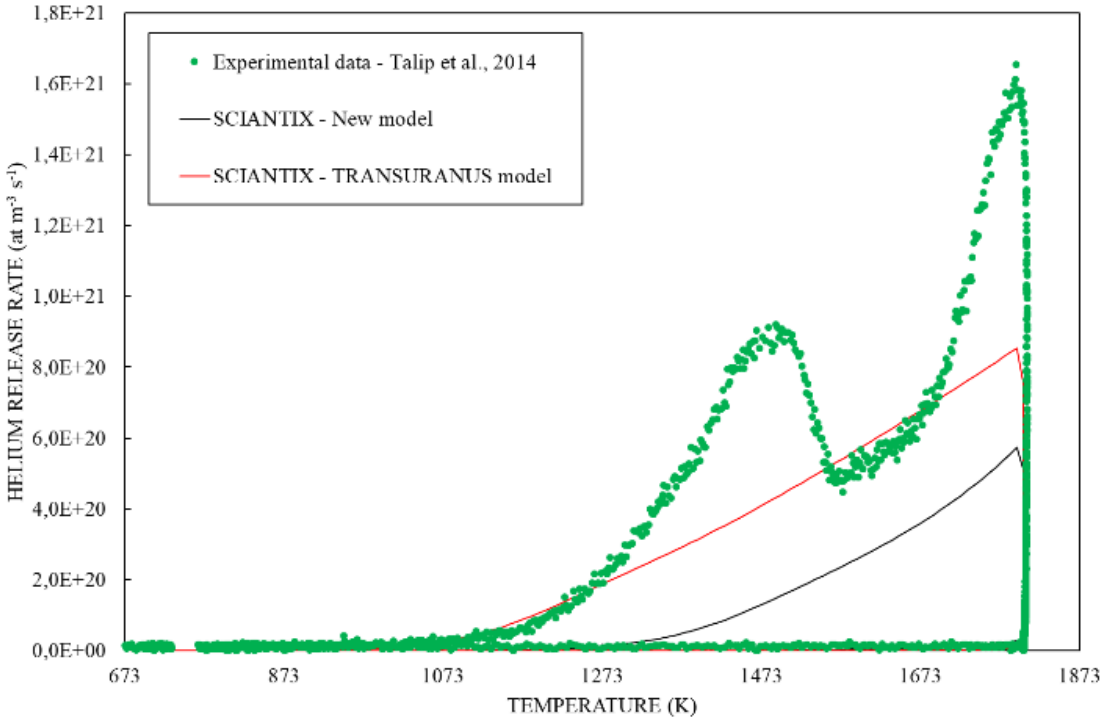

(e)

Figure 3: Comparison of SCIANTIX results (new helium model and current TRANSURANUS model) with experimental helium release rate from [25]. Each subfigure corresponds to an annealing history which is referred to by the temperature of its first plateau, respectively (a) 1320 K, (b) 1400 K, (c) 1400 K, (d) 1600 K, and (e) 1800 K (see Fig. 1).

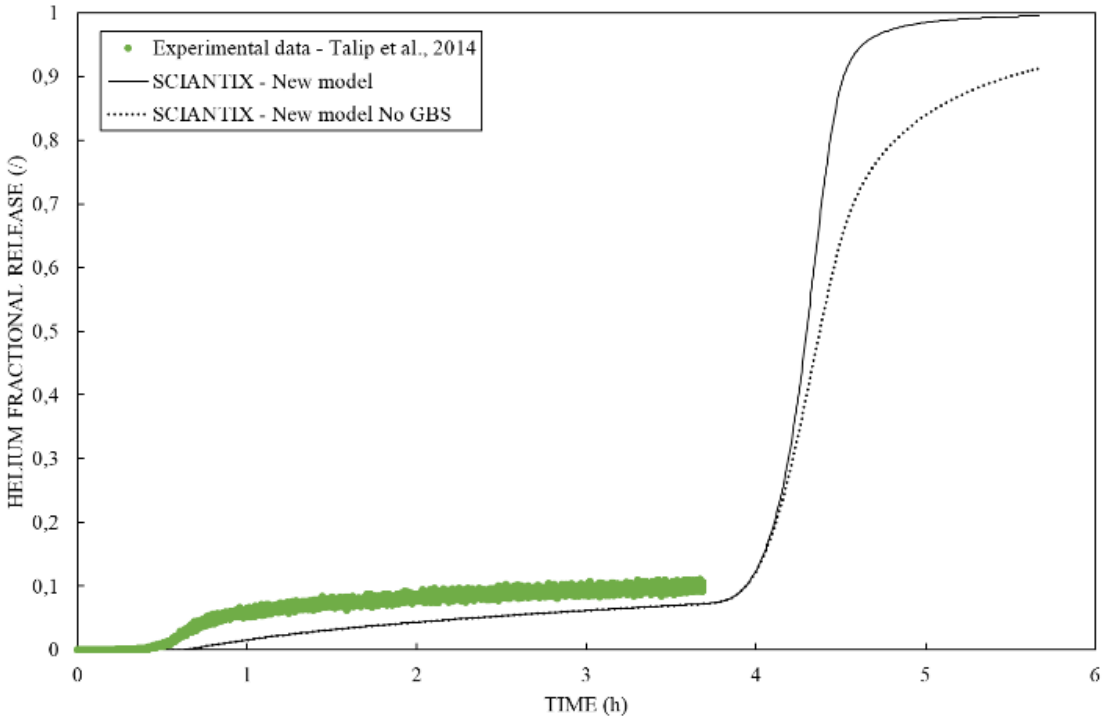

(a)

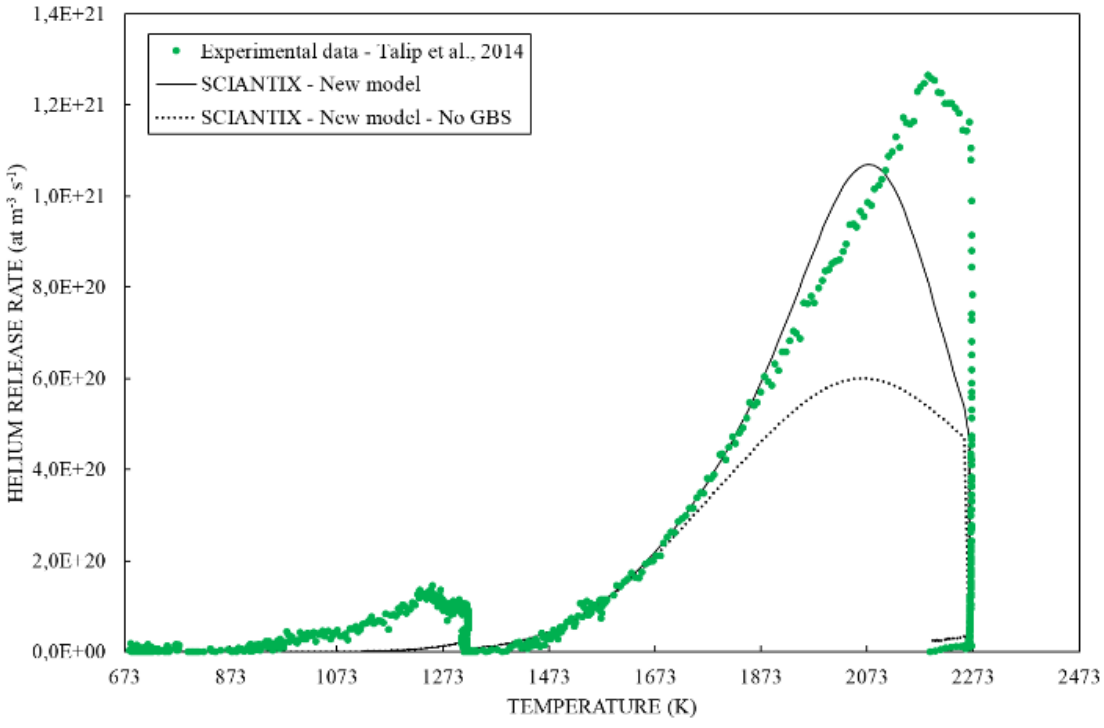

(b)

Figure 4: Comparison of SCIANTIX results (new helium model), including and excluding grain boundary sweeping (GBS), with experimental data from [25]. Each subfigure corresponds to the 1320K temperature history, respectively (a) fractional helium release and (b) helium release rate.

Table 1: Validation metric (mean square error) for the comparison of the simulation results with the experimental data by Talip *et al.* [25] in terms of helium fractional release (see Figs. 1 and 2). Lower values of the validation metric correspond to a better agreement.

Annealing history	Current TRANSURANUS model	New mechanistic model
1320 K (a)	1.48	0.74
1400 K (b)	0.64	0.76
1400 K (c)	0.76	0.69
1600 K (d)	0.62	0.64
1800 K (e)	0.28	0.57

1.2 Helium production rate

In this section, we present the new depletion model embedded in SCIANTIX. The main reason for the development of such a module is to have the capability to predict the evolution of actinides in MOX fuel in fast reactor conditions since they represent a relevant helium source. This depletion model relies on average microscopic cross-section lookup tables generated via SERPENT high-fidelity calculations and involves the online solution of Bateman's equations for a subset of relevant actinides. The results are verified in terms of the evolution of actinide and helium concentrations for MOX fuel in fast reactor conditions by comparing them with the high-fidelity results from SERPENT. Moreover, the results are compared to those of TUBRNP, a depletion module tailored to the evaluation of relative radial power and burn-up profiles in fuel performance codes and currently used in TRANSURANUS.

This model is described in *A. Cechet, S. Altieri, T. Barani, L. Cognini, S. Lorenzi, A. Magni, D. Pizzocri, L. Luzzi, "A new burn-up module for application in fuel performance calculations targeting the helium production rate in (U,Pu)O_2 for fast reactors", Submitted to Nuclear Engineering and Technology.*

1.2.1 Model description

Several state-of-the-art dedicated depletion codes allow tracking the evolution of the nuclides inventory, e.g., Monte Carlo neutronic codes like SCALE [40]. Despite the high accuracy in the numerical methods and the results, depletion codes are not affordable in the frame of fuel performance simulations. Nonetheless, depletion models need to be embedded in fuel performance codes to keep track of the evolution of nuclides relevant for heat generation by fission, finally determining the relative radial power profile. The traditional simplifying approach used in these depletion models is the definition of macroscopic cross-sections representative of different reactor types and neutron spectra (e.g., SFR, LFR). Up to now, there is no standard methodology for generating these macroscopic cross-sections, and various neutronics codes (e.g., SCALE, MONTEBURNS, SERPENT) have been applied for this purpose. In the TUBRNP model (the depletion model adopted in TRANSURANUS), important steps to include the production of helium were taken by Botazzoli *et al.* [41], with a recent extension to Th-based LWR fuels by Tijero *et al.* [42]. It should be underlined that a direct coupling of the SERPENT and TRANSURANUS code was developed for the simulation of Gd-doped UO_2 in the frame of the ESSANUF project, and that a similar coupling in the open source SALOME platform for nuclear reactor simulations is under development in the frame of the McSAFE project.

The herein presented depletion model is designed:

- To predict the helium production inside a MOX fuel grain in fast reactor irradiation conditions since the initial enrichment in plutonium nuclides leads to a higher content of α-emitters in MOX fuel with respect to UO_2.
- To yield a reliable estimation of the actinide evolution, which is a critical predictive capability for fuel performance codes even if it is not strictly an objective of Task 6.1 of INSPYRE [32,43].

The methodology adopted consists in coding multi-dimensional lookup tables for each relevant cross-section. The values are obtained from SERPENT with reaction rates calculation [44]. This methodology has been applied to MOX fuel in two different reactor conditions: sodium fast reactor (MOX/SFR) and lead-bismuth eutectic fast reactor (MOX/LBE-FR).

The depletion model accounts for the three main processes of helium production: (n,α) reactions on O_{16}, a fraction of ternary fissions, and α-decays of actinide elements [17]. Botazzoli *et al.* [41] showed that the transuranic elements up to Cm_{245} are sufficient for a satisfactorily description of helium formation due to α-decays. This translates in the following equation in this model:

$$\begin{aligned}\frac{\mathrm{d}}{\mathrm{dt}}[\mathrm{He}_4] &= \lambda_{\alpha,\mathrm{U}_{234}}[\mathrm{U}_{234}] + \lambda_{\alpha,\mathrm{U}_{235}}[\mathrm{U}_{235}] + \lambda_{\alpha,\mathrm{U}_{236}}[\mathrm{U}_{236}] + \lambda_{\alpha,\mathrm{U}_{238}}[\mathrm{U}_{238}] \\ &+ \lambda_{\alpha,\mathrm{Np}_{237}}[\mathrm{Np}_{237}] \\ &+ \lambda_{\alpha,\mathrm{Pu}_{238}}[\mathrm{Pu}_{238}] + \lambda_{\alpha,\mathrm{Pu}_{239}}[\mathrm{Pu}_{239}] + \lambda_{\alpha,\mathrm{Pu}_{240}}[\mathrm{Pu}_{240}] + \lambda_{\alpha,\mathrm{Pu}_{242}}[\mathrm{Pu}_{242}] \\ &+ \lambda_{\alpha,\mathrm{Am}_{241}}[\mathrm{Am}_{241}] + \lambda_{\alpha,\mathrm{Am}_{243}}[\mathrm{Am}_{243}] \\ &+ \lambda_{\alpha,\mathrm{Cm}_{242}}[\mathrm{Cm}_{242}] + \lambda_{\alpha,\mathrm{Cm}_{243}}[\mathrm{Cm}_{243}] + \lambda_{\alpha,\mathrm{Cm}_{244}}[\mathrm{Cm}_{244}] + \lambda_{\alpha,\mathrm{Cm}_{245}}[\mathrm{Cm}_{245}] \\ &+ {}^{O_{16}}\overline{\sigma_{n,\alpha}}\bar{\phi}[\mathrm{O}_{16}] + y_{\mathrm{TF}}\dot{F}\end{aligned} \tag{13}$$

Where, $[X_i]$ (at m^{-3}) is the concentration of the nuclide X_i, λ_{α,X_i} (s^{-1}) is the alpha decay constant of the nuclide X_i, ${}^{O_{16}}\overline{\sigma_{n,\alpha}}$ (m^2) is the energy-averaged cross-section for the (n,α) reaction on O_{16}, $\bar{\phi}$ (m^{-2} s^{-1}) is the local energy-averaged neutron flux (see Eq. 14), y_{TF} is the ternary fission yield of helium, set equal to 0.22% [45], and $\dot{F}$ (fiss m^{-3} s^{-1}) is the local fission rate. As can be seen in Eq. 13, to have a reliable estimation of the helium source, we considered a selected set of actinides. To follow the evolution of these actinides, a total of 23 nuclides needs to be considered (Fig. 5). Not all of the neutron reactions (especially neutron multiplication reactions) are considered in the depletion model, since the inclusion of all of them would have implied a rise in the computational time not justified by a significant improvement in the accuracy of the results.

In the present depletion model, the estimation of the local neutron flux feeding the Bateman equations is carried out based on the fission rate density, based on the relation

$$\dot{F} = \overline{\Sigma_f}\bar{\phi} \tag{14}$$

where $\dot{F}$ (fiss m^{-3} s^{-1}) is the fission rate and $\overline{\Sigma_f}$ (m^{-1}) is the one-group macroscopic fission cross-section and $\bar{\phi}$ (m^{-2} s^{-1}) is the energy-averaged local neutron flux. To evaluate the one-group macroscopic fission cross-section, the following assumption is adopted [46]:

$$\overline{\Sigma_f} = \sum_{i=1}^{k} {}^{X_i}\bar{\sigma}_f\,[X_i] \tag{15}$$

in which ${}^{X_i}\bar{\sigma}_r$ (m^2) is the microscopic, energy averaged fission cross-sections of the nuclide X_i.

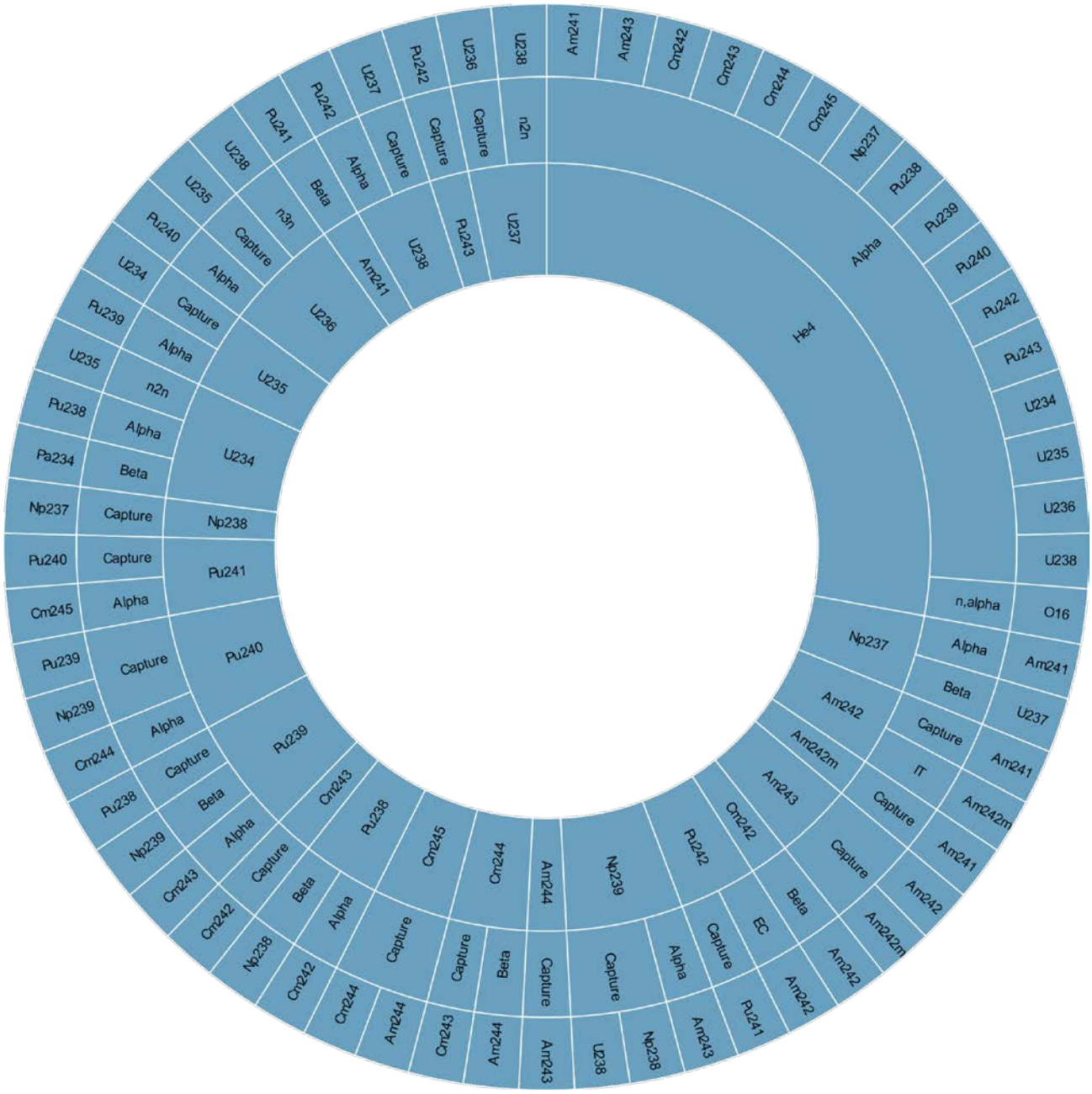

Figure 5: Father-to-daughter relations between the 23 actinide nuclides tracked in the depletion model. The inner and the outer circles contain the daughter and parent nuclide, respectively. In the middle circle the relation (i.e., type of nuclear reaction) between the parent and the daughter nuclides is indicated.

The methodology used to build the herein presented depletion model parameters (i.e., the values of the energy-averaged cross-sections) is depicted in the upper part of Fig. 6:

1. Run a set of SERPENT calculations with different initial fuel compositions, representative for the analysed fuel/reactor combination.
2. For each initial Pu/HM enrichment e_0, collect the values of the energy-averaged microscopic cross-sections at different burn-up values (e.g., *bu* (GWd/t_{HM}) = 0, 5, 10, 15, …), evaluated by the reaction rate integrals in SERPENT.

3. Each microscopic cross-section is therefore characterized at discrete sampling points as a function of initial enrichment e_0 and local burn-up bu, i.e., the energy-averaged cross-section for reaction r of nuclide X_i will be a discrete function ${}^{X_i}\bar{\sigma}_r(e_0, bu)$.
4. These discrete functions are hard-coded as two-entry lookup tables in SCIANTIX.

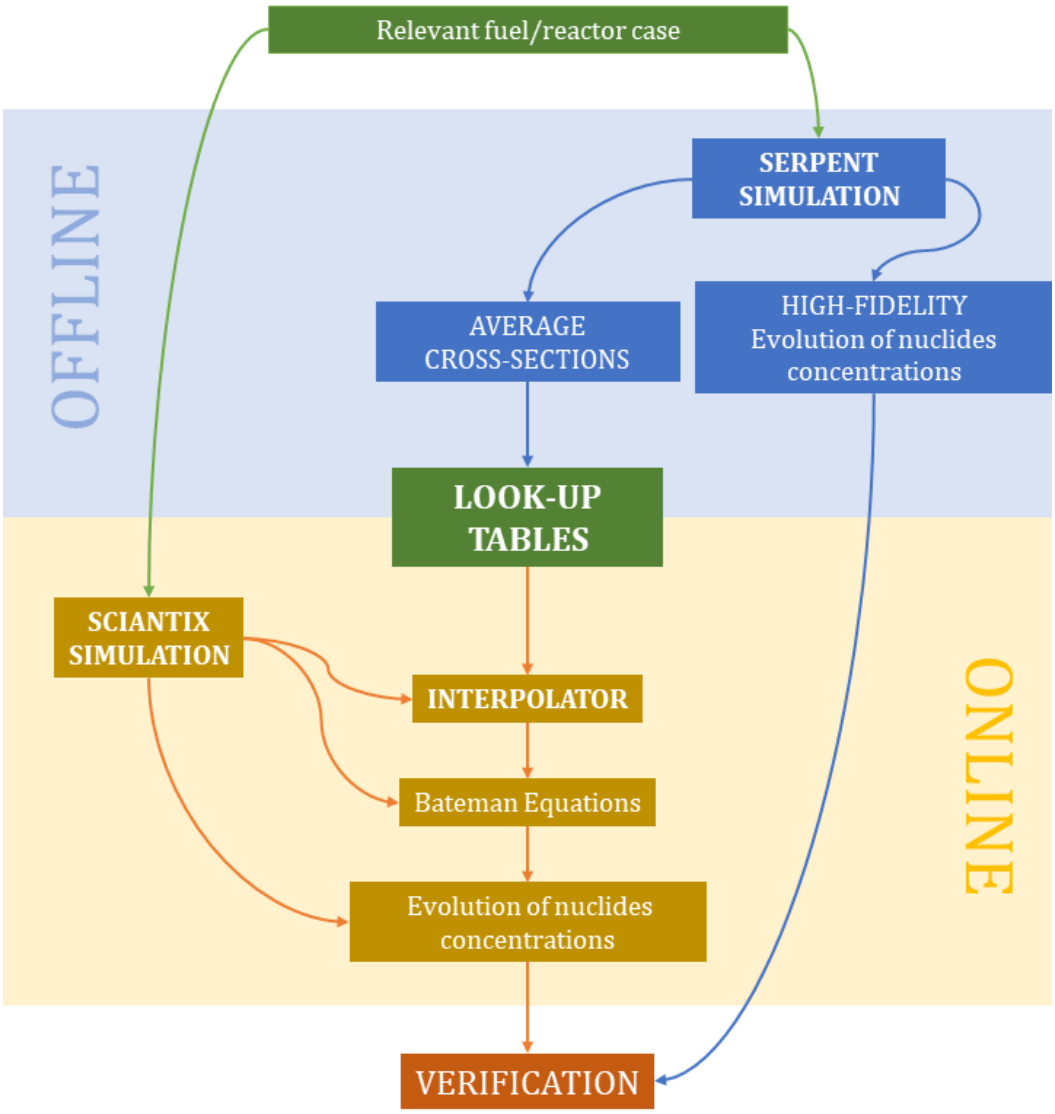

Figure 6: Methodology applied for the generation of the cross-section lookup tables by SERPENT (offline), the solution of the depletion calculation in SCIANTIX (online) and the consequent comparison of the results (verification).

These steps are to be performed once and for all and hence referred to as offline operations. The set of Bateman equations is solved by SCIANTIX (online, lower part of Fig. 6), or equivalently by SCIANTIX coupled with a fuel performance code. This online calculation requires an interpolation within the cross-section values in the lookup tables in terms of initial Pu/HM enrichment and current burn-up. This interpolation is computationally inexpensive, but brings about additional information with respect to using a fixed value for the cross-sections during the all irradiation [41,47,48]. These tables depend on the fuel/reactor combination, since the energy-averaged cross-sections strongly depend on the neutron energy spectrum, which in turn is determined by the whole reactor characteristics. Together with the decay constants, these lookup tables constitute the required information to calculate each parameter in the depletion model.

1.2.2 Verification against high-fidelity simulations

The main features and options used to build the SERPENT simulations in the three fuel/reactor cases herein analysed are reported in Tables 2 and 3.

Table 2: SERPENT input parameters used for the generation of the lookup tables.

Parameter	MOX/SFR	MOX/LBE-FR
External Pellet radius (mm)	2.71	2.71
Radial gap (mm)	0.115	0.115
U/HM	80-60[a]	80-60[a]
Pu/HM	20-40[b]	20-40[b]
Enrichment width (at/HM%)	2	2
O/HM	1.97	1.97
Fuel density (g cm^{-3})	10.97	10.97
Column length (mm)	650	650
Cladding material	15-15 Ti SS	15-15 Ti SS
Cladding thickness	0.45	0.45
Cladding density (g cm^{-3})	7.95	7.95
Coolant	Sodium	Lead Bismuth Eutectic
Coolant prism side (mm)	6.7	6.7
Coolant prism height (mm)	670	670
Coolant density (g cm^{-3})	0.61[c]	10.28[c]
Total burn-up (GWd/t_{HM})	200	200
Burn-up width (GWd/t_{HM})	5	5
Burn-up steps	41	41
Power density (kW kg^{-1})	40	40

[a]: Assumed natural uranium isotopic composition.
[b]: Pu^{238}/Pu 2.332%, Pu_{239}/Pu 56.873%, Pu_{240}/Pu 26.997%, Pu_{241}/Pu 6.105%, Pu_{242}/Pu 7.693% (wt.%).
[c]: From Sobolev [51].

Table 3: Input settings used for the SERPENT simulations.

Command	Description	Values
set pop	Sets parameters for simulated neutron population in criticality source mode. NPG: number of neutrons per generation NGEN: number of active generations NSKIP: number of inactive generations	NPG = 10'000 NGEN = 100 NSKIP = 30
set ures	Sets unresolved resonance probability table sampling on or off. OPT: option to switch probability table sampling on (1/yes) or off (0/no)	OPT = 1
set bc	Sets the boundary conditions for all outer boundaries of the geometry.	Reflective boundary condition
set bumode	Sets the burn-up calculation mode.	CRAM
set pcc	Sets the time integration method in burn-up calculation. MODE: time integration method. SSP: number of sub-steps for predictor steps SSC: number of sub-steps for corrector steps	MODE = LELI SSP = 30 SSC = 30

set xcalc	Calculation mode for transmutation cross-sections. We use spectrum-collapse mode.	
set egrid	Sets the unionized energy grid reconstruction parameters. TOL: fractional reconstruction tolerance EMIN: minimum energy in the grid (MeV) EMAX: maximum energy in the grid (MeV)	TOL = $5 \cdot 10^{-5}$ EMIN = 10^{-9} EMAX = 15
set powdens	Sets normalization to power density. PDE: power density (in kW g^{-1})	PDE = $4 \cdot 10^{-2}$

In SERPENT, the absolute value of the reaction rate integrals depends on source normalization. In this work, for each test case, we used a power density of 40 kW kg^{-1} (which corresponds to a fission rate of $1.32 \cdot 10^{19}$ fiss m^{-3} s^{-1}, assuming 208 MeV $fiss^{-1}$) to normalize the source. We calculated energy-averaged cross-sections as

$$ {}^{X_i}\bar{\sigma}_r(e_0, bu) = \frac{\int_V \int_0^\infty {}^{X}\sigma_r(e_0, bu, E)\phi(\mathbf{r}, E) d^3 r dE}{\int_V \int_0^\infty \phi(\mathbf{r}, E) d^3 r dE} \quad (16) $$

Where, X_i, e_0 and bu are respectively the considered target nuclide, the initial enrichment and the burn-up, and ${}^{X_i}\sigma_r(e, bu, E)$ (m^2) is the microscopic cross-section, which is a function of burn-up bu, initial fuel enrichment $e_0$and incident neutron energy E , while $\phi(\mathbf{r}, E)$ (m^{-2} s^{-1} eV^{-1}) is the neutron flux per energy as function of the neutron energy E and space.

The other results we obtained using SERPENT are the helium and actinide concentrations as a function of burn-up and initial enrichment of Pu/HM. The results of these high-fidelity simulations will serve as comparison in the assessment phase of the depletion model.

The geometry used in the SERPENT simulation is a cylindrical geometry (fuel pellet) in a prismatic space (coolant) with a reflective boundary condition on the coolant external surface. The calculation is performed for a single fuel rod. In both the MOX/SFR and MOX/LBE-FR cases the initial fuel composition is chosen based on standard nuclides compositions which would likely be similar to those adopted in the Gen-IV ESFR and MYRRHA concepts [49]. As for the cladding material, it is 15-15 Ni-Cr, Ti stabilized, stainless steel for both the MOX/SFR and MOX/LBE-FR cases.

The depletion calculation in SERPENT is performed in 41 equally distanced burn-up steps. The initial fuel composition foresees a value of enrichment from 20 % to 40 % with steps of 2 % in both cases. The initial neutron population is set to 10'000 for both cases, with 100 active neutron generations and 30 inactive generations. The solution of the burn-up matrix is achieved through the Chebyshev Rational Approximation Method [50], while we use linear extrapolation as predictor method and linear interpolation as corrector method for what concern the time integration method in burn-up calculations.

To assess the proposed depletion model, we carried out in SCIANTIX the same simulations described in Table 2. The results shown refer to a Pu/HM concentration of 20% for both MOX/SFR and MOX/LBE-FR cases. The irradiation lasts approximately 106'000 hours (12 years) for both cases. Table 4 reports the main SCIANTIX input parameters.

The results of SCIANTIX are compared also to those of TUBRNP (TRANSURANUS version v1m1j18), the burn-up model implemented in TRANSURANUS that is tailored to the evaluation of relative radial profiles. It is worth noting that, aside from specific cases such as Gd-doped fuels in VVER reactors, TURBNP adopts burnup-independent microscopic cross sections. As proven by the example for Gd-doped fuels, generalization of TUBRNP to include burnup-dependent microscopic cross section is

possible. SERPENT results are considered as high-fidelity reference to compare both SCIANTIX and TUBRNP. Given this, we use as validation metric

$$v = \sqrt{\frac{1}{N}\sum_{i=1}^{N}\left(\frac{C_i - R_i}{R_i}\right)^2} \tag{17}$$

Where, C_i is the calculated value (either SCIANTIX or TUBRNP), R_i is the reference value, and N is the number of burn-up steps and the summation is intended over each burn-up step.

For each case (MOX/SFR and MOX/LBE-FR), Figs. 7-27 collect the helium and actinides concentrations as a function of burn-up. From the observation of the nuclide profiles, it emerges that the depletion model implemented in SCIANTIX demonstrates a satisfactory agreement with the reference model for every nuclide, especially at low/average burn-up (< 50 GWd/t_{HM}). U_{237}, Pu_{243} and Am_{244} are not shown because of their very low concentration in fuel matrix at the end of irradiation (< 10^{21} at m^{-3}). Looking at the validation metric reported in Table 5, the general predictive capability of the new depletion model is in line with the results of TUBRNP in each test case. We should note that the TUBRNP module has been validated for few FBR applications against experimental data up to 100 GWd/t_{HM} and is dedicated to the evaluation of relative radial power and burn-up profiles in fuel performance codes. TUBRNP thus focuses on the local concentrations of the most relevant nuclides, while the new depletion model tracks the evolution of a larger number of nuclides. Moreover, the new model shows a good prediction capability for nuclides that present a non-zero concentration at the beginning of irradiation (i.e., U_{238} and plutonium nuclides). Heavy nuclides, like americium and curium, present a higher v, because they are created by successive neutron capture reactions, whose cross-sections are affected by the propagation of the error of the cross-sections and the concentrations of the respective precursors.

Lastly, since helium is produced by α-decays of several nuclides, it is expected that the error in the evaluation of the α-emitters propagates in the helium concentration. Nevertheless, Fig. 7 shows a satisfactory agreement between the new depletion model and SERPENT, with a value of the validation metric v that is comparable to TUBRNP for each fuel/reactor combination, proving that a set of burn-up and Pu/HM enrichment dependent cross-sections is very effective in the description of the fuel evolution as burn-up increases.

Table 4: SCIANTIX input parameters for two verification cases.

Parameter	MOX/SFR	MOX/LBE-FR
Irradiation time (h)	106'000	106'000
Burn-up at discharge (GWd/t_{HM})	200	200
Fission rate (fiss m^{-3} s^{-1})	$1.32 \cdot 10^{19}$	$1.32 \cdot 10^{19}$
Grain radius (m)	$10 \cdot 10^{-6}$	$10 \cdot 10^{-6}$
Fuel density (g cm^{-3})	10.97	10.97
O/M	1.97	1.97
U_{235} (wt.%)	0.6	0.6
U_{238} (wt.%)	79.4	79.4
Pu_{238} (wt.%)	0.5	0.5
Pu_{239} (wt.%)	11.3	11.3
Pu_{240} (wt.%)	5.4	5.4
Pu_{241} (wt.%)	1.2	1.2
Pu_{242} (wt.%)	1.6	1.6

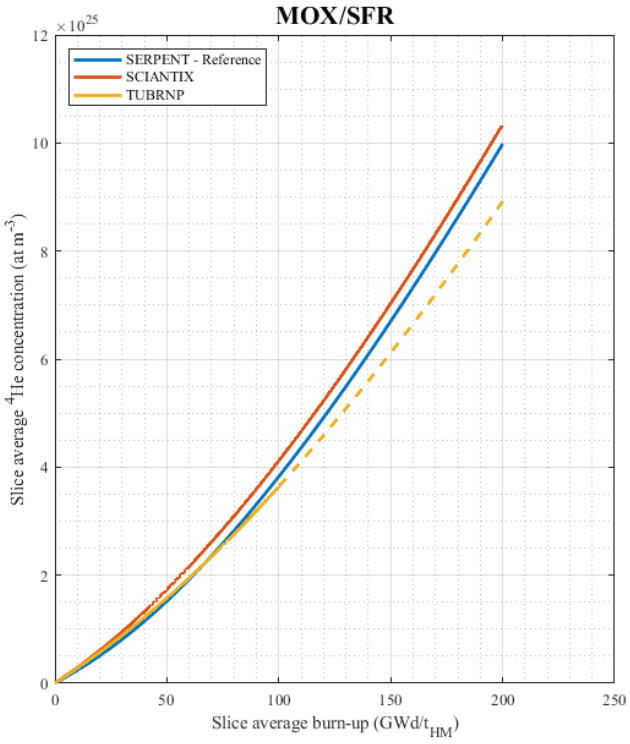

(a)

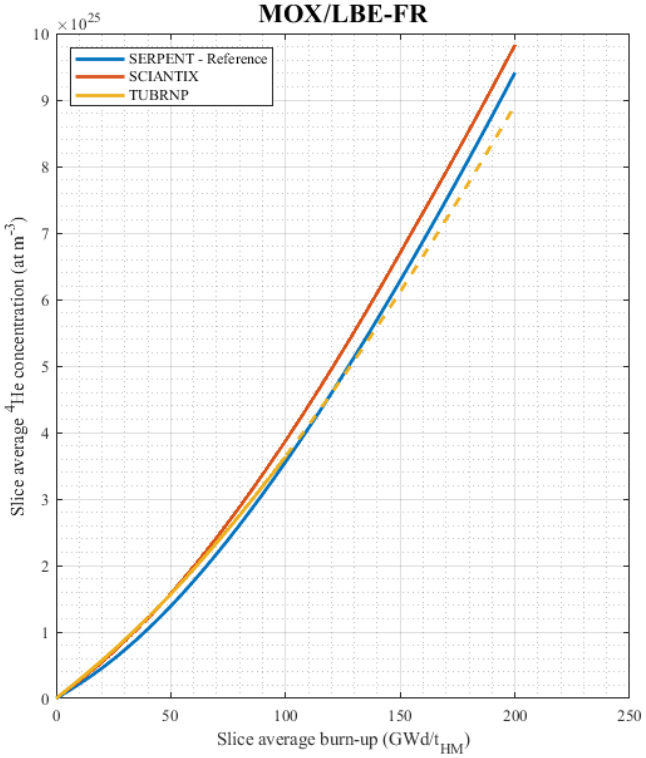

(b)

Figure 7: Evolution of the concentration (at m^{-3}) of He_4 in (a) MOX/SFR case, (b) MOX/LBE-FR case. The result of TUBRNP is dashed above 100 GWd/tHM, i.e., outside its validation range.

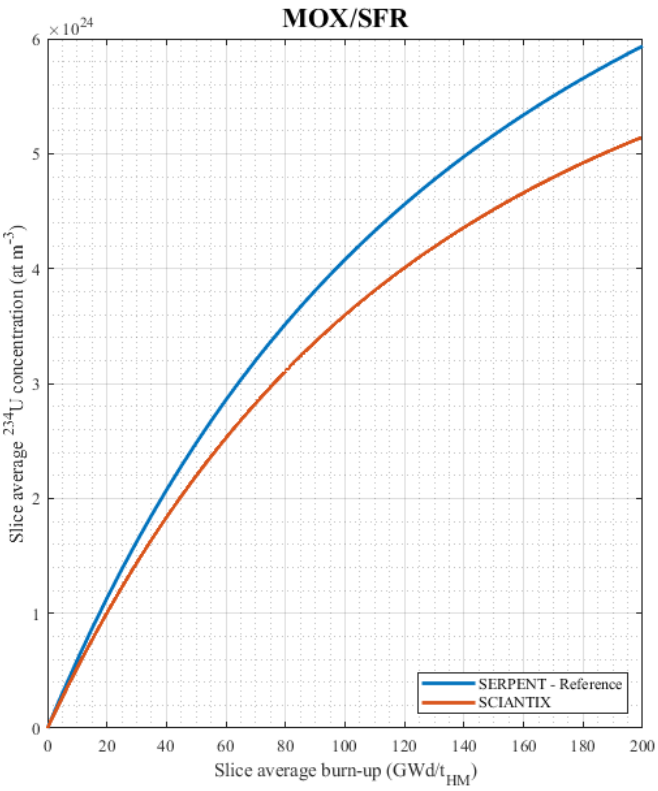

(a)

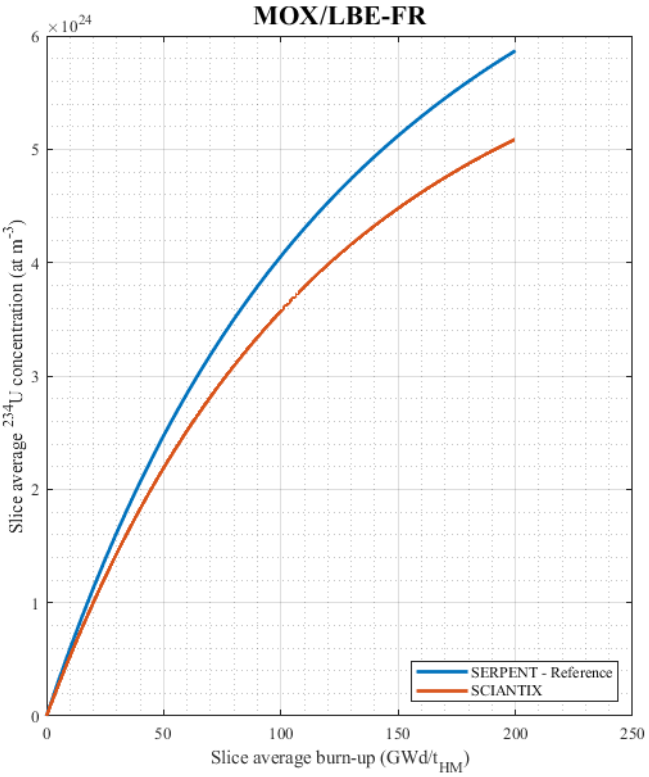

(b)

Figure 8: Evolution of the concentration (at m^{-3}) of U_{234} in (a) MOX/SFR case, (b) MOX/LBE-FR case.

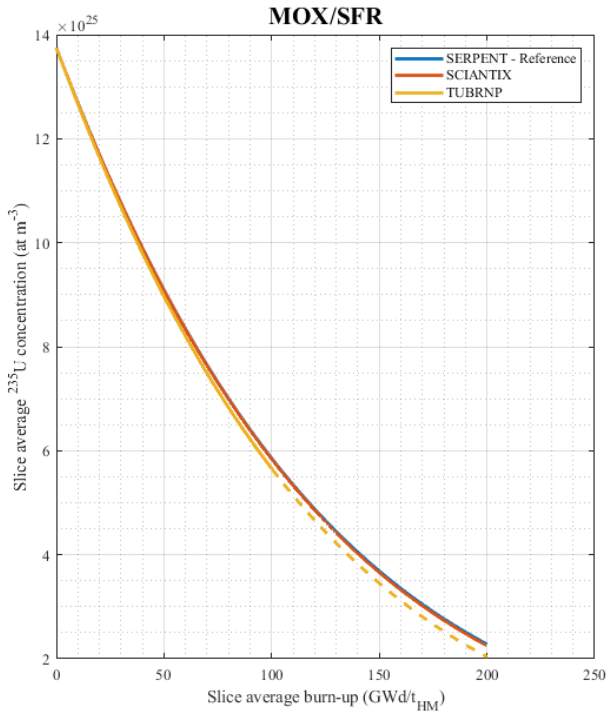

(a)

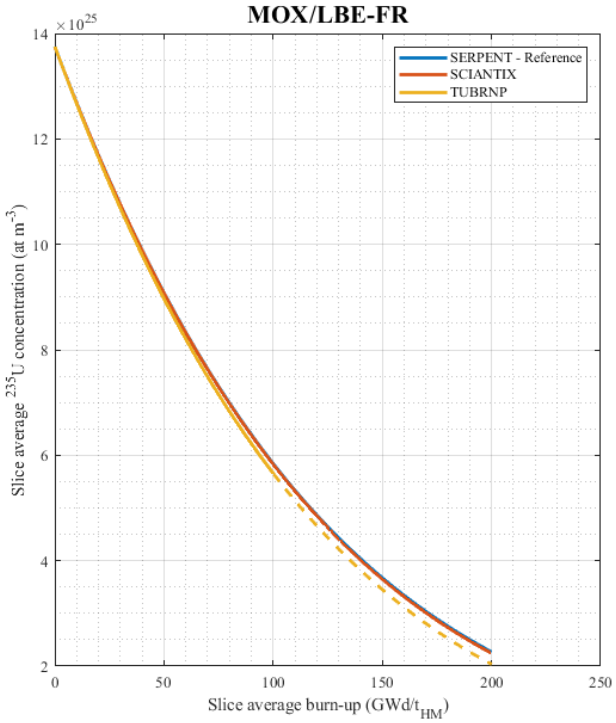

(b)

Figure 9: Evolution of the concentration (at m^{-3}) of U_{235} in (a) MOX/SFR case, (b) MOX/LBE-FR case. The result of TUBRNP is dashed above 100 GWd/tHM, i.e., outside its validation range.

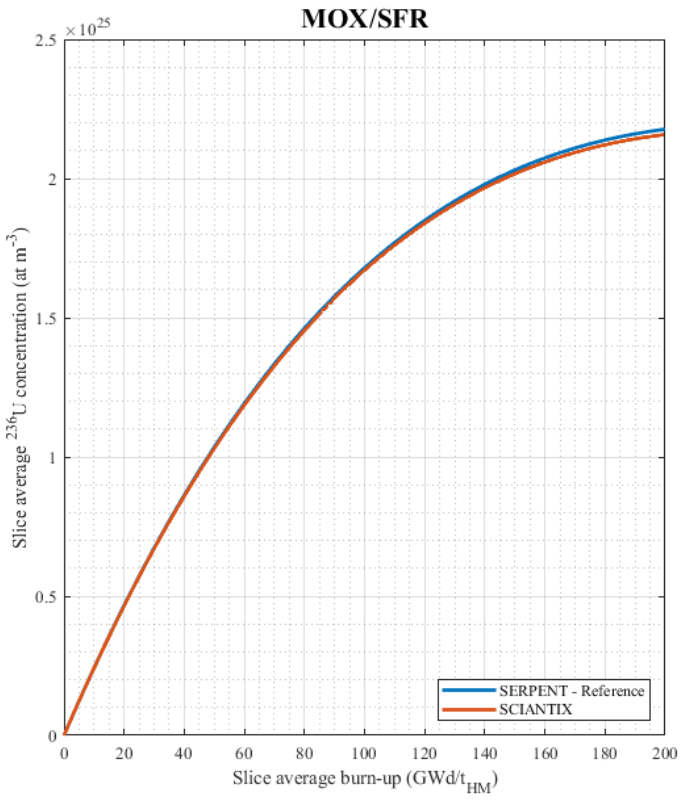

(a)

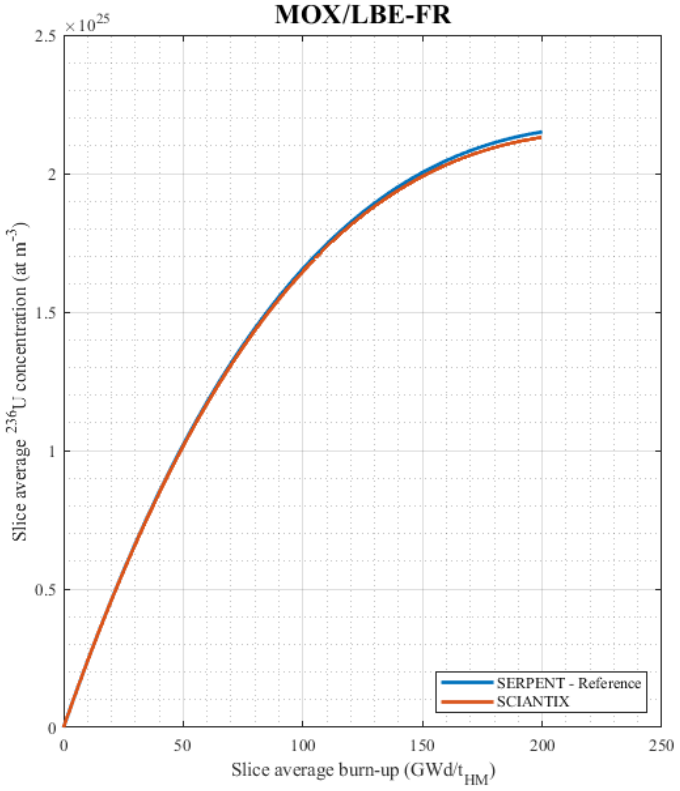

(b)

Figure 10: Evolution of the concentration (at m^{-3}) of U_{236} in (a) MOX/SFR case, (b) MOX/LBE-FR case.

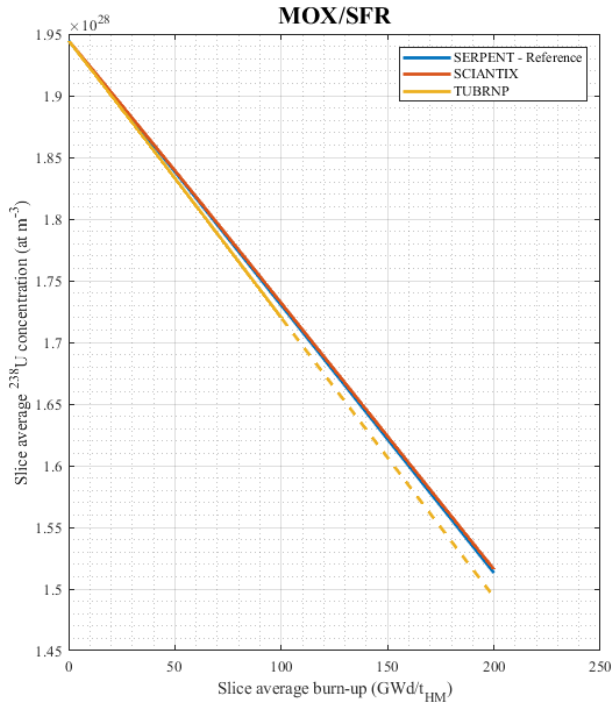

(a)

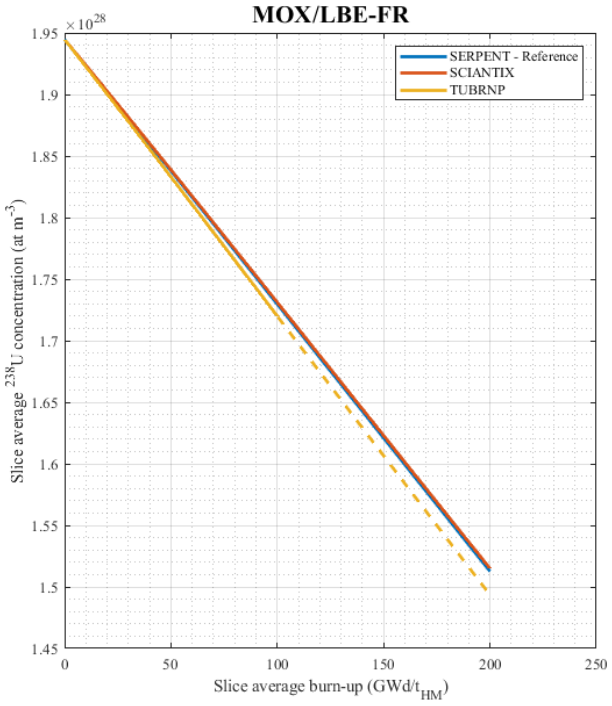

(b)

Figure 11: Evolution of the concentration (at m^{-3}) of U_{238} in (a) MOX/SFR case, (b) MOX/LBE-FR case. The result of TUBRNP is dashed above 100 GWd/tHM, i.e., outside its validation range.

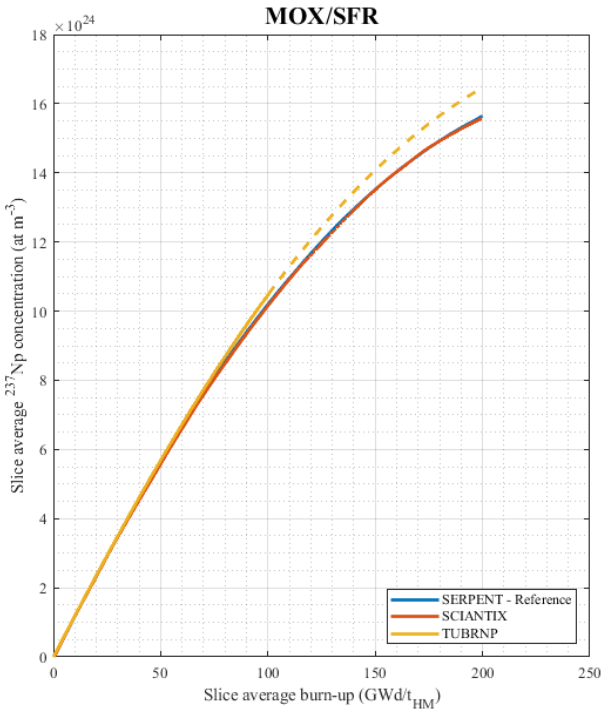

(a)

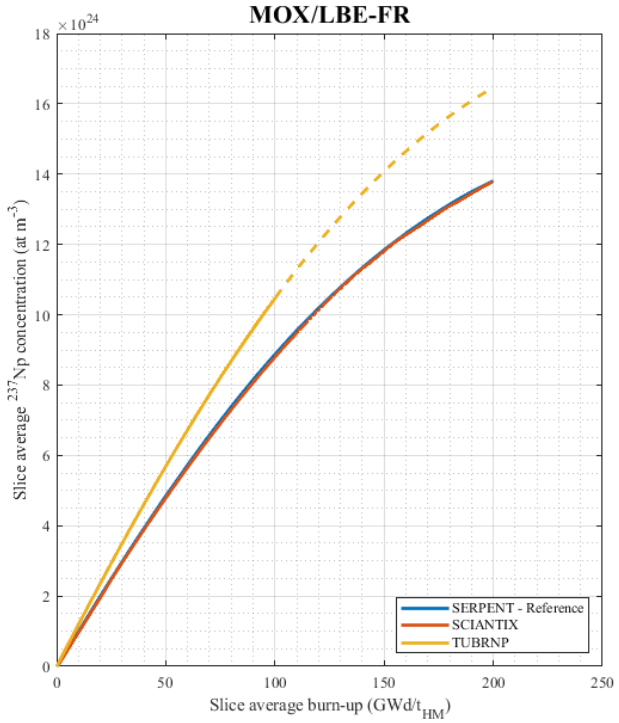

(b)

Figure 12: Evolution of the concentration (at m^{-3}) of Np_{237} in (a) MOX/SFR case, (b) MOX/LBE-FR case. The result of TUBRNP is dashed above 100 GWd/tHM, i.e., outside its validation range.

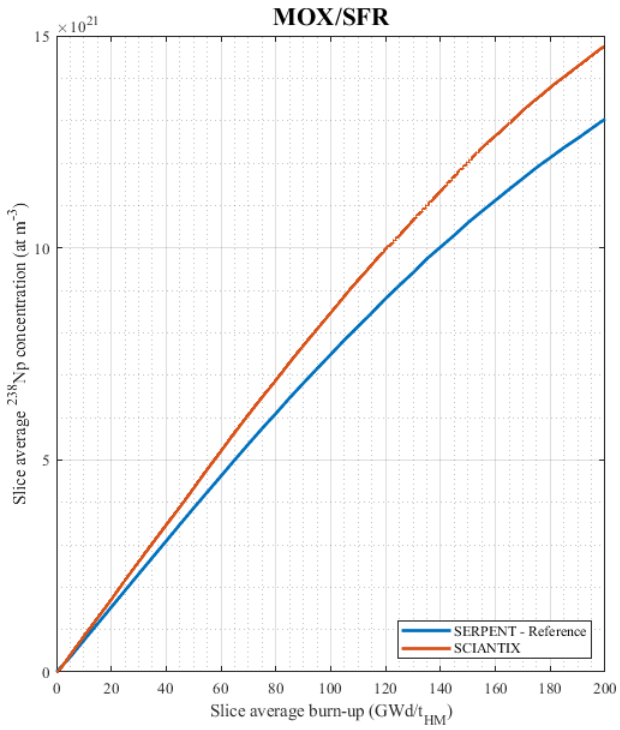

(a)

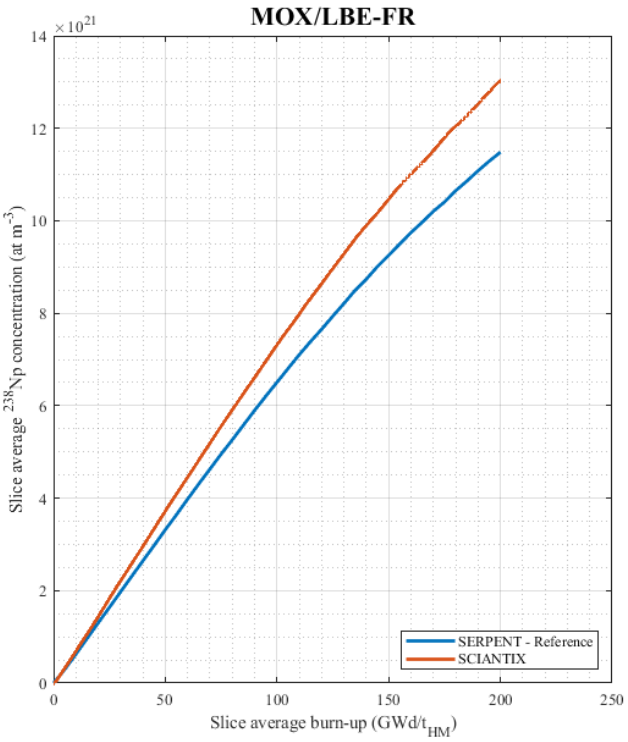

(b)

Figure 13: Evolution of the concentration (at m^{-3}) of Np_{238} in (a) MOX/SFR case, (b) MOX/LBE-FR case.

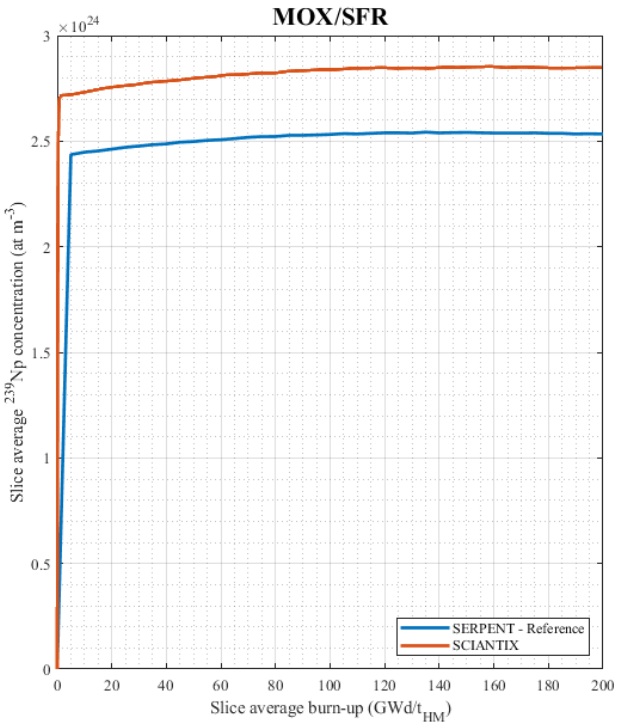

(a)

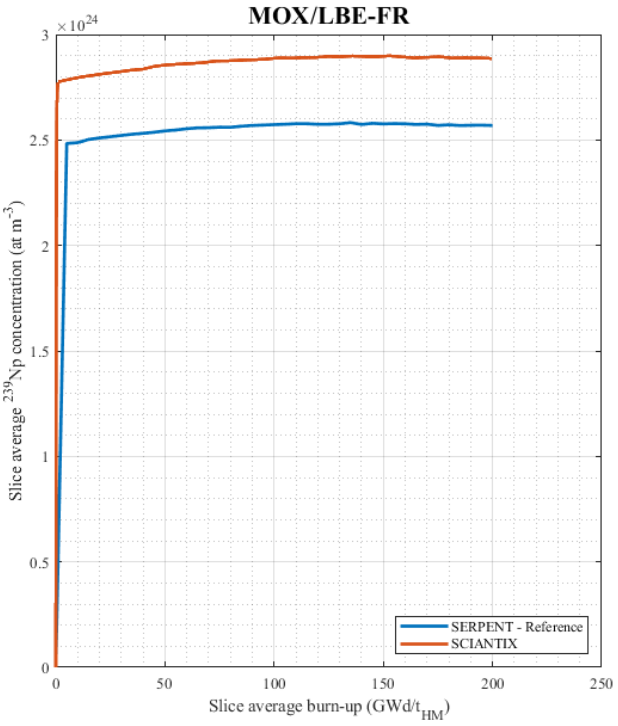

(b)

Figure 14: Evolution of the concentration (at m^{-3}) of Np_{239} in (a) MOX/SFR case, (b) MOX/LBE-FR case.

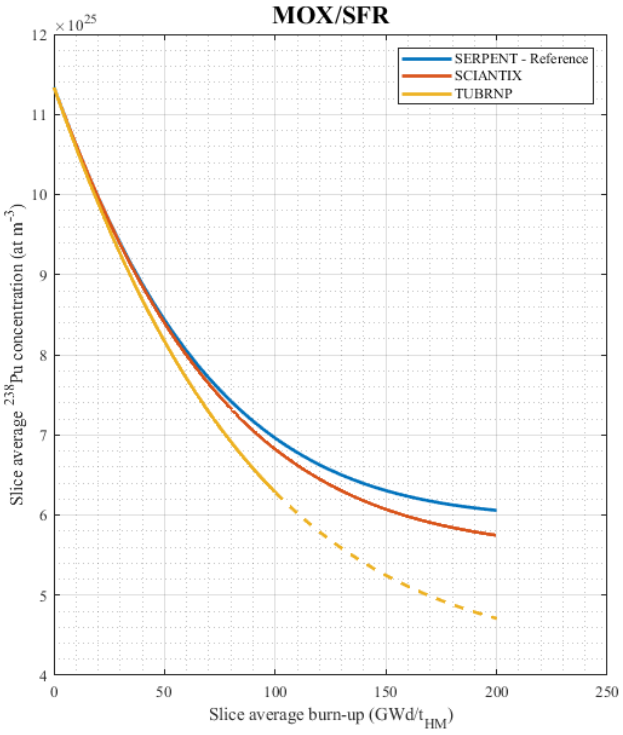

(a)

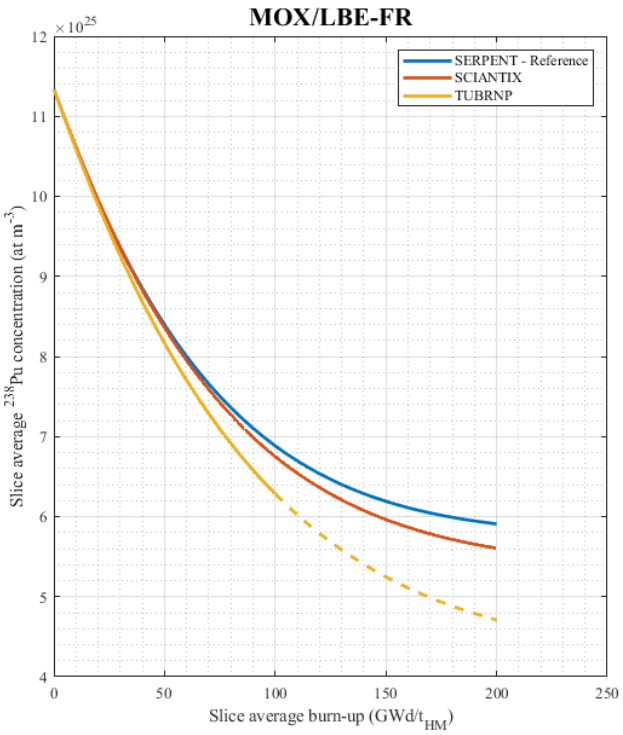

(b)

Figure 15: Evolution of the concentration (at m^{-3}) of Pu_{238} in (a) MOX/SFR case, (b) MOX/LBE-FR case. The result of TUBRNP is dashed above 100 GWd/tHM, i.e., outside its validation range.

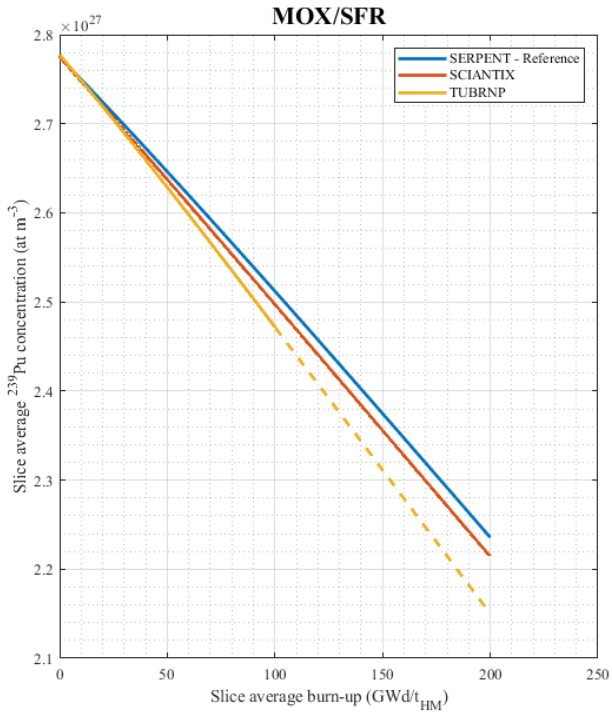

(a)

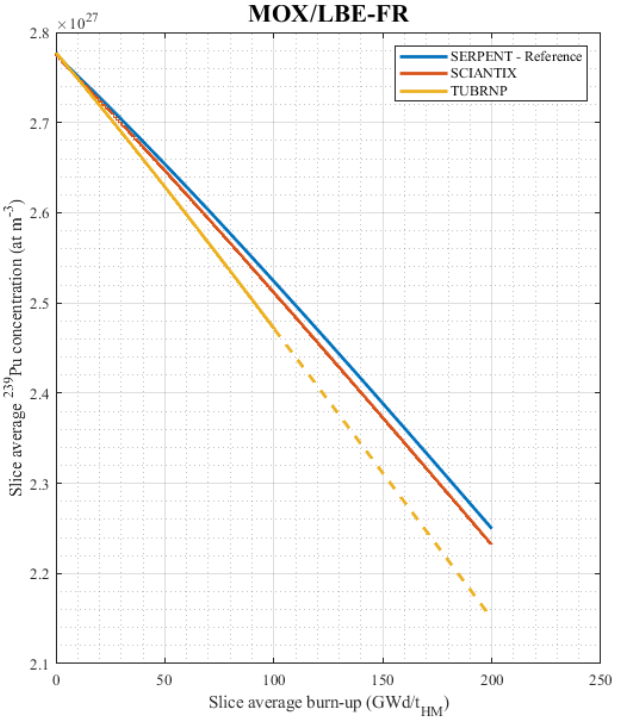

(b)

Figure 16: Evolution of the concentration (at m^{-3}) of Pu_{239} in (a) MOX/SFR case, (b) MOX/LBE-FR case. The result of TUBRNP is dashed above 100 GWd/tHM, i.e., outside its validation range.

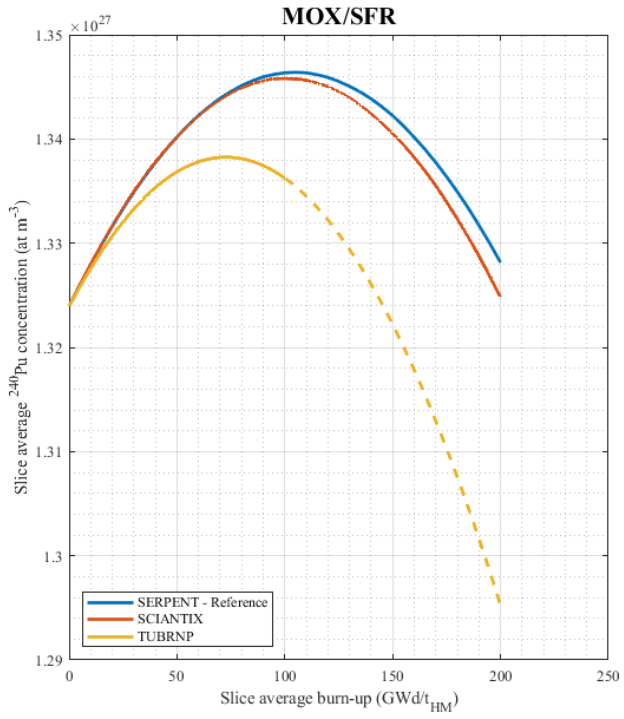

(a)

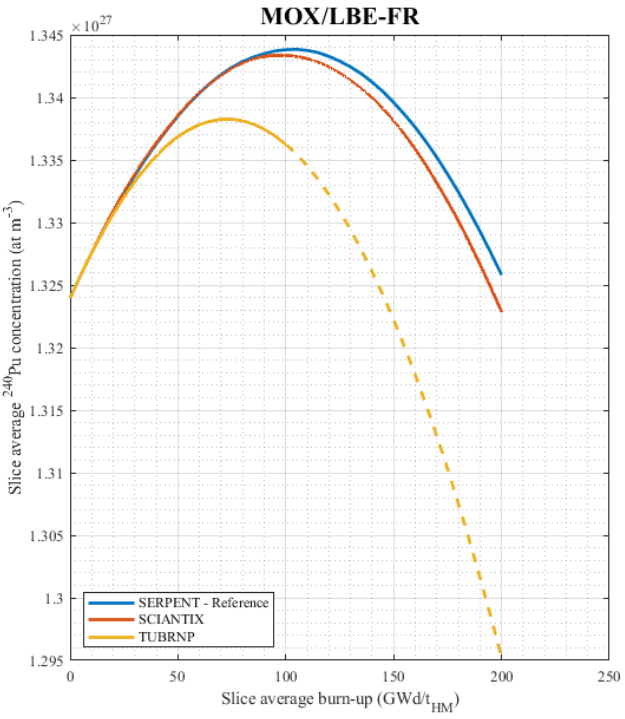

(b)

Figure 17: Evolution of the concentration (at m^{-3}) of Pu_{240} in (a) MOX/SFR case, (b) MOX/LBE-FR case. The result of TUBRNP is dashed above 100 GWd/tHM, i.e., outside its validation range.

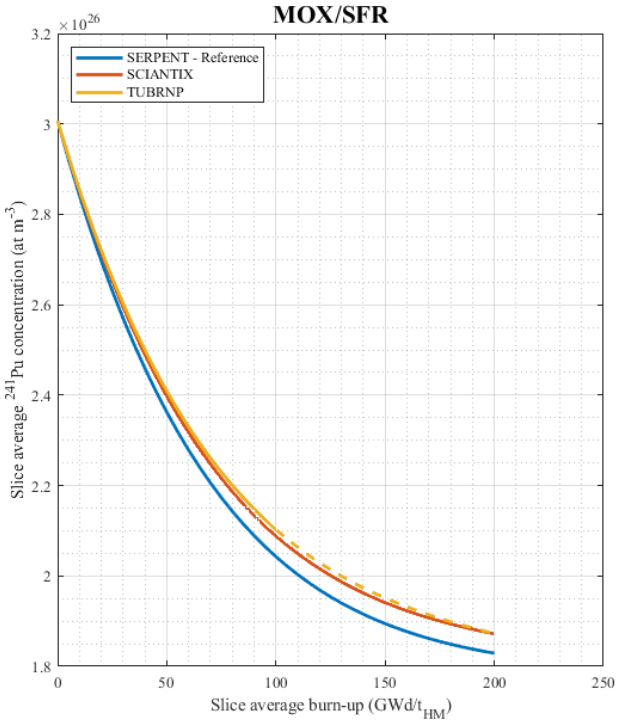

(a)

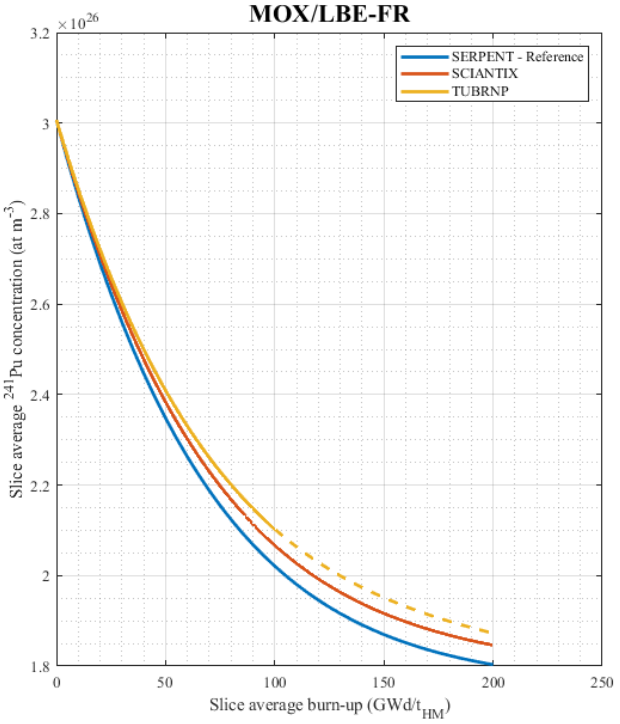

(b)

Figure 18: Evolution of the concentration (at m^{-3}) of Pu_{241} in (a) MOX/SFR case, (b) MOX/LBE-FR case. The result of TUBRNP is dashed above 100 GWd/tHM, i.e., outside its validation range.

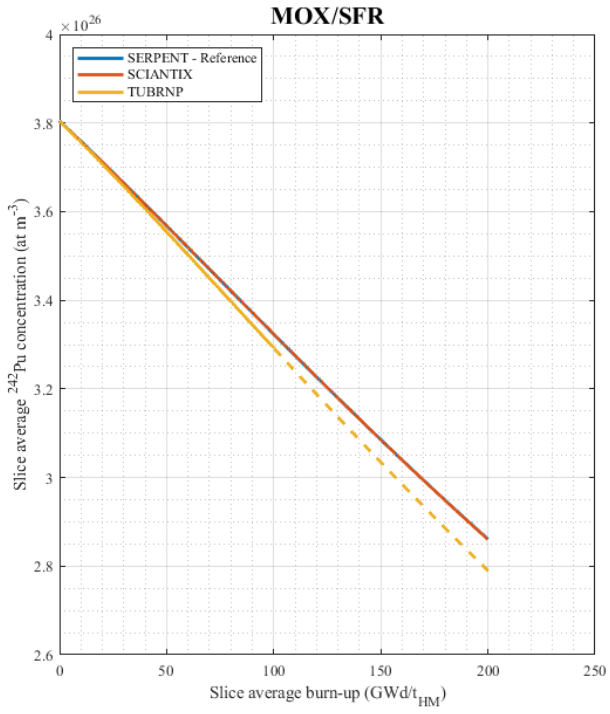

(a)

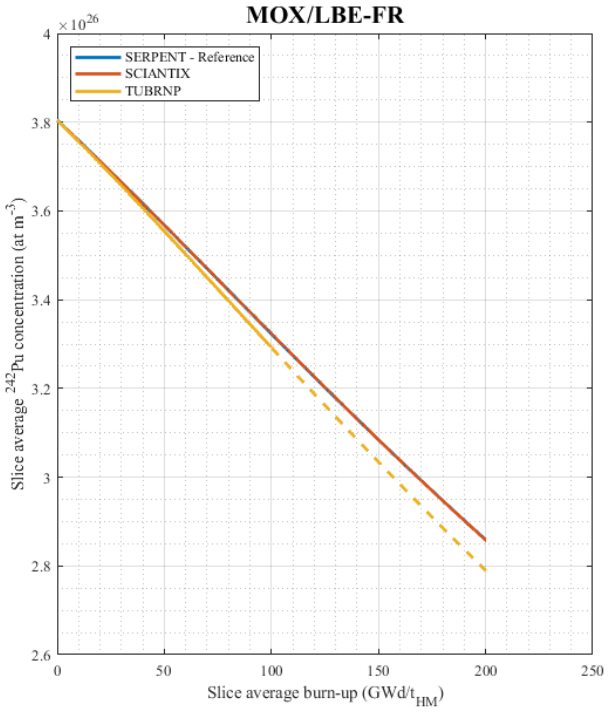

(b)

Figure 19: Evolution of the concentration (at m^{-3}) of Pu_{242} in (a) MOX/SFR case, (b) MOX/LBE-FR case. The result of TUBRNP is dashed above 100 GWd/tHM, i.e., outside its validation range.

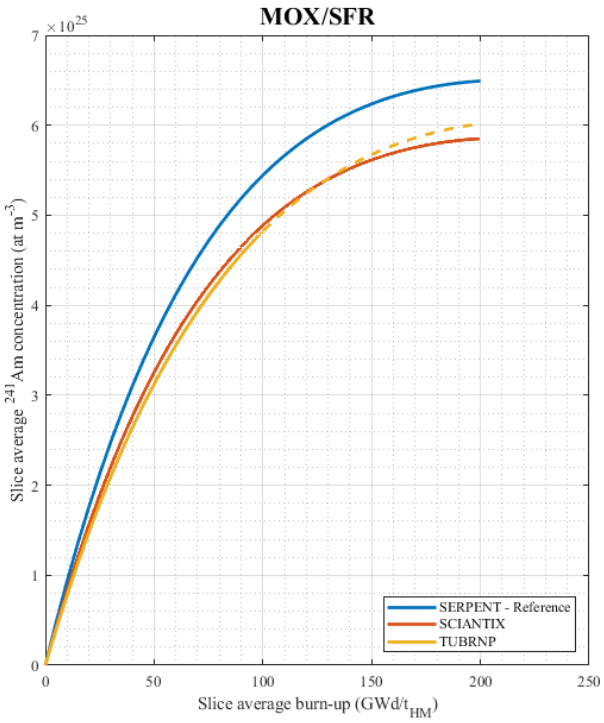

(a)

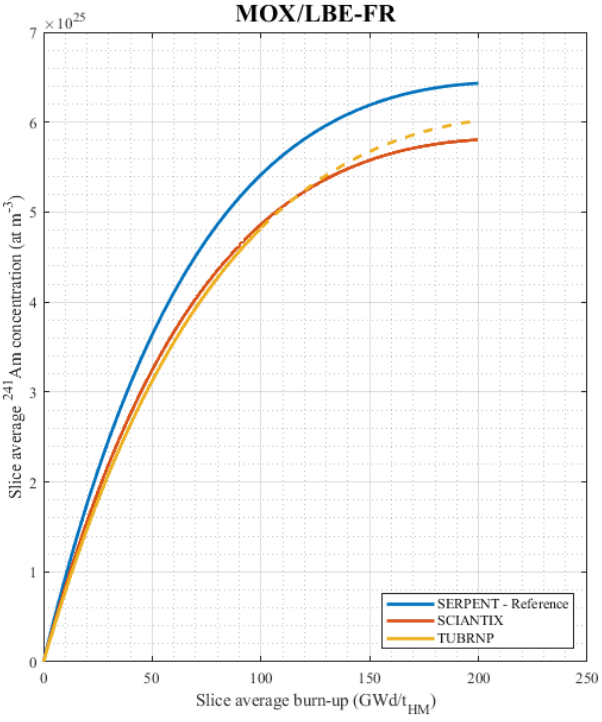

(b)

Figure 20: Evolution of the concentration (at m^{-3}) of Am_{241} in (a) MOX/SFR case, (b) MOX/LBE-FR case. The result of TUBRNP is dashed above 100 GWd/tHM, i.e., outside its validation range.

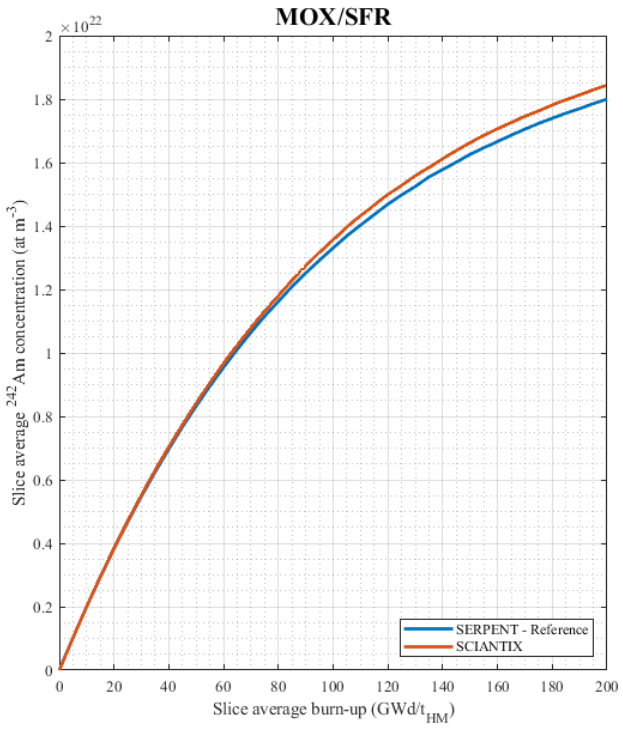

(a)

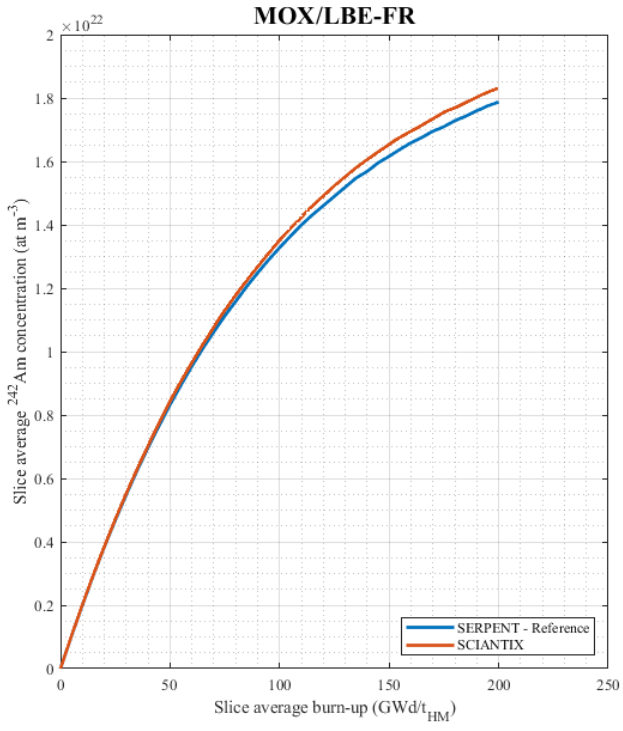

(b)

Figure 21: Evolution of the concentration (at m^{-3}) of Am_{242} in (a) MOX/SFR case, (b) MOX/LBE-FR case.

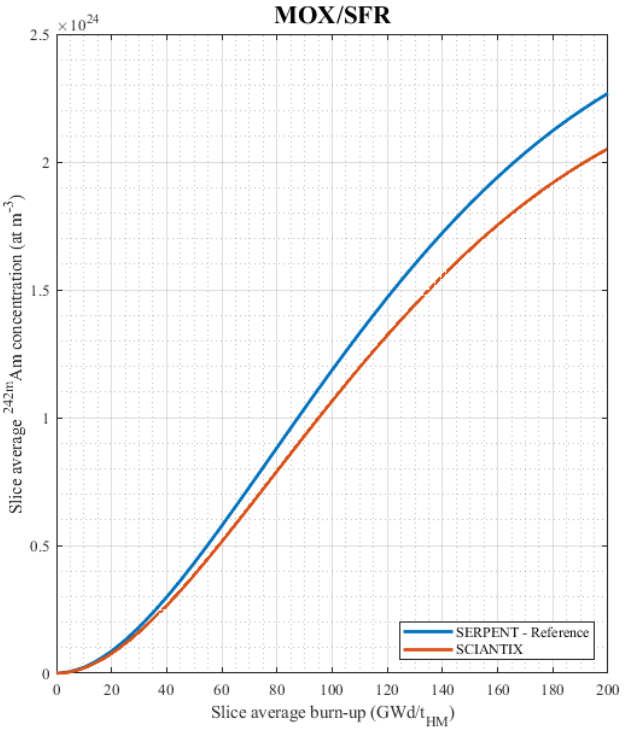

(a)

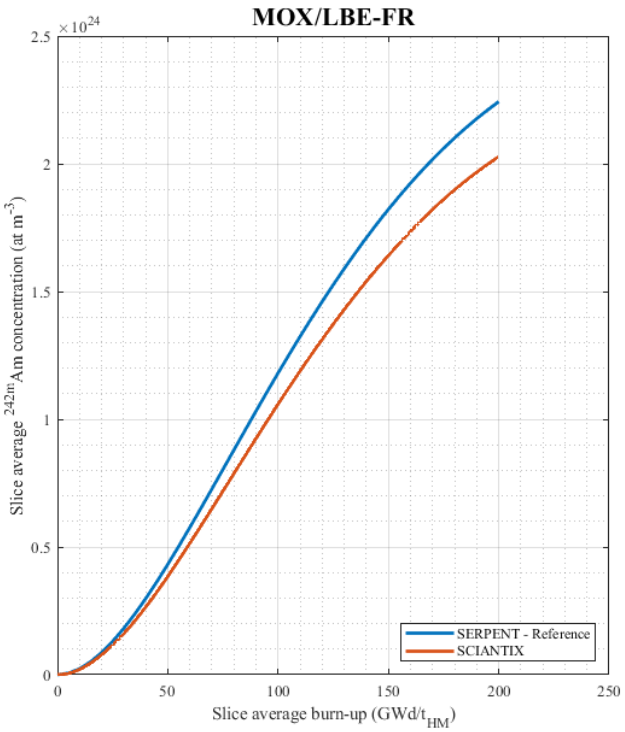

(b)

Figure 22: Evolution of the concentration (at m^{-3}) of Am_{242m} in (a) MOX/SFR case, (b) MOX/LBE-FR case.

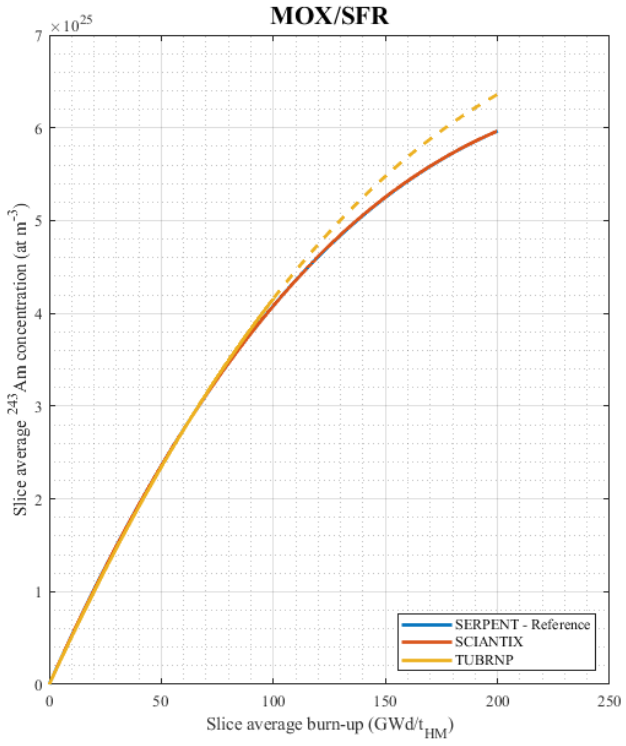

(a)

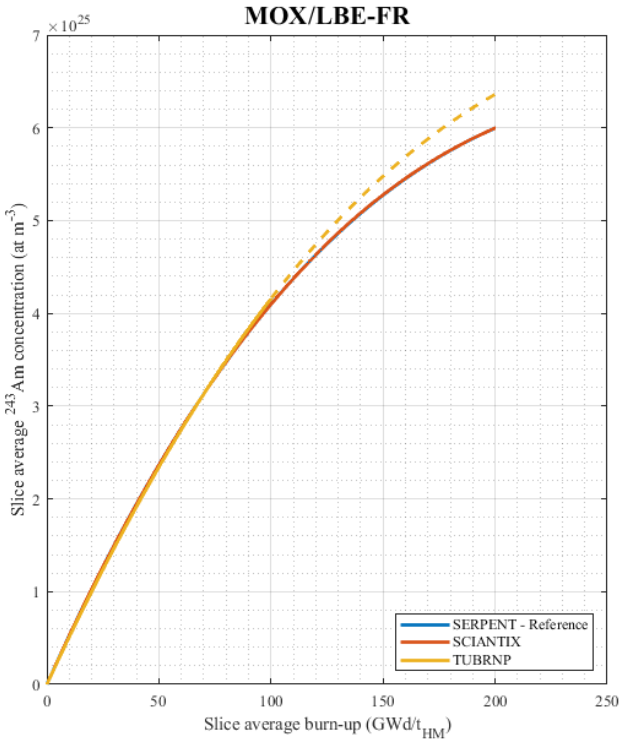

(b)

Figure 23: Evolution of the concentration (at m^{-3}) of Am_{243} in (a) MOX/SFR case, (b) MOX/LBE-FR case. The result of TUBRNP is dashed above 100 GWd/tHM, i.e., outside its validation range.

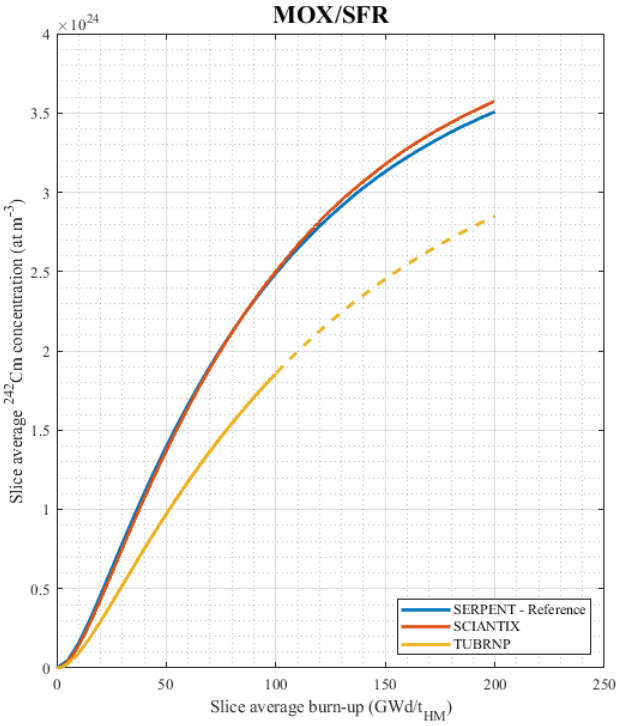

(a)

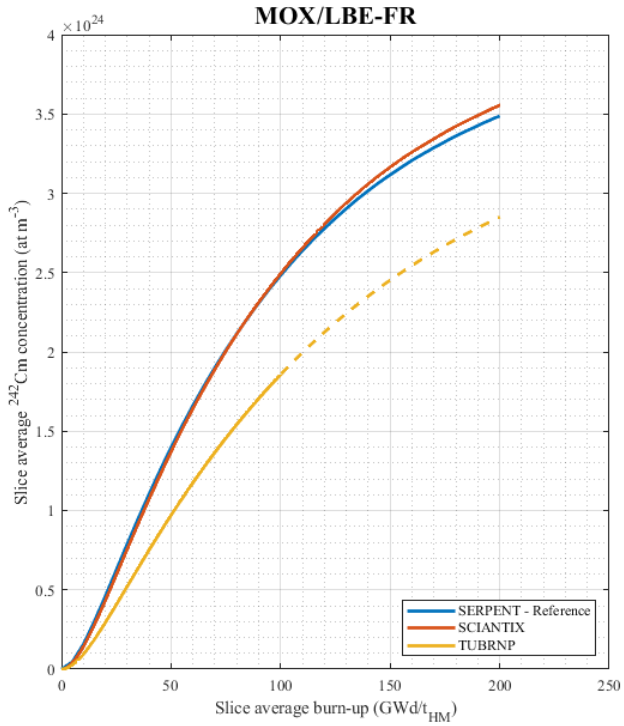

(b)

Figure 24: Evolution of the concentration (at m^{-3}) of Cm_{242} in (a) MOX/SFR case, (b) MOX/LBE-FR case. The result of TUBRNP is dashed above 100 GWd/tHM, i.e., outside its validation range.

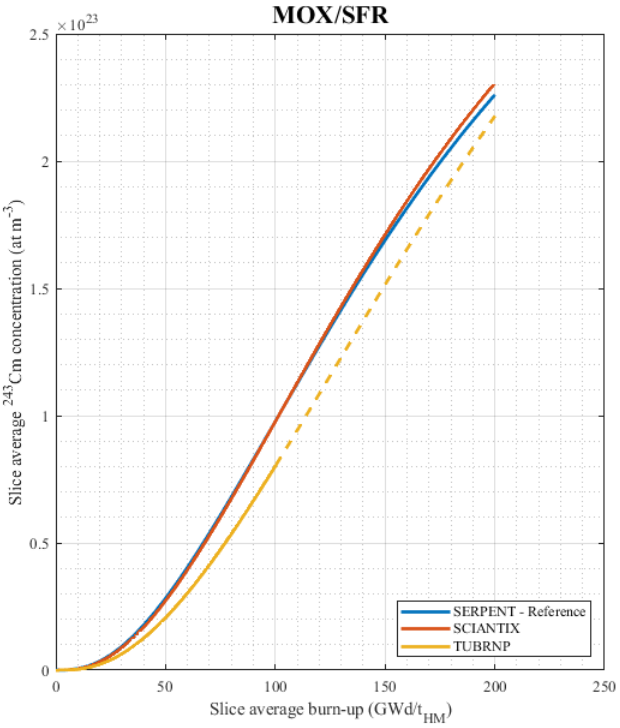

(a)

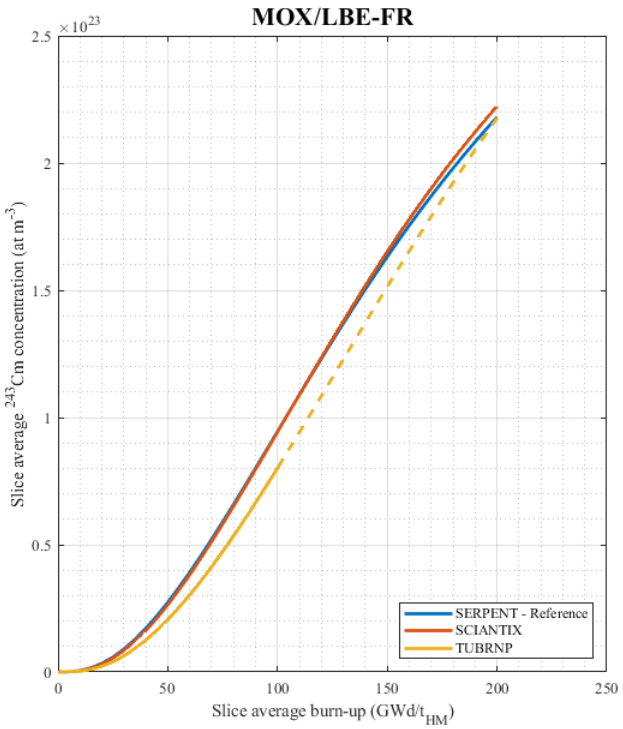

(b)

Figure 25: Evolution of the concentration (at m^{-3}) of Cm_{243} in (a) MOX/SFR case, (b) MOX/LBE-FR case. The result of TUBRNP is dashed above 100 GWd/tHM, i.e., outside its validation range.

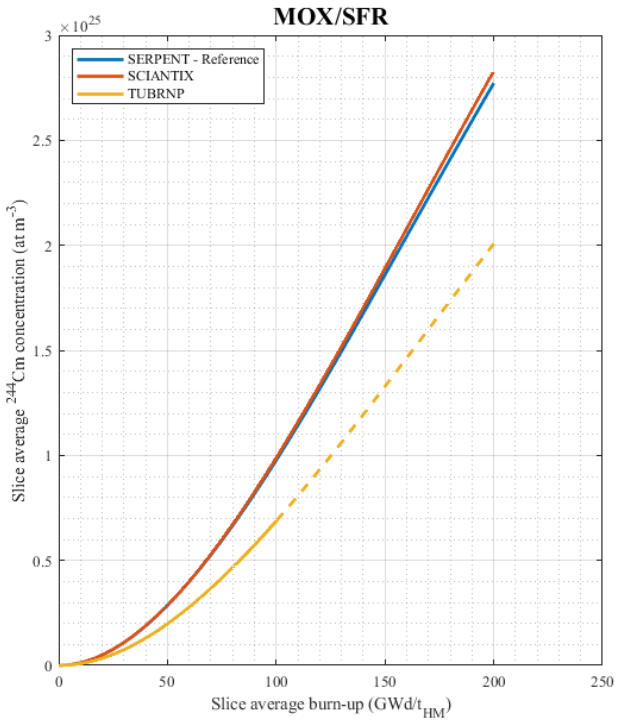

(a)

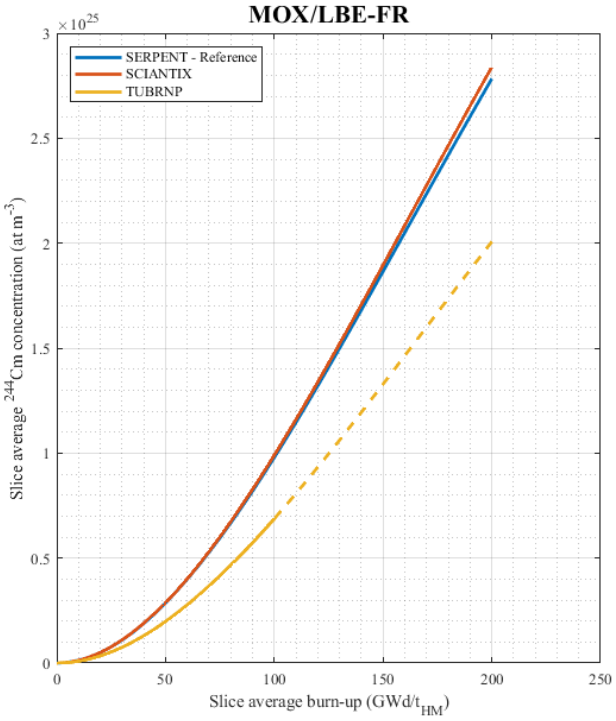

(b)

Figure 26: Evolution of the concentration (at m^{-3}) of Cm_{244} in (a) MOX/SFR case, (b) MOX/LBE-FR case. The result of TUBRNP is dashed above 100 GWd/tHM, i.e., outside its validation range.

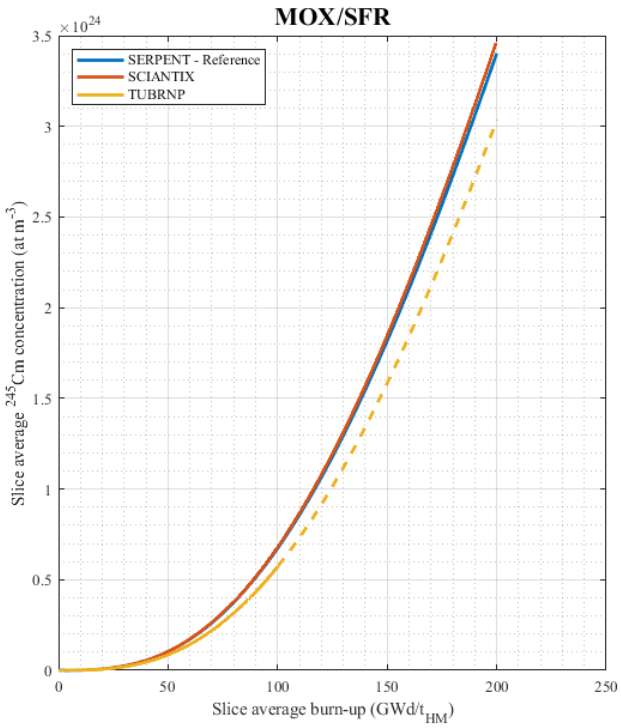

(a)

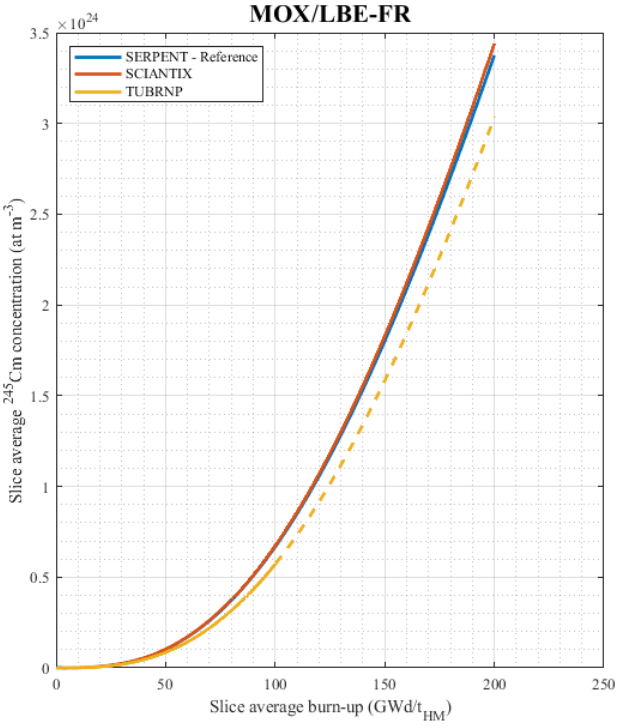

(b)

Figure 27: Evolution of the concentration (at m^{-3}) of Cm_{245} in (a) MOX/SFR case, (b) MOX/LBE-FR case. The result of TUBRNP is dashed above 100 GWd/tHM, i.e., outside its validation range.

Table 5: Validation metric *v* for the comparison of the new depletion model and the high-fidelity reference. The validation metric is reported also for the results from TUBRNP for the sake of comparison. It should be noted that the evaluation of the validation metric for TUBRNP is on the range 0-200 GWd/t_{HM}, with the model being validated only up to 100 GWd/t_{HM}. Lower values of the validation metric correspond to a better agreement.

Validation metric, *v* (/)	MOX/SFR		MOX/LBE-FR	
	SCIANTIX	TUBRNP	SCIANTIX	TUBRNP
He_4	0.1242	0.0838	0.1321	0.1235
U_{234}	0.1373	-	0.1372	-
U_{235}	0.0063	0.0518	0.0056	0.0495
U_{236}	0.0068	0.0808	0.0070	0.0706
U_{237}	0.1601	-	0.1619	-
U_{238}	0.0012	0.0073	0.0010	0.0071
Np_{237}	0.0052	0.0344	0.0111	0.1866
Np_{238}	0.1491	-	0.1417	-
Np_{239}	0.1372	-	0.1392	-
Pu_{238}	0.0317	0.1253	0.0315	0.1137
Pu_{239}	0.0072	0.0207	0.0061	0.0251
Pu_{240}	0.0012	0.0119	0.0011	0.0105
Pu_{241}	0.0230	0.0245	0.0234	0.0351
Pu_{242}	0.0002	0.0130	0.0002	0.0127
Pu_{243}	0.1516	-	0.1513	-
Am_{241}	0.1183	0.1169	0.1177	0.1130
Am_{242}	0.0206	-	0.0204	-
Am_{242m}	0.1158	-	0.1169	-
Am_{243}	0.0004	0.0337	0.0008	0.0306
Am_{244}	0.2470	-	0.2489	-
Cm_{242}	0.0339	0.2642	0.0336	0.2631
Cm_{243}	0.0385	0.2064	0.0373	0.1859
Cm_{244}	0.0155	0.2901	0.0152	0.2918
Cm_{245}	0.0153	0.1476	0.0150	0.1412

Table 6: Comparison between the execution time of TUBRNP and of the SCIANTIX depletion model.

Execution time (s)	TUBRNP	SCIANTIX
MOX/SFR	0.80	0.65
MOX/LBE-FR	0.61	0.66

2 DIFFUSION IN COLUMNAR GRAINS

Because of the high temperature and temperature gradient, three microstructures are created the fuel pellet in MOX operated in fast reactor conditions: from the rim of the pellet towards its centre:

(1) an external as-fabricated zone with unchanged density (T < 1600°C),

(2) an intermediate zone with equiaxed grains with higher density, grain-size of around 20 µm (1600°C < T < 1800°C) and

(3) an internal zone (T > 1800°C) with columnar grains (almost theoretical density, length of approximately 1 mm and radius of 10-20 µm).

In this section, we address the question of the diffusion of fission gases in columnar grains, which is currently considered in fuel performance codes using very strong simplifying hypotheses.

2.1 Model description

The classical description of inert gas behaviour diffusion adopted in fuel performance codes relies on the model by Booth [52]:

$$\frac{\partial}{\partial \mathrm{t}} c_t = \mathrm{S} + \mathrm{D}_{\mathrm{eff}} \frac{1}{r^2} \frac{\partial}{\partial r} r^2 \frac{\partial}{\partial r} c_t \qquad (18)$$

Where, c_t (at m^{-3}) is the total intra-granular gas concentration, S (at m^{-3} s^{-1}) is the production term, and $\mathrm{D}_{\mathrm{eff}}$ (m^2 s^{-1}) is the effective gas diffusion coefficient, a single parameter lumping the diffusion towards the grain boundaries, the trapping/re-solution rate of atoms in/from intra-granular bubbles. The diffusion operator is assumed to be the radial component of the Laplacian operator in spherical coordinates since the grain shape is idealized as a sphere. The boundary conditions are of Dirichlet type, assuming grain boundaries as perfect sinks.

The assumption of spherical grains in Eq. 18, hinders a priori the application of this diffusion description to columnar grains. It is common in fuel performance codes, however, to model diffusion in the columnar grain zone as if the grain were spherical, eventually considering a specific spherical radius *representative* of cylindrical geometry. On the one hand, this modelling approach is partially justified by the high fission gas release expected (not to mention the large uncertainty pertaining to the diffusion coefficient), which makes the modelling simplification less impactful. On the other hand, treating columnar grains according to Eq. 18 implies two degrees of simplification which should be taken into consideration

- The dynamics of diffusion are different in a sphere and in a cylinder and cannot be set equal by the selection only of a representative spherical grain radius.
- Given the temperature dependence of the diffusion coefficient and the temperature profile in the columnar zone, the use of a single value of the diffusion coefficient outside of the Laplacian is inaccurate.

To demonstrate the different diffusion dynamics in a sphere and in a cylinder, we can consider the eigenfunctions of the radial component of the Laplacian in spherical and cylindrical coordinates, i.e., cardinal sines and the J_0 Bessel function, respectively. The corresponding eigenvalues are for the sphere

$$\lambda_n^2 = n^2\pi^2 \frac{\mathrm{D_{eff}}}{a^2} \tag{19}$$

And for the cylinder

$$\alpha_n^2 = z_n^2 \frac{\mathrm{D_{eff}}}{R^2} \tag{20}$$

Where, the index n stands for the mode, i.e., the eigenfunction, a (m) is the spherical grain radius and R (m) is the radius of the columnar grain, and z_n are the zeros of the J_0 Bessel function.

By equating the eigenvalues in Eqs. 19 and 20 the relation between R and a depends on n

$$n^2\pi^2 \frac{\mathrm{D_{eff}}}{a^2} = z_n^2 \frac{\mathrm{D_{eff}}}{R^2} \tag{21}$$

$$R^2 = \frac{z_n^2}{n^2\pi^2} a^2 \tag{22}$$

and hence the use of a spherical Laplacian with a *representative* grain radius fails as a surrogate of the dynamics of diffusion in a cylindrical grain.

The diffusion problem may then be written as

$$\frac{\partial}{\partial \mathrm{t}} c_t = \mathrm{S} + \frac{1}{r}\frac{\partial}{\partial r} \mathrm{D_{eff}}\big(T(z)\big) r \frac{\partial}{\partial r} c_t + \frac{\partial}{\partial z} \mathrm{D_{eff}}(T(z)) \frac{\partial}{\partial z} c_t \tag{23}$$

Where, z (m) is the coordinate along the axis of the cylindrical grain (i.e., along the radius of the pellet), r (m) is the radius of the cylindrical grain, and the effective diffusion coefficient is temperature dependent (the boundary condition is of Dirichlet type, assuming grain boundaries as perfect sinks). For this reason, Eq. 23 is highly non-linear and its solution within a fuel performance code is impractical. Even if the conclusion in Eq. 22 is achieved neglecting the diffusion along the columnar grain axis, it should be noted that neglecting the diffusion of gas in this direction is a non-conservative hypothesis. The diffusion coefficient is higher in the inner part of the pellet (higher temperature) and decreases moving outside along the columnar grain axis, hence the gas concentration diffuses (towards the lateral surface of the grain) more in the inner part than in the outer part. This creates a concentration gradient along the z axis of the grain (opposite to the temperature gradient) and consequently a flux of gas moving towards the inner part of the grain. This transport of gas implies a higher release since it is directed towards the part of the columnar grain with higher diffusivity.

In order to avoid these simplifying hypotheses and to introduce a treatment of diffusion in columnar grains suitable for application in fuel performance codes, we propose a reduced order model based on proper orthogonal decomposition and Galerkin projection (ROM-POD-G) [8,53]. The construction of the ROM is obtained in three steps

1. To collect a limited number of high-fidelity solutions, referred to as *snapshots*, of the governing PDE. The snapshots are obtained through the finite volume method (FVM). For the high-fidelity solution we used the in-house developed `GrainThermoDiffusionFOAM` solver, in the open source software OpenFOAM [54], solving the coupled energy and gas diffusion equations.
2. To evaluate the basis on which to project the governing equation, generating a reduced solution of the PDE. The POD approach handles these steps in terms of an optimization problem, minimizing the L^2 difference between the high-fidelity solution and the reduced one.

3. To apply the Galerkin projection on the governing PDE. Together with the approximation of the solution as a finite summation of time coefficients and basis, this step allows deriving an algebraic linear system to be solved for the time coefficients.

These three steps are performed offline using the CFD software OpenFOAM [54], and then only the ROM step is included in the online calculation of the fuel performance code by inclusion of the SCIANTIX module [15].

In the offline phase, the physical problem of gas diffusion through the columnar grains is mathematically described by a system of coupled PDEs, one for the variable temperature and the other one for the gas concentration. These PDEs are

$$\begin{aligned} L^2\frac{\partial}{\partial \mathrm{t}}T - L^2\frac{1}{\rho}\frac{\partial}{\partial\rho}\alpha\big(T(\xi)\big)\rho\frac{\partial}{\partial\rho}T - R^2\frac{\partial}{\partial\xi}\alpha\big(T(\xi)\big)\frac{\partial}{\partial\xi}T = L^2\mathrm{Q} \\ L^2\frac{\partial}{\partial \mathrm{t}}c_t - L^2\frac{1}{\rho}\frac{\partial}{\partial\rho}\mathrm{D_{eff}}\big(T(\xi)\big)\rho\frac{\partial}{\partial\rho}c_t - R^2\frac{\partial}{\partial\xi}\mathrm{D_{eff}}\big(T(\xi)\big)\frac{\partial}{\partial\xi}c_t = L^2\mathrm{S} \end{aligned} \tag{24}$$

Where, t (s) is time, $\rho = r/R$, $\xi = z/L$, T (K) is the temperature, $\mathrm{D_{eff}}$ ($\mathrm{m^2\ s^{-1}}$) is the effective gas diffusion coefficient, α ($\mathrm{m^2\ s^{-1}}$) is the thermal diffusivity, S (at $\mathrm{m^3\ s^{-1}}$) is the production rate of inert gas, and Q ($\mathrm{K\ s^{-1}}$) is the normalized heat generation rate.

2.2 Preliminary results and approach planned

The results obtained with the system of PDEs (Eqs. 24) solved in OpenFOAM are shown below, with representations of temperature T (Fig. 28) and gas concentration c_t (Fig. 29) within the non-dimensional 1x1 cylinder. Table 7 reports the values of the parameters used for this simulation. The temperature Dirichlet boundary condition (BC) is set to 2000 K, and the simulation is set to 10^7 s.

The gas concentration exhibits the longitudinal distribution effect, as mentioned in Section 3.1, with the maximum of the gas concentration in the outer part of the columnar grain (outer with the respect to the fuel pellet radius). The concentration gradient towards the inner part of the columnar grain is responsible for the transfer of gas towards the inner, and hotter, part of the grain. This effect can be only obtained by solving the coupled partial differential equations considering the diffusion both along the grain axis and along the radial direction.

Prior to the development of the envisaged reduced order model and its inclusion in fuel performance codes, we present a roadmap of simulations aimed at evaluating the importance of having a solution for the coupled set of Eqs. 24, or if it is enough in certain conditions to solve a single equation considering only the radial diffusion (i.e., like Eq. 18, but in cylindrical coordinates). The matrix of simulations is reported in Table 8. Since the temperature of the columnar zone is high (above 2000 K), the release of fission is expected to be fast. For this reason, the impact of a rigorous description of the diffusion problem is presumably more relevant at the beginning of irradiation. We hence plan to evaluate the difference between various approximated approaches after one week, one month, and one year of irradiation. The approaches to be compared are as follows

1. The solution of one single gas diffusion problem (only radial component of the Laplacian), at one representative temperature, referred to as SCIANTIX, one point.
2. The solution of a set of decoupled gas diffusion problems (only radial component of the Laplacian) at various temperatures along the grain, referred to as SCIANTIX multi-point.
3. The solution of temperature/concentration coupled problem (including the axial component of the Laplacian), referred to as OpenFOAM.

The figure of merit identified as relevant for fuel performance code applications to be compared between the three mentioned approaches is the spatially averaged gas concentration. This comparison will pave the way to the clarification of the impact of the different approximations and to the identification of the scenarios in which they do not effectively represent the solution, thus requiring the introduction of the reduced order model.

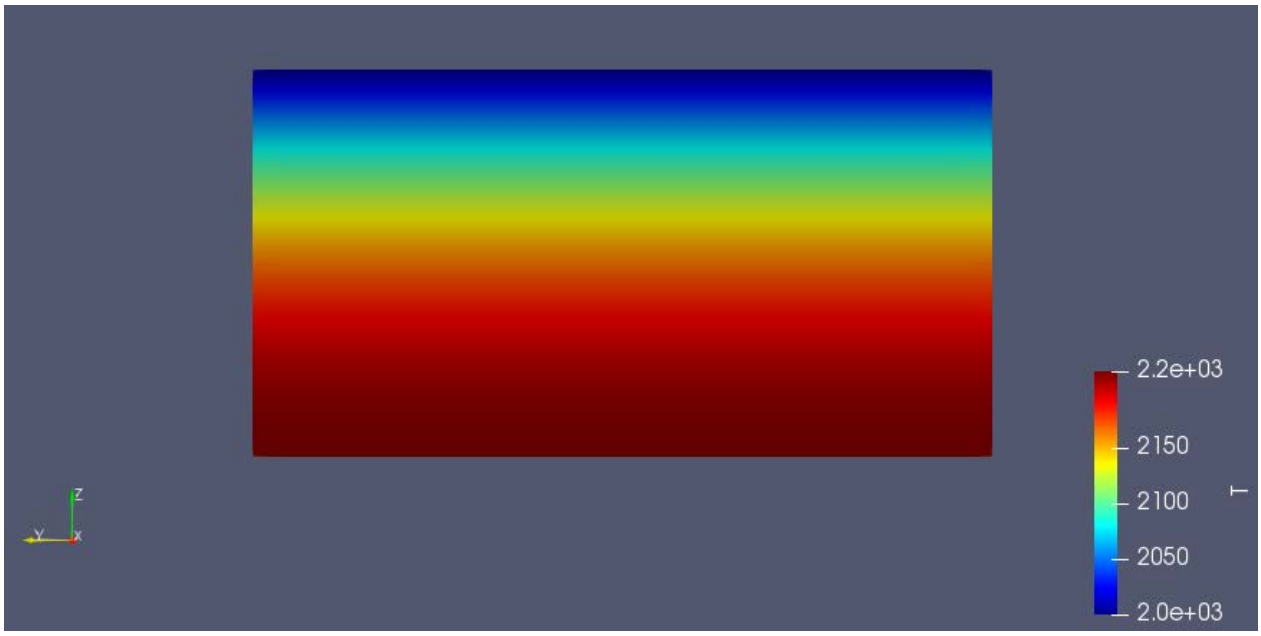

Figure 28: Temperature plot in a non-dimensional columnar grain. The top of the rectangle corresponds to the outer part of the grain, units in Kelvin.

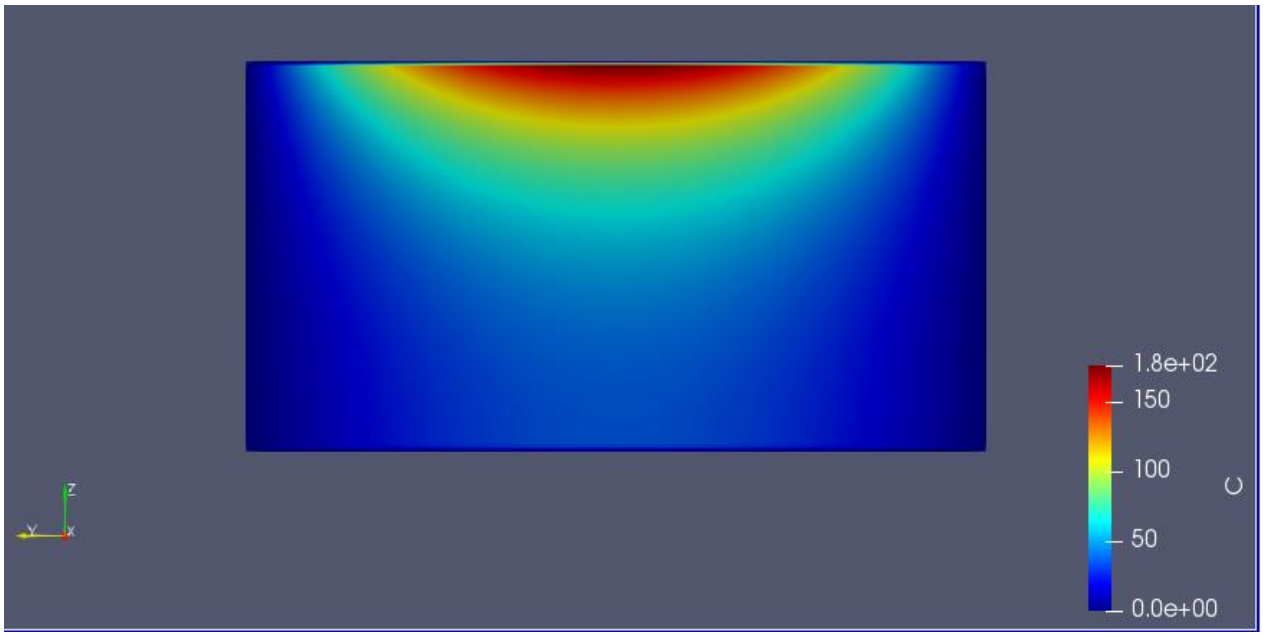

Figure 29: Gas concentration plot in a non-dimensional columnar grain. The top of the rectangle corresponds to the outer part of the grain, units in mol m^{-3}.

Table 7: Parameters used for the high-fidelity simulation of the gas diffusion in columnar grain.

Parameter	u.d.m.	Value
α	$m^2\ s^{-1}$	$5\ 10^{-7}$
D_{eff}	$m^2\ s^{-1}$	Turnbull *et al.* [55]
S	$mol\ m^{-3}\ s^{-1}$	$1.5\ 10^{-4}$
Q	$K\ s^{-1}$	$2.2\ 10^{2}$
L	m	$1\ 10^{-3}$
R	m	$10\ 10^{-6}$
T_{BC}	K	2000
t_{end}	s	10^{7}

Table 8: Simulation matrix to be used as roadmap for the further development of the reduced order model accounting for diffusion in columnar grains.

Duration	SCIANTIX (one point)	SCIANTIX (multi-point)	OpenFOAM
One week	2100 K	2000-2200 K, ΔT = 50 K	$T(z)$
One month	2100 K	2000-2200 K, ΔT = 50 K	$T(z)$
One year	2100 K	2000-2200 K, ΔT = 50 K	$T(z)$

3 GRAIN-BOUNDARY VENTING

High temperature and temperature gradients characteristic of MOX fuel operated in fast reactor conditions induce a behaviour of fission gases different from that observed in light water reactor conditions. The conventional design hypothesis of 100 % of the gas released, however, is not satisfactory to simulate the performance of fuel pins in reactors with a significant part of the fuel column at not-so-high temperatures (e.g., ASTRID, MYRRHA, ALFRED). Direct use of physics-based fission gas behaviour models tailored for application to light water reactor is not usually possible, since the faster kinetics expected in fast reactors imply different and/or additional evolution mechanisms and hence tend to bring several model parameters out of range. For these reasons, we propose a physics-based model describing fission gas behaviour oriented for application in simulation of fast reactor MOX performance. The proposed model differs from current formulations applied in fuel performance codes in the description of grain-face percolation, which is the critical process controlling the onset of thermal release. The percolation threshold proposed, based on random numerical experiments, provides a self-consistent and self-limiting description, which avoids a potential unphysical behaviour caused by fast grain-boundary bubble growth and consequent coalescence. The proposed model is implemented in the SCIANTIX code, targeting use in GERMINAL and TRANSURANUS.

The content of this section will be published in *D. Pizzocri, T. Barani, R. Genoni, L. Luzzi, M. Lainet, P. Van Uffelen, "Modeling of the grain-boundary vented fraction for the description of fission gas behaviour in fast reactor conditions", in preparation.*

3.1 Model description

The main issue identified in the models describing inter-granular gas behaviour mechanistically is the absence of physical bounds to the coalescence process. The description of coalescence of inter-granular bubbles is typically treated using the model developed by White [56], i.e., relating the rate of decrease of the bubble number density to the increase of the bubble projected area on the grain-face based on geometric considerations. When the bubbles on the grain face become large enough and are numerous, the grain face itself is considering percolated. This intuitive definition of percolation is based on the hypothesis, confirmed by phase-field studies (e.g., see the work of Prudil and co-authors [57] and the discussion by Van Uffelen [58]) that grain edges percolate before grain faces, with grain faces hence being the limiting factor in the percolation of the overall fuel pellet.

The treatment of coalescence proposed by White and adopted in several state-of-the-art fission gas behaviour models (e.g., two used in the INSPYRE Project [15,59]) presents limitations when applied for the simulation of fast reactor MOX fuels. In these fuels, since the temperature is high, the kinetics of bubble growth is extremely fast [60] and bubbles tend rapidly towards their equilibrium dimension. As the bubbles grow, the coalescence progresses, and the number of bubbles decreases. If the growth kinetics is too fast, the coalescence is strong, and the number of bubbles decreases with no lower bound imposed by the model. Such a reduction is unphysical, since the model tends asymptotically towards one (huge) bubble.

To overcome this limitation, which hinders the application of these models in fast reactor conditions, we propose to introduce a grain-face vented fraction φ (/). This vented fraction is defined as the fraction of grain-boundary bubbles connected to the grain edge, which is assumed to be always percolated. Given the vented fraction, we assume that a fraction φ of the atoms arriving at the grain boundary is directly vented and that only the rest (1 – φ) contributes to bubble growth and hence to coalescence. This approach is in line with the treatment of open porosity proposed by Claisse and Van Uffelen [61]. It is of interest to combine these two modelling approaches in the future. The treatment of fabrication porosity is expected to impact fission gas release in the outer (cooler) part of the pellet. Ideally, this modelling approach allows for a self-limiting behaviour of the grain-boundary bubble behaviour. The problem is shifted to the calculation of the grain-face percolation fraction.

To evaluate the vented fraction φ, we performed a numerical random experiment generating 1000 square images representative of grain faces. Each grain face is assumed of size 10x10 μm². On each grain face, we generate superposing single-sized circles of radius sampled from an uniform distribution ~[0,1 μm].

Figure 30 shows three examples of random grain faces, with clearly different fractional coverages (area of the bubble over the area of the grain face itself) and different vented fractions (defined by the fraction of bubbles touching the edge of the grain face).

In each grain face, we count the number of effective bubbles N_{eq}, i.e., the separated number of clusters of circles. The equivalent radius of each cluster/bubble is calculated as

$$R_{eq} = \sqrt{A/\pi} \tag{25}$$

where A (μm²) is the area of the cluster/bubble. The fractional coverage F (/) is defined accordingly as

$$F = S_1 = \frac{1}{A_{tot}} \sum_i \pi R_{eq,i}^2 \tag{26}$$

Where, A_{tot} = 100 μm² is the area of the generated grain face. The fractional coverage is identical to S_1, i.e., the porosity on the grain face. In Fig. 31a we report each generated grain face in the space $\{R_{eq}, N_{eq}\}$. The fact that the points end up in a bounded region of the plane is an effect of the coalescence, simulated by the geometrical partial superposition of the randomly generated circles.

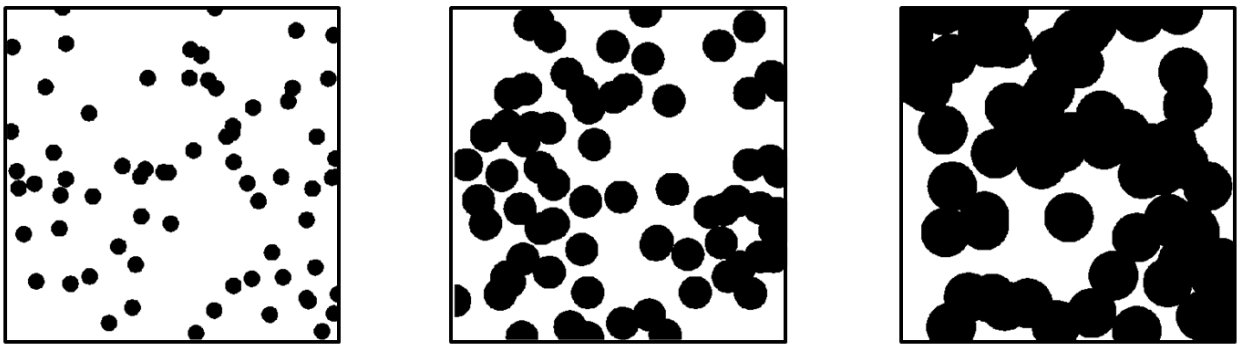

Figure 30: Example of randomly generated grain faces with progressively increasing fractional coverage and vented fraction.

In each generated grain face, we evaluated the fraction of pores touching the edge, i.e., the vented fraction φ. The results are plotted in Fig. 32a as a function of the fractional coverage. The best-estimate fit of a generalized sigmoidal function gives the estimation of the vented fraction as follows

$$\varphi = \frac{1}{[1 + \omega e^{-\kappa(F - F_{sat})}]^{1/\omega}} \tag{27}$$

with the parameters ω = 4, κ = 20, F_{sat} = 0.5. The function reported in Eq. 27 has several interesting features

- The inflection point is at F = 0.5, which corresponds to the saturation fractional coverage observed experimentally by White and co-workers [62] and adopted in various models [56,59].
- At the value of $F = \pi/4$, which corresponds to the theoretical value at which circles arranged in a regular array percolate [63], we have φ = 0.99. It should be noted that the definition of venting (point on a grain-face connected to an edge) used in this work differs from the classical definition of percolation (edge connected to the opposite edge). Nevertheless, the two definitions tend to predict similar values of percolated/vented fraction as the fractional coverage increases.
- The variance of the percolated fraction decreases as the fractional coverage increases, consistently with the coalescence that decreases the effective number of bubbles as the fractional coverage increases.

The purely geometric numerical experiment performed in this work can be compared with the physical phase field approach followed by Millett and co-workers [64] (Fig. 32b). The two approaches provide qualitatively identical results, with the vented fraction presenting a clear sigmoidal shape with the inflection point around F = 0.5. Quantitatively, the present results show a higher vented fraction compared to those reported in [64]. This trend, explained with the proposed geometrical approach, does not account for the relaxation of bubbles and for ripening, resulting in smaller fractional coverage. Nevertheless, the overall agreement between these two results obtained using completely different approaches is remarkable, corroborating the use of Eq. 27 as a description of the percolation of grain faces. For the sake of comparison, a best estimate fit of the results obtained by Millett and co-workers is obtained with the identical sigmoidal function used in this work, with F_{sat} = 0.6.

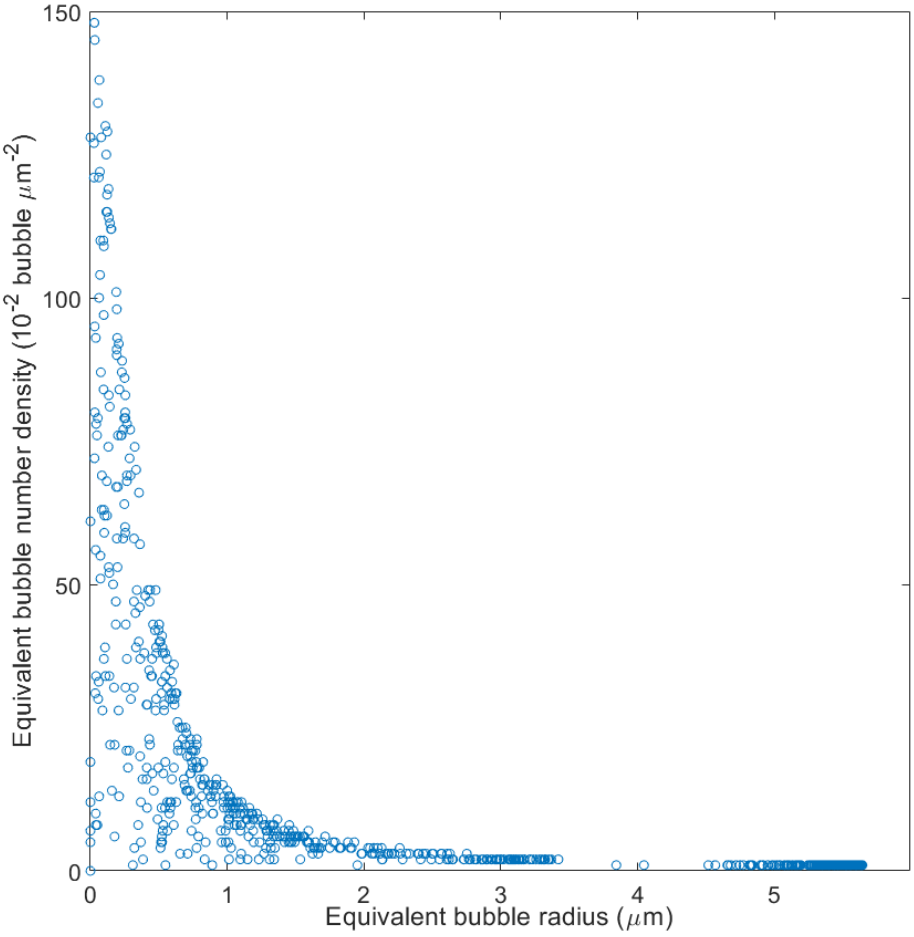

(a)

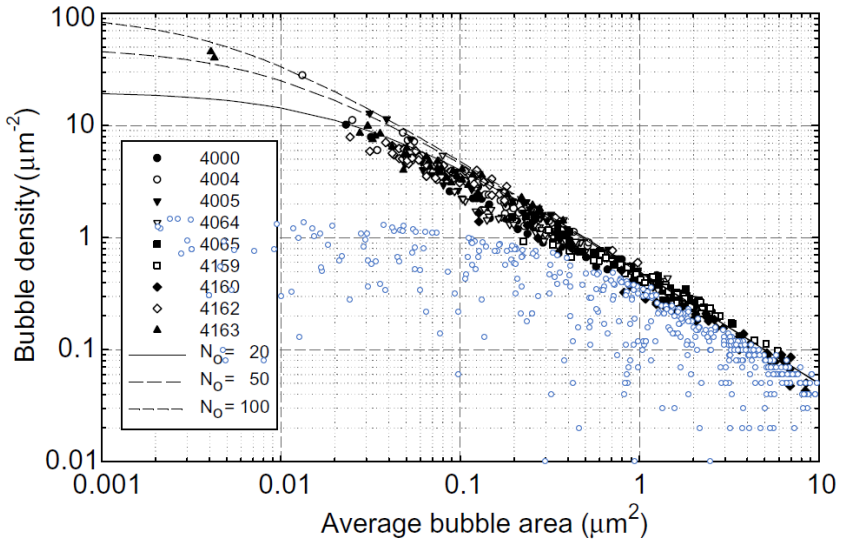

(b)

Figure 31: (a) Scatter plot of the space covered by the random numerical experiment; each point corresponds to a randomly generated grain face, and (b) compared with the experimental data by White [65] (the light blue dots are the same of Fig. 31a).

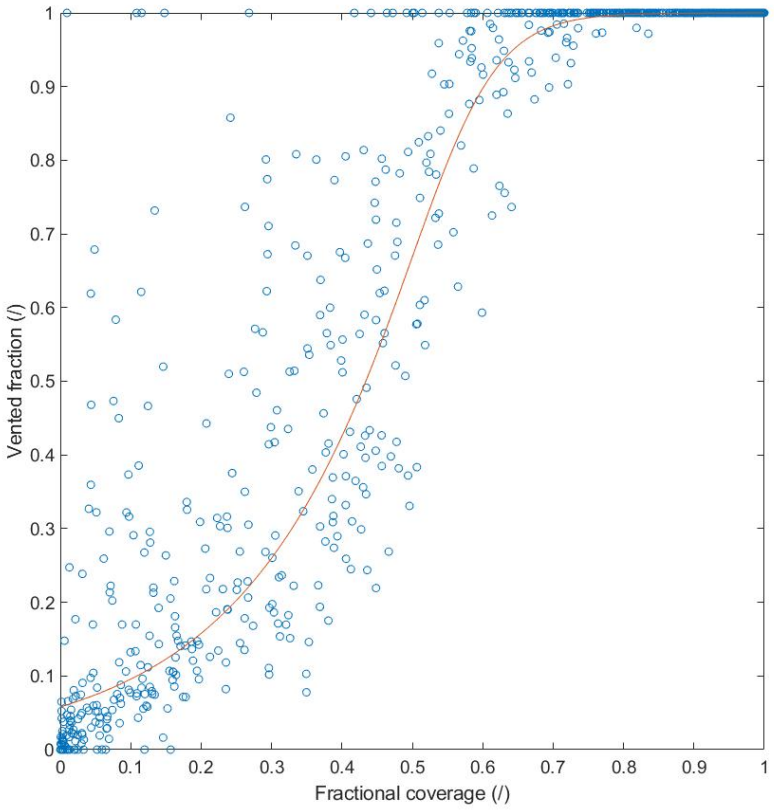

(a)

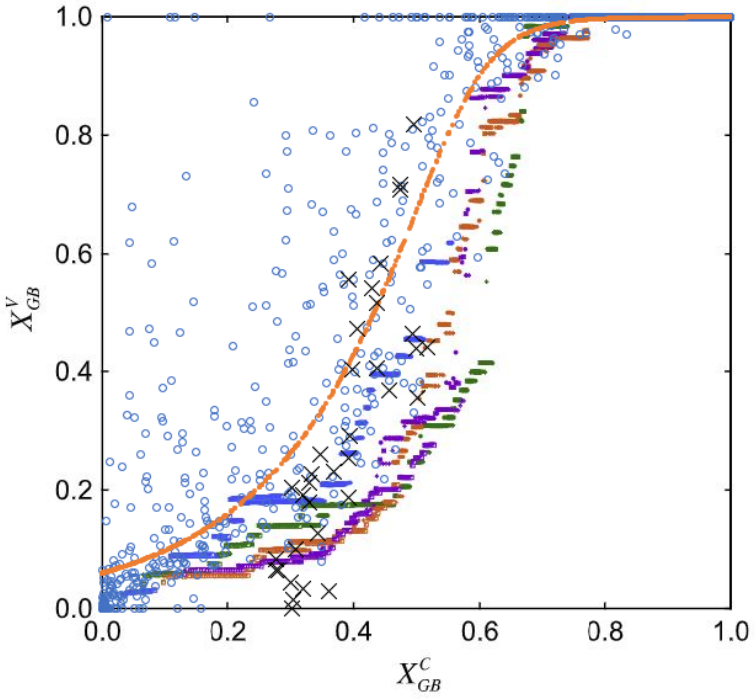

(b)

Figure 32: (a) Dependence of the vented fraction of randomly generated grain faces on the fractional coverage. The orange line corresponds to the best-estimate fit. (b) Comparison with the vented fraction (X_{GB}^{V}) proposed in this model (light blue dots and orange line) with the experimental results by White [65] (black crosses) and the phase field results by Millet *et al.* [64] (dark blue, brown, violet and green dots), as a function of the fractional coverage (X_{GB}^{C}).

More fundamental is the comparison between the herein proposed vented fraction derived from a geometrical numerical experiment and the experimental measurements performed by White [65] on irradiated fuel. The comparison in the space $\{A,N_{eq}\}$ is reported in Fig. 31b.

The agreement is satisfactory for bubble projected areas above 1 μm², whereas the results of the geometrical numeric experiment underestimates the experimental results for smaller bubble areas. This underestimation can be explained by analysing the assumption under which the geometrical numerical experiment is performed

- The use of single-sized random circles to geometrically construct the bubbles/clusters is a simplifying assumption that results in less bubbles/clusters compared to the real physical evolution represented by the experimental measurements. The nucleation of new bubbles is partially responsible of this discrepancy because it introduces a population of small bubbles not accounted for in the numerical experiment. However, the nucleation process is itself limited as the fractional coverage increases, since less and less free grain face is available for nucleation of new bubbles.
- The generation of random circles with centres uniformly distributed on the grain face (assumed as a square) is not strictly coincident with the distribution of the gas concentration gradient, driving the gas current from inside the grains towards a grain face. The gas concentration gradient driving the outflow of gas from the grain is maximum at the centre of the grain face and null on the grain edges. It is hence expected that a limited amount of bubbles should be close to the edges and to the corners of the square grain face. Considering this effect could increase the density of bubbles since the probability of finding isolated circles in the peripheral region of the grain face would increase, improving the agreement with the experimental data.

Further refinement of the proposed numerical experiment in view of these considerations is ongoing. A path forward to address the first point is sampling the size of each circle instead of adopting a single-sized approach. Adopting a non-uniform distribution for the position of the circles on the grain face, paired with the definition of vented fraction used by Millett and co-workers [64] (i.e., evaluating the contact of bubbles/clusters with a inscribed circle instead that on the edge of the grain face) could also improve the description.

Besides the limitations of representation in the $\{A,N_{eq}\}$-space mentioned, it is of interest to evaluate the agreement of the predicted vented fraction φ directly with the experimental data by White [65], depicted in Fig. 32b. For this figure of merit, which is fundamental for the herein proposed model, the agreement is satisfactory, with the proposed sigmoidal function (Eq. 27) appearing able to represent the experimental data. This conclusion is consistent with the previous discussion about Fig. 31b. White measured the vented fraction on the micrographs with (approximately) $A > 1$ μm², i.e., the section of Fig. 31b with good agreement between the experimental data and the geometrical numerical experiment.

3.2 Results

We present here the results of a test case simulated with SCIANTIX in which we compare the herein presented model considering the vented fraction and the state-of-the-art model already available in SCIANTIX. The test case is an 80'000 hours irradiation at 2000 K and 1.10^{19} fiss.m^{-3}.s^{-1}. Figure 33 reports the gas concentrations, i.e., the gas produced, the gas in grain, the gas at grain boundaries and the gas released. Figure 33a shows the results of the state-of-the-art model available in SCIANTIX. It can be observed how the gas released presents a clear onset corresponding to an abrupt change in the derivative of the gas at the grain boundaries. This behaviour is due to the treatment of fission gas release from the grain boundaries described as threshold phenomenon occurring when the fractional coverage exceeds the saturation coverage.

This modelling approach corresponds approximately to using a stepwise function instead of a sigmoid in describing the vented fraction (Fig. 32). Fig. 33b shows the result of the new model. Gas is released from the very beginning of the irradiation, presenting a smooth time-evolution with no abrupt changes. The immediate onset of release is a consequence of a combination of two modelling assumptions: (1) a fraction of grain-boundary bubbles is directly connected to the grain edges, i.e., vented, and (2) the grain edges are considered to be always percolated. A proper modelling of bubble growth and coalescence along the grain edges would improve this aspect of the present model.

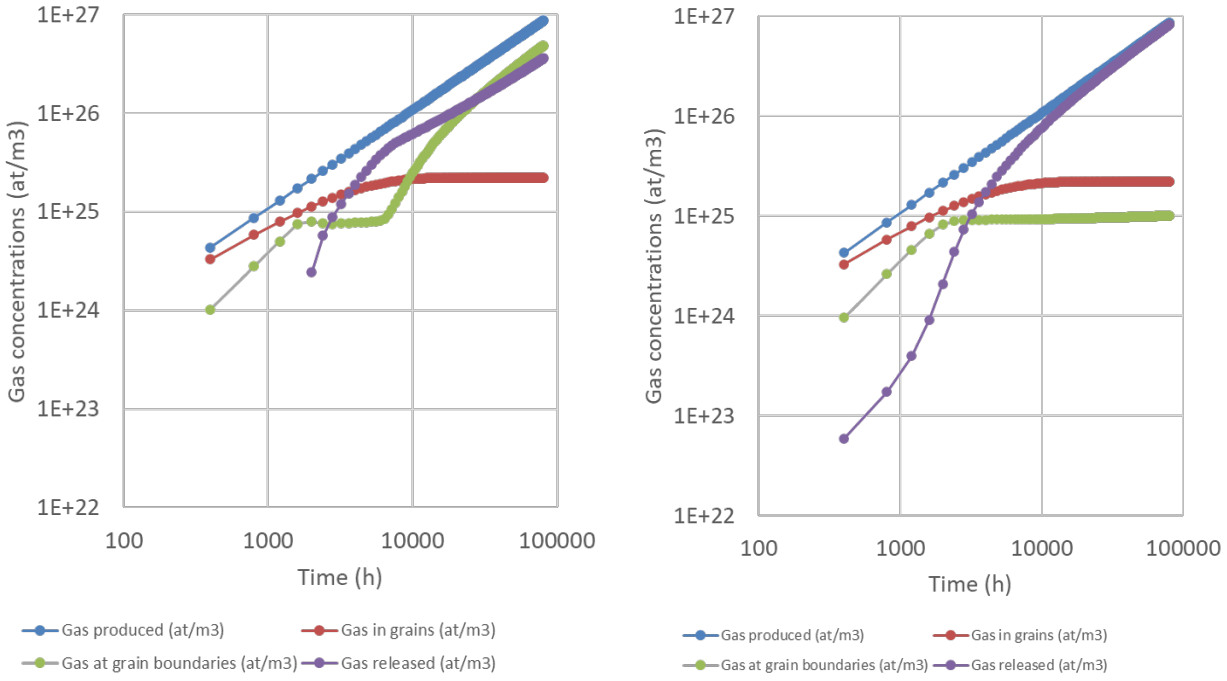

Figure 33: Evolution of gas concentrations in the (a) state-of-art SCIANTIX model and the (b) herein presented model.

Figure 34 shows the evolution of the grain boundary bubble density and grain boundary bubble radius. In the conditions of the test case analysed, the state-of-the-art model (Fig. 34a) shows unphysical behaviour: the bubble density drops below 10^8 bubbles m^{-2}, with $\approx 10^{10}$ bubble m^{-2} being the limit of roughly one bubble per grain face (the minimum experimental observation reported by White being $4\ 10^{10}$ m^{-2} [65]), and the bubble radius grows up to 10^{-4} m, one hundred times the typical grain size. By comparison, the results of the herein presented model (Fig. 34b) show similar trends but remain in a physical range. However, (1) the minimum bubble density predicted in these conditions is higher than the minimum observation by White [65], and (2) the predicted bubble radius is smaller than the bigger bubbles reported by White [65]. These issues will be analysed further when the geometrical numerical experiment is refined (see discussion in Section 4.1).

Finally, Fig. 35 shows the evolution of fractional coverage and grain-boundary swelling. As for the swelling, the conclusions are the same as those derived from the observation of the bubble density and the bubble radius (in view of the physical relationship between these variables): in the state-of-the-art model, the swelling reaches the clearly unphysical value of approximately 7 (i.e., 700 %) (Fig. 35a).

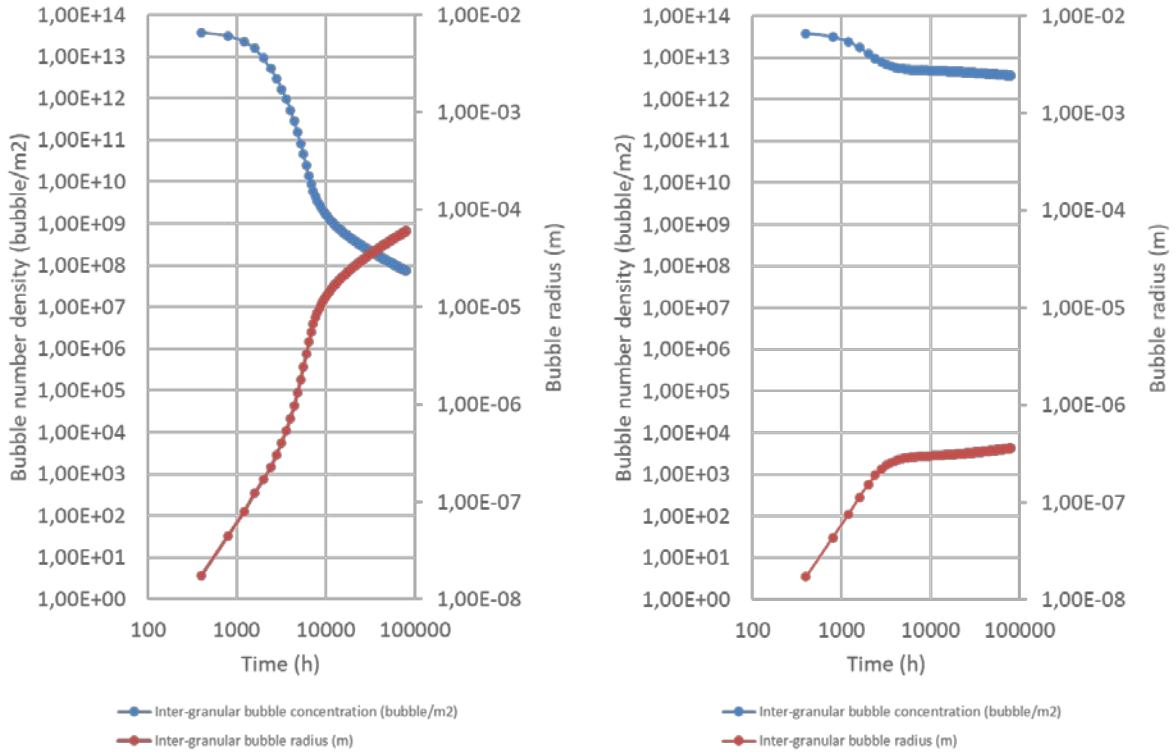

(a) (b)

Figure 34: Evolution of bubble number density and bubble radius for grain-boundary bubbles in the (a) state-of-art SCIANTIX model and the (b) herein presented model.

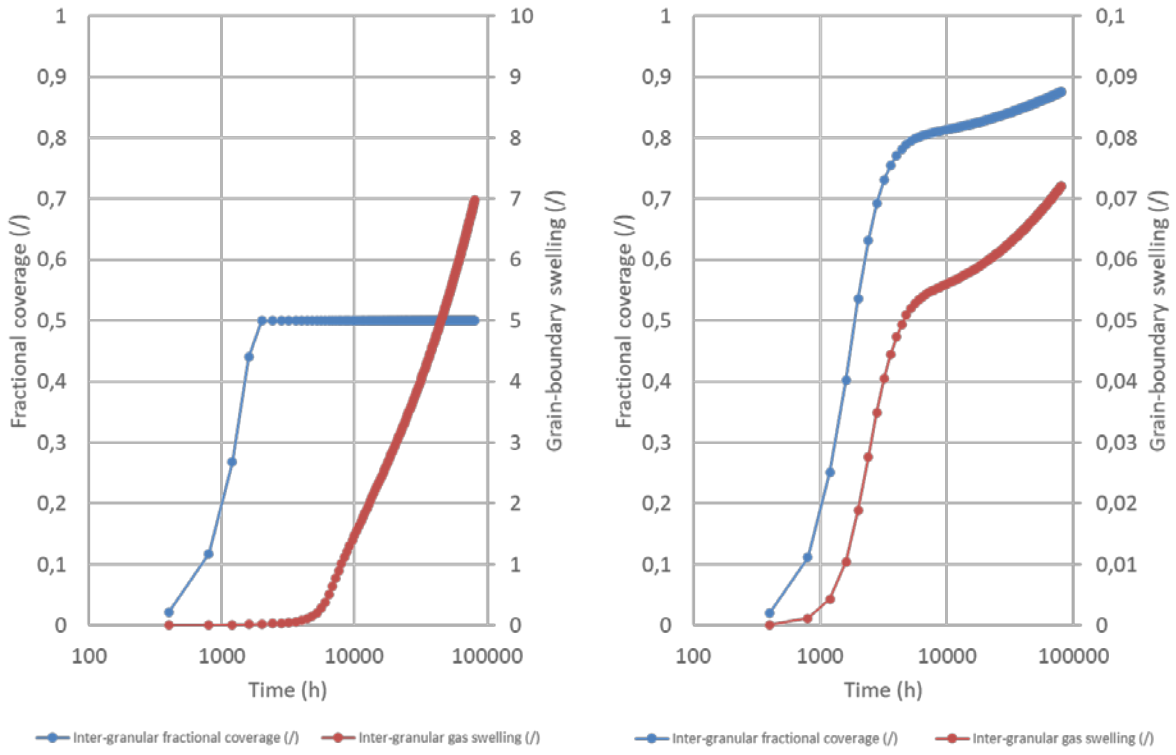

(a) (b)

Figure 35: Evolution of fractional coverage and grain-boundary swelling in the (a) state-of-art SCIANTIX model and the (b) herein presented model.

The evolution of the fractional coverage in Fig. 35a exhibits the threshold behaviour discussed above, whereas in Fig. 35b a continuous behaviour is revealed, corresponding to the continuous gas evolution yielded by the new model. Nevertheless, the fractional coverage increases up to values above 0.6 (which is the maximum observed experimentally in light water reactor conditions at high temperature [62]). This growth is due to the inflow of vacancies in the grain-boundary bubbles that remain over pressurized even when the gas inflow essentially stops after almost perfect percolation is achieved. A review of the mechanism of vacancy inflow and of its role at high temperature (i.e., with fast kinetics) is planned as a future development of the herein presented model.

4 HIGH BURN-UP STRUCTURE

Several models, either semi-empirical or mechanistic, were developed to describe high burn-up structure (HBS) effects in the framework of fuel performance codes. Lassmann *et al.* [66] developed a pragmatic, empirical model to account for intra-granular xenon depletion, decreasing its concentration with an exponential law as a function of burn-up (not considering the effect of temperature) and needing as an input parameter the HBS formation threshold. This approach represents the legacy treatment of HBS in TRANSURANUS [16]. The model by Khvostov and co-workers [67,68] describes the HBS restructuring through a Kolmogorov-Johnson-Mehl-Avrami (KJMA) relationship, introducing also the concept of *effective burn-up* in the description of HBS to weight differently the burn-up accumulation at high and low temperatures and thus consider thermal annealing of defects in the description of HBS formation. The concept of effective burn-up was integrated into the Lassmann model by Holt *et al.* [69], introducing also a more physical temperature threshold in the definition of effective burn-up with respect to the one originally proposed by Khvostov. This model is the standard treatment of the HBS formation/depletion in TRANSURANUS.

In this work, we propose a novel model describing HBS formation in oxide fuel, accounting for the progressive Xe depletion and its feedback on the fuel matrix swelling. We implemented the model in SCIANTIX [15]. The originality of the presented model lies in his intrinsic capability of representing HBS formation due to polygonization in a continuous and smooth manner, consistently accounting for the intra-granular fission gas behaviour during the formation process.

The content of this section is published in *T. Barani, D. Pizzocri, F. Cappia, L. Luzzi, G. Pastore, P. Van Uffelen, Submitted to Journal of Nuclear materials, Modeling High Burnup Structure in Oxide Fuels for Application to Fuel Performance Codes. Part I: High Burnup Structure formation.*

4.1 Model description

The formation of the HBS is described through a semi-empirical model that correlates the fraction of restructured fuel to the local effective burn-up. The behaviour of intra-granular fission gas in the restructured volume is described via a model available in the open literature [70]. We employed the data extracted from [69] and [70] to fit an expression for the HBS formation rate as a function of effective burn-up. We chose the functional form of the Kolmogorov-Johnson-Mehl-Avrami (KJMA) formalism, which is suitable to model generic restructuring phenomena and phase transitions and has been already proposed in HBS modelling [67,73].

The restructured volume fraction α (/) follows

$$\alpha = 1 - e^{-Kbu_{\text{eff}}{}^{m}} \quad (28)$$

Where, K = 2.77 10^{-7} is the transformation rate constant, m =3.35 is the so-called Avrami constant and bu_{eff} is the effective burn-up. It is interesting to note that a similar expression was adopted by Bouloré and co-workers [74] to evaluate the HBS restructuring rate in MIMAS uranium-plutonium mixed oxide fuel based on statistical considerations. The two constants K and m in Eq. 28 were determined by a least-square fitting of the experimental data shown in Fig. 36.

Although resulting from a fitting procedure, the coefficients we derived for Eq. 28 retain a physical meaning, which is a direct consequence of the KJMA theoretical formulation [75]. The value of the power to which the burn-up variable is taken (i.e., the Avrami constant, m) can provide information about the nature of the phase transition. A transformation featured by a constant bulk nucleation rate of the second phase – in the present work, HBS is representing the second phase – and by a bulk growth has a power equal to 4.

On the other hand, if the nucleation sites are preformed, or if transformation happens on grain boundaries in presence of a constant nucleation rate, the power is equal to 3. From the fitting procedure we obtain an Avrami constant between 3 and 4. This value reflects a mixed nature of the transformation, i.e., with contributions from bulk nucleation and growth and from bulk growth from preformed sites combined to a transformation occurring at grain boundaries. In the work by Khvostov and co-authors [67], the Avrami constant was taken equal to 3, i.e., only the latter mechanism was considered. The presence of this mechanism is corroborated by experimental observations and theoretical predictions [76–78]. This would not account for the formation of HBS following intra-granular patches, which has also been reported in several experimental works [78–81]. Indeed, the value obtained in this work accounts for all the mentioned contributions, being adherent to the different experimental findings.

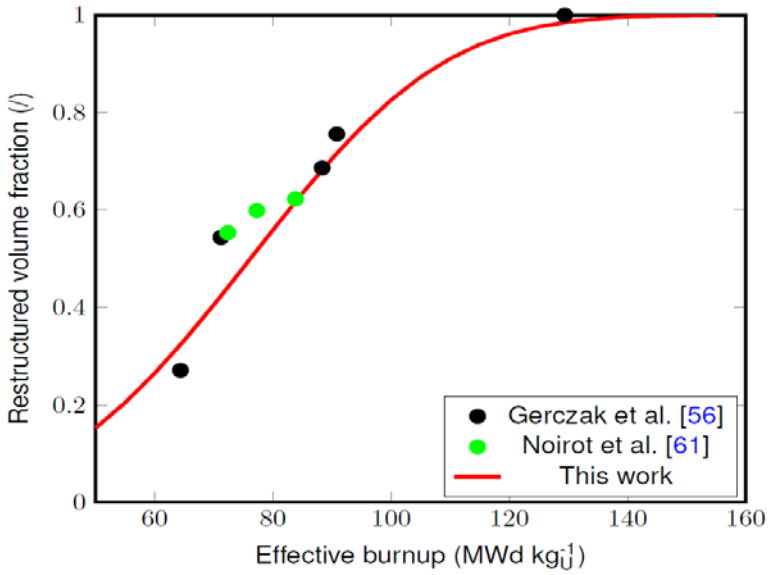

Figure 36: Restructured volume fraction as a function of the effective burn-up as described by KJMA.

The gas model is designed to be included in fuel performance codes and therefore we adopt the classical representation employed in such codes to describe fission gas diffusion, i.e., we represent the single grain as an equivalent spherical domain, employing the concept of an effective diffusion equation [52,82–84]. Eq. 28 is adopted to evaluate the volume fraction that underwent HBS restructuring.

Besides, the model considers a *two phase* material, one pertaining to the original microstructure and one to HBS, as sketched in Fig. 37.

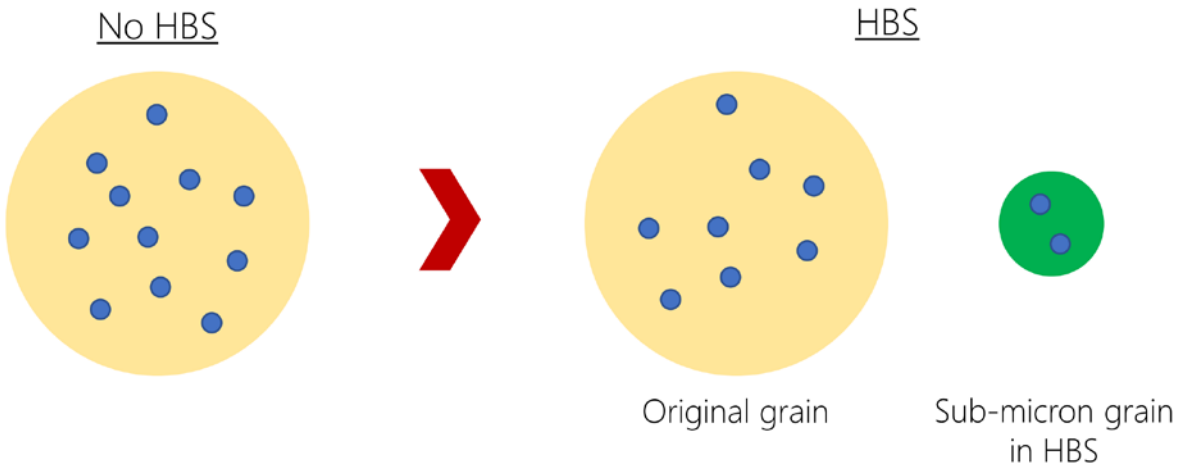

Figure 37: Representation of the modelling approach to intra-granular fission gas behaviour accounting for HBS progressive formation.

These two *phases* are featured by different grain sizes, i.e., the original microstructure (labelled as non-restructured, NR) usually by a micrometric size, whereas the HBS is assumed to be formed at a radius equal to 150 nm (in line with experimental data, e.g., by Ray and co-workers [85,86]). It is worth stressing that this modelling approach can be naturally extended to heterogeneous U-Pu mixed oxide fuels, featured by *regions* with different Pu content, resulting in local higher fission densities along the fuel pellet.

In both domains, the intra-granular gas behaviour is described through the mechanistic model presented in [14]. This model allows for the calculation of intra-granular fission gas bubble nucleation, growth due to gas atom trapping, destruction due to the interaction with fission fragments, along with considering a net diffusion of gas atoms towards the grain boundaries. As HBS is progressively forming, two intra-granular problems are solved, one for each *phase*. Henceforth, the overall concentration of gas in the considered domain c_t*, is evaluated as

$$c_t^* = (1-\alpha)c_t^{\mathrm{NR}} + \alpha c_t^{\mathrm{HBS}} \tag{29}$$

Where, the superscripts NR and HBS refer to the quantities evaluated solving the intra-granular problem in the non-restructured and HBS sub-domains, respectively. The same concept is applied to estimate each concentration. It is worth noting that a weighted average is also employed in the MARGARET code [87]. As HBS forms during irradiation, an increasing portion of the material is covered by the restructured microstructure. Thus, we consider a sweeping of gas concentration from the original to restructured region, namely

$$\frac{\mathrm{d}}{\mathrm{d}bu_{\mathrm{eff}}} c_t^{\mathrm{HBS}} = \frac{1}{\alpha}\left(c_t^{\mathrm{NR}} - c_t^{\mathrm{HBS}}\right)\frac{\mathrm{d}\alpha}{\mathrm{d}bu_{\mathrm{eff}}} - \frac{1-\alpha}{\alpha}\frac{\partial c_t^{\mathrm{NR}}}{\partial bu_{\mathrm{eff}}} \tag{30}$$

Where, the first term of the right-hand side of Eq. 30 represents the effective gas transfer between the two regions due to restructuring. Moreover, we assumed that the total concentration of gas in the considered reference volume is conserved during the restructuring.

The combination of increasing HBS volume ratio and smaller grain size of HBS allows for a consistent description of fission gas depletion as HBS is formed. As the effective burn-up builds up, an increasing fraction of the volume is affected by HBS (Eq. 28). This increases the weight of intra-granular behaviour

in the HBS sub-domain, which is characterized by a fast diffusion to the grain boundary associated with the nanometric grain size (the diffusion rate being $D_{eff} a^{-2}$).

Rather than attempting to describe HBS formation mechanistically, since the sequence of phenomena involved is still debated, the presented approach provides a robust model that accounts for HBS formation and gas depletion in a consistent manner, still preserving a degree of simplicity in line with fuel performance requirements.

4.2 Comparison with experimental results

The model presented in Section 5.1 was implemented in the SCIANTIX code [15]. The expressions of parameters employed in SCIANTIX are reported in Table 9.

Table 9: Expressions of the model parameters. F (fiss m^{-3} s^{-1}) is the fission rate, k (J K^{-1}) is the Boltzmann's constant, and T (K) is the temperature

Parameter		u.d.m.	Expression/value/reference
D^{NR}	Diffusivity, Non-recrystallized region	m^2 s^{-1}	$D_1+D_2+D_3$ $D_1 = 7.6\ 10^{-10} \exp(-4.86\ 10^{-19}/kT)$ $D_2 = 5.64\ 10^{-25}\ F^{0.5} \exp(-1.91\ 10^{-19}/kT)$ $D_3 = 2\ 10^{-40}\ F$ Turnbull *et al.* [93]
D^{HBS}	Diffusivity, HBS region	m^2 s^{-1}	$4.5\ 10^{-42}\ F$ Bremier and Walker [94] Pizzocri *et al.* [82]
β_n	Size-dependent trapping rate	s^{-1}	$4\pi D N R_n$ R_n = intra-granular bubble radius N = intra-granular bubble density Ham [30]
α_n	Size-dependent re-solution rate	s^{-1}	$2\pi\mu_{ff}F(R_n+R_{ff})^2$ $\mu_{ff} = 6\ 10^{-6}$ m, fission spike length R_n = intra-granular bubble radius $R_{ff} = 1\ 10^{-9}$ m, fission spike radius Turnbull *et al.* [95]
ν	Nucleation rate	m^{-3} s^{-1}	$2{\cdot}25\ F$ White and Tucker [96] Pizzocri *et al.* [14]

In Fig. 38, we compare the intra-granular concentration of xenon predicted by SCIANTIX simulations, considering the present model, to several experimental data obtained by different authors [79,88,89] via EPMA. Considering the huge scattering of the experimental data, due to different irradiation conditions and initial fuel specifications, the agreement is deemed satisfactory. For the sake of completeness, it must be underlined that xenon is accompanied by other gases in determining the overall gas behaviour (namely, krypton and helium). In this work, we draw a special attention on xenon since it was the subject of the most intensive experimental investigations.

For the sake of comparison, we also report the results obtained by several state-of-the-art models employed in fuel performance codes, in particular the model by Lassmann *et al.* [90], by Lemes *et al.*

[91], and by Pizzocri *et al.* [82]. The models by Lassmann and Lemes, the latter being an extension of the former, represent pragmatic and purely empirical approaches to account for fission gas depletion as HBS forms, considering an exponential decay of retained gas concentration with burn-up. They are directly fitted on a subset of the EPMA data reported, i.e., those by Walker [88]. Moreover, they consider a threshold for HBS formation solely dependent on burn-up, discarding the effect of temperature, which is instead considered in this work via the effective burn-up concept. In Fig. 38, predictions of those models considering different burn-up thresholds are reported, showing how this parameter impacts the maximum xenon retention and the subsequent depletion.

On the other hand, the model proposed by Pizzocri *et al.* [82,92] represents a step forward compared to the previous ones as it is not purely empirical. This model represents HBS formation by a gradual reduction of the grain size, which may be a questionable representation of the underlying physical processes. Differently from the present model results, the predictions obtained through this model and shown in Fig. 38 are obtained considering a xenon production rate adjusted to the experimental data at low burn-up to Walker data [88], to obtain a maximum xenon retention in line with experimental data. Finally, this model does not consider the evolution of intra-granular fission gas bubbles, employing a fixed value for intra-granular bubble density and radius, and disregards volume changes due to irradiation damage in the lattice. This results in an inconsistent estimation of gas partition between bubbles and dynamic solution, preventing a consistent calculation of matrix swelling due to single gas atoms and intra-granular bubbles, in addition to affect the effective diffusion representation.
The present model also accounts for the observed delay in xenon depletion (thus HBS formation) when considering higher grain sizes in the original microstructure, as shown in Fig. 38 and consistently with several experimental observations [76,80].

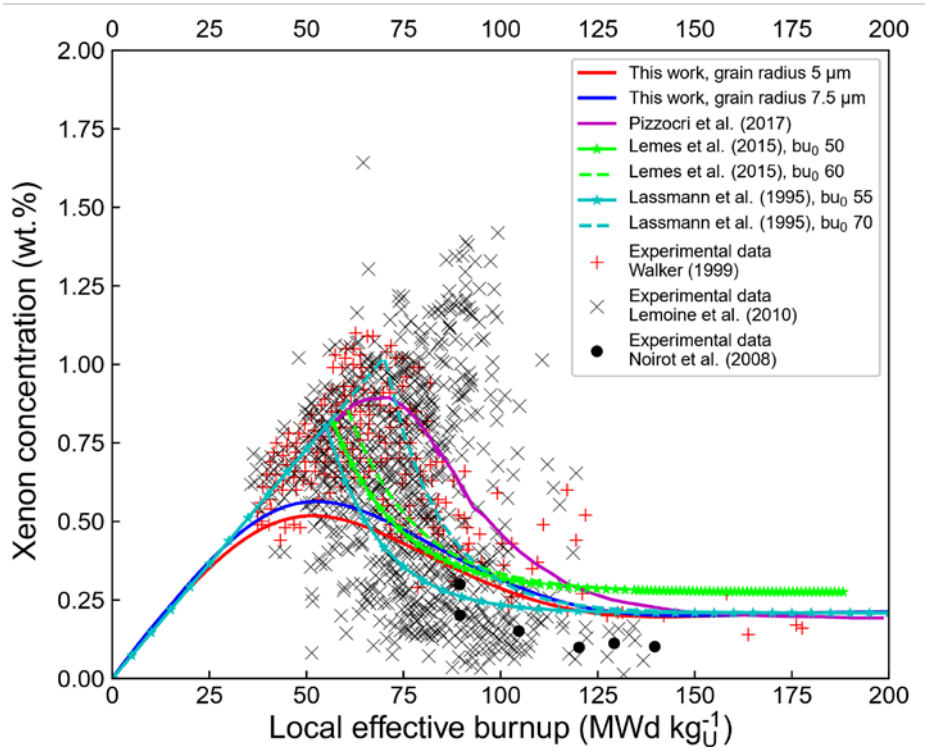

Figure 38: Comparison of various data on intra-granular xenon concentration obtained via EPMA (red crosses from Walker [88], black crosses from Lemoine *et al.* [89], and black dots from Noirot *et al.* [79]) to the predictions of the presented model. For the sake of comparison, the prediction obtained with other state-of-the-art models employed in fuel performance codes are included, namely from Pizzocri *et al.* [82], Lemes *et al.* [91], and Lassmann *et al.* [90].

5 CONCLUSION AND FUTURE DEVELOPMENTS

This deliverable synthesised the complete set of inert gas behaviour models developed in the INSPYRE project, targeting the simulation of MOX fuel in fast reactor conditions using fuel performance codes. All the models proposed are physics-based, mesoscale models allowing both for effective and efficient use in codes and for the incorporation of information from the lower-length scale in terms of model parameters. Further use of lower-length scale information derived in INSPYRE will be addressed in the last part of the project as this information becomes available.

The first model is a physics-based description of helium behaviour. We extended the classical description used for fission gas behaviour introducing a solubility term influencing the intra-granular behaviour of helium and effectively representing the mechanism of thermal resolution. The model results were compared with experimental data obtained in annealing conditions to isolate and test a subset of model parameters compared to the full set necessary to simulate an irradiation case. The agreement is overall promising and allowed to identify the most impactful parameters requiring further analysis, namely the above-mentioned thermal re-solution rate. We developed a depletion model tracking the evolution of actinides in fast reactor conditions to properly evaluate the helium production rate. This depletion model is based on high-fidelity simulations performed with SERPENT systematically used to determine spatial and energy averaged cross-sections as a function of burn-up and initial plutonium enrichment to be used in fuel performance codes. This depletion model was verified against the high-fidelity simulations of SERPENT for both sodium-cooled and lead-bismuth-eutectic-cooled fast reactors. The predictions are comparable and, in some cases, more accurate than current approaches used in fuel performance codes (TUBRNP, v1m1j18) that focus on relative radial profiles.

The second model concerns the treatment of gas diffusion in columnar grains. This problem is described by a non-linear partial differential equation, with the diffusion coefficient strongly varying along the grain axis, due to the temperature distribution within the fuel pellet. To be able to solve this challenging problem with a computational effort in line with the requirements of fuel performance codes, we propose a reduced order model based on proper orthogonal decomposition and Galerkin projection, which has been outlined in a previous deliverable (D6.1). We presented the results of the high-fidelity simulations of the problem performed with OpenFOAM and designed a roadmap of further analyses to be performed in SCIANTIX in order to identify the conditions in which the application of the reduced order model envisaged is necessary and the conditions in which simpler approximations (i.e., spectral methods applied in cylindrical geometry) may be acceptable.

The third model presented concerns the venting of grain faces, which is highly relevant because of the fast bubble growth and coalescence expected at the high temperatures characterizing operation of fast reactor MOX. The new description of grain-boundary venting proposed is derived based on a purely geometric random numerical experiment involving the generation of random grain faces with different fractional coverages and evaluating the vented fraction on each of them. The inclusion of a smooth percolation threshold instead of the stepwise function traditionally applied in fission gas behaviour models allows for a self-limiting evolution of the bubble growth and coalescence processes, making it possible to apply this physical description in fast reactor conditions. This modelling activity has been performed as part of a mobility action within INSPYRE and is being tested in fuel performance codes.

The fourth model extends the models of formation and depletion of the high burn-up structure currently used for UO_2 in fuel performance codes. The extension is based on newly obtained measurements of the fraction of volume occupied by HBS as function of the effective burn-up, i.e., the burn-up integrated below a certain temperature threshold, used as a measure of the lattice damage. This approach is more consistent with the physical process of HBS compared to other state-of-the-art models and succeeds in describing "naturally" the depletion of intra-granular fission gas from the HBS region. Moreover, the approach proposed by this model can be extended to describe the behaviour of inert gas in any heterogeneous material, including MOX fuel.

All the presented models have been implemented in SCIANTIX, which has been used for the both the verification and validation activities performed for each of these models. This approach is convenient since SCIANTIX is coupled to fuel performance codes in Task 7.1, acting as an inert gas behaviour module in the fuel performance codes.

We stress the fundamental role of new experimental data and lower-length scale calculation results yielded by the activities of WP 1 to 5 of INSPYRE to inform quantitatively (i.e., model parameters) and qualitatively (i.e., model hypothesis), as well as assess the new mesoscale models developed.

REFERENCES

[1] S.B. Fisher, R.J. White, P.M.A. Cook, S. Bremier, R.C. Corcoran, R. Stratton, C.T. Walker, P.K. Ivison, I.D. Palmer, Microstructure of irradiated SBR MOX fuel and its relationship to fission gas release, J. Nucl. Mater. 306 (2002) 153–172. doi:10.1016/S0022-3115(02)01247-3.

[2] Y.H. Koo, B.H. Lee, J.S. Cheon, D.S. Sohn, Modeling and parametric studies of the effect of inhomogeneity on fission gas release in LWR MOX fuel, Ann. Nucl. Energy. 29 (2002) 271–286. doi:10.1016/S0306-4549(01)00035-4.

[3] R. Parrish, A. Aitkaliyeva, A review of microstructural features in fast reactor mixed oxide fuels, J. Nucl. Mater. (2018). doi:10.1016/j.jnucmat.2018.05.076.

[4] S. Yatabe, M. Floyd, F. Dimayuga, Canadian experience in irradiation and testing of MOX fuel, J. Nucl. Mater. 502 (2018) 177–190. doi:10.1016/j.jnucmat.2018.02.015.

[5] D.R. Olander, Fundamental Aspects of Nuclear Reactor Fuel Elements, 1976. doi:10.1016/0022-3115(77)90226-4.

[6] V. Di Marcello, A. Schubert, J. Van De Laar, P. Van Uffelen, Extension of the TRANSURANUS plutonium redistribution model for fast reactor performance analysis, Nucl. Eng. Des. 248 (2012) 149–155. doi:10.1016/j.nucengdes.2012.03.037.

[7] V. Di Marcello, V. Rondinella, A. Schubert, J. Van De Laar, P. Van Uffelen, Modelling actinide redistribution in mixed oxide fuel for sodium fast reactors, Prog. Nucl. Energy. 72 (2014) 83–90. doi:10.1016/j.pnucene.2013.10.008.

[8] D. Pizzocri, L. Luzzi, T. Barani, L. Cognini, A. Magni, A. Schubert, P. Van Uffelen, T. Wiss, INSPYRE D6.1 - Review inert gas behaviour modelling, 2019.

[9] Gen-IV, Gen-IV, Https://Www.Gen-4.Org/Gif/Jcms/C_59461/Generation-Iv-Systems. (2018).

[10] ALFRED, ALFRED, Http://Www.Alfred-Reactor.Eu/. (2018).

[11] MYRRHA, MYRRHA, Https://Sckcen.Be/En/Technology_future/MYRRHA. (2018).

[12] L. Luzzi, A. Cammi, V. Di Marcello, S. Lorenzi, D. Pizzocri, P. Van Uffelen, Application of the TRANSURANUS code for the fuel pin design process of the ALFRED reactor, Nucl. Eng. Des. 277 (2014) 173–187. doi:10.1016/j.nucengdes.2014.06.032.

[13] G. Pastore, L. Luzzi, V. Di Marcello, P. Van Uffelen, Physics-based modelling of fission gas swelling and release in UO 2 applied to integral fuel rod analysis, Nucl. Eng. Des. 256 (2013) 75–86. doi:10.1016/j.nucengdes.2012.12.002.

[14] D. Pizzocri, G. Pastore, T. Barani, A. Magni, L. Luzzi, P. Van Uffelen, S.A. Pitts, A. Alfonsi, J.D. Hales, A model describing intra-granular fission gas behaviour in oxide fuel for advanced engineering tools, J. Nucl. Mater. 502 (2018). doi:10.1016/j.jnucmat.2018.02.024.

[15] D. Pizzocri, T. Barani, L. Luzzi, SCIANTIX: A new open source multi-scale code for fission gas behaviour modelling designed for nuclear fuel performance codes, J. Nucl. Mater. 532 (2020).

[16] K. Lassmann, TRANSURANUS: a fuel rod analysis code ready for use, J. Nucl. Mater. 188 (1992) 295–302. doi:10.1016/0022-3115(92)90487-6.

[17] E. Federici, A. Courcelle, P. Blanpain, H. Cognon, Helium production and behavior in nuclear oxide fuels during irradiation in LWR, in: Proc. 2007 Int. LWR Fuel Perform. Meet. San Fr. Calif., 2007: pp. 664–673.

[18] P. Botazzoli, Helium Production and Behaviour in LWR Oxide Nuclear Fuels, PhD Thesis, Politec. Di Milano, Italy. (2011).

[19] L. Cognini, A. Cechet, T. Barani, D. Pizzocri, P. Van Uffelen, L. Luzzi, Towards a physics-based description of intra-granular helium behaviour in oxide fuel for application in fuel performance codes, Nucl. Eng. Technol. (2020).

[20] M. V. Speight, A Calculation on the Migration of Fission Gas in Material Exhibiting Precipitation and Re-solution of Gas Atoms Under Irradiation, Nucl. Sci. Eng. 37 (1969) 180–185. doi:10.13182/nse69-a20676.

[21] D.R. Olander, D. Wongsawaeng, Re-solution of fission gas – A review: Part I. Intragranular bubbles, J. Nucl. Mater. 354 (2006) 94–109. doi:10.1016/j.jnucmat.2006.03.010.

[22] P. Lösönen, On the behaviour of intragranular fission gas in UO2 fuel, J. Nucl. Mater. 280 (2000) 56–72. doi:10.1016/S0022-3115(00)00028-3.

[23] M.S. Veshchunov, On the theory of fission gas bubble evolution in irradiated UO2 fuel, J. Nucl. Mater. 277 (2000) 67–81.

[24] P. Sung, Equilibrium solubility and diffusivity of helium in single-crystal uranium dioxide, PhD Thesis, Univ. Washingt. (1967).

[25] Z. Talip, T. Wiss, V. Di Marcello, A. Janssen, J.Y. Colle, P. Van Uffelen, P. Raison, R.J.M. Konings, Thermal diffusion of helium in 238Pu-doped UO2, J. Nucl. Mater. 445 (2014) 117–127. doi:10.1016/j.jnucmat.2013.10.066.

[26] P. van Uffelen, G. Pastore, V. di Marcello, L. Luzzi, Multiscale modelling for the fission gas behaviour in the TRANSURANUS Code, Nucl. Eng. Technol. 43 (2011) 477–488. doi:10.5516/NET.2011.43.6.477.

[27] A.M. Booth, A method of calculating fission gas diffusion from UO2 fuel and its application to the X-2-f loop test, 1957.

[28] L. Van Brutzel, A. Chartier, A new equation of state for helium nanobubbles embedded in UO2 matrix calculated via molucelar dynamics simulations, J. Nucl. Mater. 518 (2019) 431–439.

[29] L. Cognini, D. Pizzocri, T. Barani, P. Van Uffelen, A. Schubert, T. Wiss, L. Luzzi, Helium solubility in oxide nuclear fuel: Derivation of new correlations for Henry's constant, Nucl. Eng. Des. 340 (2018) 240–244. doi:10.1016/j.nucengdes.2018.09.024.

[30] F.S. Ham, Theory of diffusion-limited precipitation, J. Phys. Chem. Solids. 6 (1958) 335–351.

[31] L. Luzzi, L. Cognini, D. Pizzocri, T. Barani, G. Pastore, A. Schubert, T. Wiss, P. Van Uffelen, Helium diffusivity in oxide nuclear fuel: Critical data analysis and new correlations, Nucl. Eng. Des. 330 (2018). doi:10.1016/j.nucengdes.2018.01.044.

[32] K. Lassmann, C. O'Carroll, J. van de Laar, C.T. Walker, The radial distribution of plutonium in high burnup UO2 fuels, J. Nucl. Mater. 208 (1994) 223–231. doi:10.1016/0022-3115(94)90331-X.

[33] D. Pizzocri, L. Luzzi, T. Barani, L. Cognini, A. Magni, A. Schubert, P. Van Uffelen, T. Wiss, Review of available models and progress on the sub-models dealing with the intra- and intergranular inert gas behaviour, 2019. http://www.eera-jpnm.eu/inspyre/.

[34] D. Pizzocri, T. Barani, L. Luzzi, SCIANTIX Code, Online Repos. (n.d.). https://gitlab.com/poliminrg/sciantix (accessed October 4, 2019).

[35] D. Pizzocri, T. Barani, L. Luzzi, Coupling of TRANSURANUS with the SCIANTIX fission gas behaviour module, in: Int. Work. " Towar. Nucl. Fuel Model. Var. React. Types across Eur., 2019.

[36] J.-Y. Colle, E.A. Maugeri, C. Thiriet, Z. Talip, F. Capone, J.P. Hiernaut, R.J.M. Konings, A mass spectrometry method for quantitative and kinetic analysis of gas release from nuclear materials and its application to helium desorption from UO2 and fission gas release from irradiated fuel, J. Nucl. Sci. Technol. 51 (2014) 700–711.

[37] P. Van Uffelen, P. Botazzoli, L. Luzzi, S. Bremier, A. Schubert, P. Raison, R. Eloirdi, M.A. Barker, An experimental study of grain growth in mixed oxide samples with various microstructures and plutonium concentrations, J. Nucl. Mater. 434 (2013) 287–290. doi:10.1016/j.jnucmat.2012.11.053.

[38] K. Lassmann, A. Schubert, P. Van Uffelen, C. Gyori, J. Van De Laar, TRANSURANUS Handbook, Karlsruhe, Germany, 2014.

[39] G. Pastore, L.P. Swiler, J.D. Hales, S.R. Novascone, D.M. Perez, B.W. Spencer, L. Luzzi, P. Van Uffelen, R.L. Williamson, Uncertainty and sensitivity analysis of fission gas behavior in engineering-scale fuel modeling, J. Nucl. Mater. 456 (2015) 398–408. doi:10.1016/j.jnucmat.2014.09.077.

[40] S.M. Bowman, M.D. DeHart, C. V. Parks, Validation of SCALE-4 for Burnup Credit Applications, Nucl. Technol. 110 (1995) 53–70. doi:10.13182/nt95-a35096.

[41] P. Botazzoli, L. Luzzi, S. Brémier, A. Schubert, P. Van Uffelen, C.T. Walker, W. Haeck, W. Goll,

Extension and validation of the TRANSURANUS burn-up model for helium production in high burn-up LWR fuels, J. Nucl. Mater. 419 (2011) 329–338. doi:10.1016/j.jnucmat.2011.05.040.

[42] J.I. Tijero Cavia, A. Schubert, P. Van Uffelen, P. Pöml, S. Brémier, J. Somers, M. Seidl, R. Macián-Juan, The TRANSURANUS burn-up model for thorium fuels under LWR conditions, Nucl. Eng. Des. 326 (2018) 311–319. doi:10.1016/j.nucengdes.2017.11.021.

[43] K. Tanaka, S. Miwa, I. Sato, T. Hirosawa, H. Obayashi, S. ichi Koyama, H. Yoshimochi, K. Tanaka, Microstructure and elemental distribution of americium-containing uranium plutonium mixed oxide fuel under a short-term irradiation test in a fast reactor, J. Nucl. Mater. 385 (2009) 407–412. doi:10.1016/j.jnucmat.2008.12.028.

[44] E. Fridman, J. Leppänen, On the use of the Serpent Monte Carlo code for few-group cross section generation, Ann. Nucl. Energy. 38 (2011) 1399–1405. doi:10.1016/j.anucene.2011.01.032.

[45] K. Tasaka, J. Katakura, H. Ihara, T. Nakagawa, H. Takano, T. Yoshida, S. Iijima, R. Nakasima, JNDC nuclear data library of fission products, second version, (1990).

[46] E. Commission, Transuranus handbook, 2017 (2017).

[47] K. Lassmann, TRANSURANUS: a fuel rod analysis code ready for use, J. Nucl. Mater. 188 (1992) 295–302. doi:10.1016/0022-3115(92)90487-6.

[48] A. Schubert, P. Van Uffelen, J. van de Laar, C.T. Walker, W. Haeck, Extension of the TRANSURANUS burn-up model, J. Nucl. Mater. 376 (2008) 1–10. doi:10.1016/J.JNUCMAT.2008.01.006.

[49] H. Aït Abderrahim, P. Baeten, D. De Bruyn, R. Fernandez, MYRRHA - A multi-purpose fast spectrum research reactor, in: Energy Convers. Manag., 2012. doi:10.1016/j.enconman.2012.02.025.

[50] M. Pusa, Numerical methods for nuclear fuel burnup calculations, 2013.

[51] V. Sobolev, Database of thermophysical properties of liquid metal coolants for GEN-IV, 2010.

[52] A.H. Booth, A method of calculating fission gas diffusion from UO\textsubscript{2} fuel and its application to the X-2-f loop test, At. Energy Canada Ltd. Chalk River Proj. Res. Dev. Rep. AECL-496. (1957) 1–23.

[53] J.S. Hesthaven, G. Rozza, B. Stamm, Certified Reduced Basis Methods for Parametrized Partial Differential Equations, 2015.

[54] OpenFOAM, OpenFOAM, Https://Www.Openfoam.Com/. (2018).

[55] J.A. Turnbull, C.A. Friskney, J.R. Findlay, F.A. Johnson, A.J. Walter, The diffusion coefficients of gaseous and volatile species during the irradiation of uranium dioxide, J. Nucl. Mater. 107 (1982) 168–184.

[56] R.J. White, A New Mechanistic Model for the Calculation of Fission Gas Release, in: Proc. Int. Top. Meet. Light WATER React. FUEL Perform., ANS, Palm Beach, Florida, 1994: pp. 196–202.

[57] A.A. Prudil, E.S. Thomas, M.J. Welland, Network percolation using a two-species included phase model to predict fission gas accomodation and venting, J. Nucl. Mater. 515 (2019) 170–186.

[58] P. Van Uffelen, Contribution to the modelling of fission gas release in Light Water Reactor fuel, Université de Liège, 2002.

[59] G. Pastore, L. Luzzi, V. Di Marcello, P. Van Uffelen, Physics-based modelling of fission gas swelling and release in UO 2 applied to integral fuel rod analysis, Nucl. Eng. Des. 256 (2013) 75–86. doi:10.1016/j.nucengdes.2012.12.002.

[60] M. V Speight, W. Beere, Vacancy potential and void growth on grain boundaries, Met. Sci. 9 (1975) 190–191.

[61] A. Claisse, P. Van Uffelen, Towards the inclusion of open fabrication porosity in a fission gas release model, J. Nucl. Mater. 466 (2015) 351–356.

[62] R.J. White, R.C. Corcoran, P.J. Barnes, A Summary of Swelling Data Obtained from the AGR / Halden Ramp Test Programme, 2006.

[63] T. Kogai, Modelling of fission gas release and gaseous swelling of light water reactor fuels, J. Nucl. Mater. 244 (1997) 131–140. doi:10.1016/S0022-3115(96)00731-3.

[64] P.C. Millett, M.R. Tonks, S.B. Biner, L. Zhang, K. Chockalingam, Y. Zhang, Phase-field simulation of

intergranular bubble growth and percolation in bicrystals, J. Nucl. Mater. 425 (2012) 130–135.

[65] R.J. White, The development of grain-face porosity in irradiated oxide fuel, J. Nucl. Mater. 325 (2004) 61–77. doi:10.1016/j.jnucmat.2003.10.008.

[66] K. Lassmann, C.T. Walker, J. van de Laar, F. Lindström, Modelling the high burnup UO2 structure in LWR fuel, J. Nucl. Mater. 226 (1995) 1–8. doi:10.1016/0022-3115(95)00116-6.

[67] G. Khvostov, V. Novikov, A. Medvedev, S. Bogatyr, Approaches to Modeling of High Burn-up Structure and Analysis of its Effects on the Behaviour of Light Water Reactor Fuels in the START-3 Fuel Performance Code, in: Water React. Fuel Perform. Meet. 2005, 2005.

[68] G. Khvostov, K. Mikityuk, M.A. Zimmermann, A model for fission gas release and gaseous swelling of the uranium dioxide fuel coupled with the FALCON code, Nucl. Eng. Des. 241 (2011) 2983–3007. doi:10.1016/j.nucengdes.2011.06.020.

[69] L. Holt, A. Schubert, P. Van Uffelen, C.T. Walker, E. Fridman, T. Sonoda, Sensitivity study on Xe depletion in the high burn-up structure of UO 2, J. Nucl. Mater. 452 (2014) 166–172. doi:10.1016/j.jnucmat.2014.05.009.

[70] D. Pizzocri, G. Pastore, T. Barani, A. Magni, L. Luzzi, P. Van Uffelen, S. Pitts, A. Alfonsi, J.D. Hales, A model describing intra-granular fission gas behaviour in oxide fuel, J. Nucl. Mater. 502 (2018).

[71] J. Noirot, Y. Pontillon, S. Yagnik, J.A. Turnbull, Post-irradiation examinations and high-temperature tests on undoped large-grain UO2 discs, J. Nucl. Mater. 462 (2015) 77–84. doi:10.1016/j.jnucmat.2015.03.008.

[72] T.J. Gerczak, C.M. Parish, P.D. Edmondson, C.A. Baldwin, K.A. Terrani, Restructuring in high burnup UO2 studied using modern electron microscopy, J. Nucl. Mater. 509 (2018) 245–259. doi:10.1016/j.jnucmat.2018.05.077.

[73] M. Kinoshita, Mesoscopic approach to describe the high burn-up fuel behaviour, in: Enlarg. Halden Proj. Gr. Meet., Loen, Norway, 1999.

[74] A. Bouloré, L. Aufore, E. Federici, P. Blanpain, R. Blachier, Advanced characterization of MIMAS MOX fuel microstructure to quantify the HBS formation, Nucl. Eng. Des. 281 (2015) 79–87.

[75] J.W. Cahn, Transformation kinetics during continuous cooling, Acta Metall. 4 (1956) 572–575.

[76] K. Nogita, K.M. Une Hirai, K. Ito, Effect of grain size on recrystallization in high burnup fuel pellets, J. Nucl. Mater. 248 (1997) 196–203.

[77] J. Spino, A.D. Stalios, H. Santa Cruz, D. Baron, Stereological evolution of the rim structure in PWR-fuels at prolonged irradiation: Dependencies with burn-up and temperature, J. Nucl. Mater. 354 (2006) 66–84. doi:10.1016/j.jnucmat.2006.02.095.

[78] D. Baron, M. Kinoshita, P. Thevenin, R. Largenton, Discussion about HBS transformation in high burn-up fuels, Nucl. Eng. Technol. 41 (2009) 199–214.

[79] J. Noirot, L. Desgranges, J. Lamontagne, Detailed characterisations of high burn-up structures in oxide fuels, J. Nucl. Mater. 372 (2008) 318–339.

[80] J. Noirot, Y. Pontillon, S. Yagnik, J.A. Turnbull, Post-irradiation examinations and high-temperature tests on undoped large-grain UO\textsubscript{2} discs, J. Nucl. Mater. 462 (2015) 77–84.

[81] M. Chollet, G. Kuri, D. Grolimund, M. Marrtin, L. Bertsch, Synchrotron XRD Analysis of Irradiated UO2 Fuel at Various Burn-up, in: TopFuel 2016 LWR Fuels with Enhanc. Saf. Perform., Boise, Idaho, USA, 2016.

[82] D. Pizzocri, F. Cappia, L. Luzzi, G. Pastore, V. V Rondinella, P. Van Uffelen, A semi-empirical model for the formation and depletion of the high burnup structure in UO\textsubscript{2}, J. Nucl. Mater. 487 (2017) 23–29.

[83] J. Rest, M.W.D. Cooper, J. Spino, J.A. Turnbull, P. Van Uffelen, C.T. Walker, Fission gas release from UO\textsubscript{2} nuclear fuel: A review, J. Nucl. Mater. 513 (2019) 310–345.

[84] P. Van Uffelen, J. Hales, W. Li, G. Rossiter, R. Williamson, A review of fuel performance modelling, J. Nucl. Mater. 516 (2019) 373–412. doi:10.1016/j.jnucmat.2018.12.037.

[85] I.L.F. Ray, H.J. Matzke, H.A. Thiele, M. Kinoshita, An electron microscopy study of the RIM

structure of a UO\textsubscript{2} fuel with a high burnup of 7.9% FIMA, J. Nucl. Mater. 245 (1997) 115–123.

[86] V. V. Rondinella, T. Wiss, The high burn-up structure in nuclear fuel, Mater. Today. 13 (2010) 24–32. doi:10.1016/S1369-7021(10)70221-2.

[87] L. Noirot, MARGARET: A comprehensive code for the description of fission gas behavior, Nucl. Eng. Des. 241 (2011) 2099–2118.

[88] C.T. Walker, Assessment of the radial extent and completion of recrystallisation in high burn-up UO\textsubscript{2} nuclear fuel by EPMA, J. Nucl. Mater. 275 (1999) 56–62.

[89] F. Lemoine, D. Baron, P. Blanpain, Key parameters for the High Burnup Structure fromation thresholds, in: 2010 LWR Fuel Perform. Meet. Fuel/WRFPM, Orlando, Florida, USA, 2010.

[90] K. Lassmann, C.T. Walker, J. van de Laar, F. Lindström, Modelling the high burnup UO\textsubscript{2} structure in LWR fuel, J. Nucl. Mater. 226 (1995) 1–8.

[91] M. Lemes, A. Soba, A. Denis, An empirical formulation to describe the evolution of the high burnup structure, J. Nucl. Mater. 456 (2015) 174–181.

[92] T. Wiss, V. V. Rondinella, R.J.M. Konings, D. Staicu, D. Papaioannou, S. Bremier, P. Pöml, O. Benes, J.-Y. Colle, P. Van Uffelen, A. Schubert, F. Cappia, M. Marchetti, D. Pizzocri, F. Jatuff, W. Goll, T. Sonoda, A. Sasahara, S. Kitajima, M. Kinoshita, Properties of the high burnup structure in nuclear light water reactor fuel, Radiochim. Acta. 105 (2017) 893–906. doi:10.1515/ract-2017-2831.

[93] J. Turnbull, R. White, C. Wise, The diffusion coefficient for fission gas atoms in uranium dioxide, in: Proc. a Tech. Comm. Meet. Organ. by Int. At. Energy Agency Held Preston, 18-22 Sept. 1988, 1989.

[94] S. Brémier, C.T. Walker, Radiation-enhanced diffusion and fission gas release from recrystallised grains in high burn-up UO2 nuclear fuel, Radiat. Eff. Defects Solids. 157 (2002) 311–322. doi:10.1080/10420150213000.

[95] J.A. Turnbull, The distribution of intragranular fission gas bubbles in UO\textsubscript{2} during irradiation, J. Nucl. Mater. 38 (1971) 203–212.

[96] R.J. White, M.O. Tucker, A new fission gas release model, J. Nucl. Mater. 118 (1983) 1–38.

[97] C. Ronchi, J.P. Hiernaut, Helium diffusion in uranium and plutonium oxides, J. Nucl. Mater. 325 (2004) 1–12.

[98] P. Talou, T. Kawano, P.G. Young, M.B. Chadwick, R.E. MacFarlane, Improved evaluations of neutron-induced reactions on americium isotopes, Nucl. Sci. Eng. 155 (2007) 84–95. doi:10.13182/NSE07-A2646.